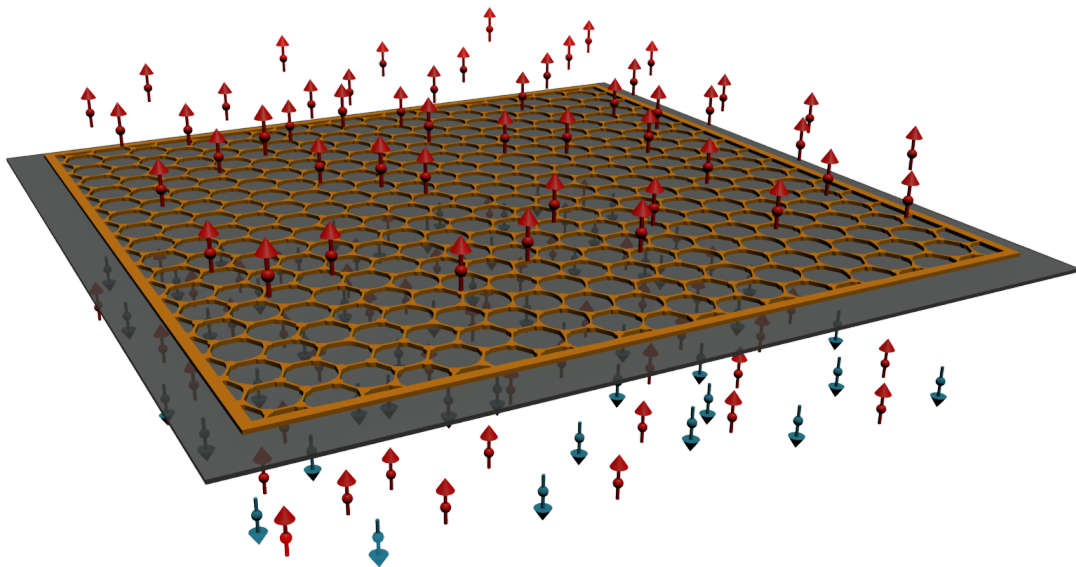


Towards experimental realisation of spin filtering at the graphene-nickel(111) interface



Master Thesis

A thesis submitted in partial fulfilment of the requirements to obtain the degree of
Master of Science in Applied Physics at the University of Twente.

October 22, 2014

Author

Jelmer M. Boter, BSc.

Graduation committee

prof.dr.ir W.G. van der Wiel
prof.dr. P.J. Kelly
dr.ir M.P. de Jong
ir. E. van Geijn

UNIVERSITY OF TWENTE.

NANO ELECTRONICS.

Abstract

This thesis presents the results of a master assignment aimed to verify the theoretical prediction of perfect spin filtering at the interface between graphene and the (111) surface of nickel by means of Tedrow-Meservey measurements. Karpan *et al.* predicted perfect spin filtering as a result of the almost perfect lattice match of graphene and the close-packed surface of nickel's fcc crystal, and the electronic properties of these materials. To verify this prediction devices are fabricated that are based on a vertical tunnel junction, comprising the graphene-nickel(111) interface, a tunnel barrier (aluminium oxide) and a superconductor (aluminium). A magnetic field is applied to spin-split the characteristic density of states for this superconductor as a result of the Zeeman effect, such that it can be used to measure the spin polarisation of electrons tunnelling from the graphene-nickel interface. This measurement technique was invented by Tedrow and Meservey. Both the spin filtering effect itself and the used measurement technique impose strict requirements on the used substrate, i.e. graphene grown on nickel by means of chemical vapour deposition, the device design and the fabrication.

The main results comprise the structural and magnetic properties of the used nickel substrate as well as the characteristics of the graphene layer. A purchased substrate of CVD grown graphene on nickel is shown to fulfil the minimal requirements for the intended purpose. Following earlier research Raman spectroscopy is shown to be a useful technique to characterise graphene. In combination with cluster analysis it is a powerful tool to determine, amongst other properties, the thickness of graphene layers. Furthermore, a clear correspondence between optical images, scanning electron microscopy images and Raman measurements is shown, which allows for the use of an optical microscope to estimate the graphene thickness. A marker pattern makes it possible to directly relate images made by an optical microscope to Raman measurements. Cluster analysis again proves to be an extremely powerful method to correlate the measurements based on the markers and subsequently analyse the results. Based on these findings, a method for lithographic alignment of the junction area based on optical images and AFM images is proposed, which employs the shown alignment of atomic force microscopy images on optical images. Placement of contact holes with this method takes into account the properties of both nickel and graphene.

A non-destructive process to fabricate the junctions has been developed and tunnelling is verified to be the main transport mechanism. However, device fabrication revealed challenges, in particular related to the roughness of the nickel substrate, which results from the high temperature in the CVD process of graphene growth. As a result the thin layers of the top electrode probably are not continuous. Further optimisation of the fabrication process is needed. Nevertheless, junctions that show interesting and reproducible results in low-temperature (magneto)transport studies are successfully fabricated. Defect assisted tunnelling and, although rare, features consistent with superconductivity are demonstrated in addition to presently unexplained features, which require further research.

Image front cover: Artist impression of spin filtering at the graphene-nickel(111) interface. Image made by **Gerald Bussink**.

Contents

	Page
1 Introduction	1
2 Theory	3
2.1 Reciprocal space, energy and density of states	3
2.2 Graphite and graphene	4
2.3 Spin	5
2.3.1 Spin-orbit coupling and hyperfine interaction	6
2.3.2 Spintronics	6
2.3.3 Ferromagnetism and nickel	8
2.3.4 Magnetoresistance	9
2.4 Spin filtering at interfaces between nickel close-packed surfaces and graphene . .	10
2.5 Spin polarisation measurements: Tedrow-Meservey	11
3 Experimental methods	15
3.1 Fabrication	15
3.1.1 Photolithography	15
3.1.2 Electron beam lithography	17
3.1.3 Ion beam etching	17
3.1.4 Electron beam evaporation	18
3.2 Characterisation	18
3.2.1 Atomic force microscopy	18
3.2.2 Raman spectroscopy	19
3.2.3 Scanning electron microscopy	22
3.2.4 Vibrating sample magnetometry	24
3.2.5 X-ray diffraction	24
3.2.6 X-ray photoelectron spectroscopy	25
3.3 Transport measurements	25
3.3.1 Current-voltage (IV) measurements	27
3.3.2 Magnetoresistance	28
3.4 Data analysis	28
3.4.1 Cluster analysis	28
4 Design and fabrication	31
4.1 Design	31
4.2 Fabrication	32
4.2.1 Contact holes	33
4.2.2 Top electrodes	34

5	Results and discussion	35
5.1	Sample characterisation	35
5.1.1	Nickel	35
5.1.2	Graphene	38
5.2	Device fabrication	45
5.2.1	Lithographic alignment of junctions	45
5.2.2	Bottom electrodes, resist layer and contact holes	47
5.2.3	Top electrode	50
5.3	Transport measurements	50
5.3.1	Photolithographically defined contact holes	51
5.3.2	Contact holes defined by means of EBL	53
6	Conclusions and recommendations	63
	Review and acknowledgements	67
	Bibliography	69
A	Theory	73
A.1	Tedrow-Meservey measurements	73
A.2	Lever arm effect	75
B	Design and fabrication	77
B.1	Recipe	77
B.2	Workflow	81
B.3	Mask	84
C	Results	85
C.1	Graphene thickness	85

List of physical constants

Quantity	Symbol	Value
Bohr magneton	μ_B	$9.274 \cdot 10^{-24} J/T$
Electron rest mass	m_e	$9.109 \cdot 10^{-31} kg$
Elementary charge	e	$1.602 \cdot 10^{-19} C$
Planck constant	h	$6.626 \cdot 10^{-34} J \cdot s$
Reduced Planck constant	\hbar	$\frac{h}{2\pi} = 1.055 \cdot 10^{-34} J \cdot s$
Speed of light in vacuum	c	$2.998 \cdot 10^8 m/s$
Vacuum permeability	μ_0	$4\pi \cdot 10^{-7} N/A^2 = 1.257 \cdot 10^{-6} N/A^2$

List of abbreviations

AFM	Atomic force microscope
ALD	Atomic layer deposition
CARS	Coherent anti-Stokes Raman spectroscopy
CVD	Chemical vapour deposition
DOS	Density of states
E_F	Fermi energy
EBL	Electron beam lithography
eV	Electronvolt ($= 1.602 \cdot 10^{-19} J$)
FCC	Face-centered cubic
FIB	Focused ion beam
FM	Ferromagnet(ic material)
FWHM	Full width at half maximum
GMR	Giant magnetoresistance
IPA	Isopropanol
LMTO	Linear muffin-tin orbital
MIBK	Methyl isobutyl ketone
MTJ	Magnetic tunnel junction
PMMA	Poly(methyl methacrylate)
(R)IBE	(Reactive) ion beam etching
SEM	Scanning electron microscope
SERS	Surface enhanced Raman scattering
STM	Scanning tunneling microscope
TMAH	Tetramethylammonium hydroxide
TMR	Tunneling magnetoresistance
(U)HV	(Ultra-)high vacuum
v_F	Fermi velocity
VSM	Vibrating sample magnometry
XPS	X-ray photoelectron spectroscopy
XRD	X-ray diffraction

Chapter 1

Introduction

Conventional electronics has fulfilled its tasks for quite some years and I expect this also to be the case in the (near) future. However, the demand for continuously increasing performance and additional functionalities requires more. To meet these expectations a wide range of physical phenomena is subject of scientific research and has the interest of industry. This already resulted in some very promising developments and probably more will emerge in the coming years. Among these research areas is organic spintronics that combines spintronics with organic materials.

The field of spintronics is one of the rapidly developing branches in condensed-matter physics. Spintronics exploits the intrinsic spin of electrons, which is strongly related to magnetism. It is based on the degree of freedom offered by the spin of electrons and the corresponding magnetic moment instead of or in addition to their charge. In spintronics the central theme is the active manipulation of spin degrees of freedom. The goal is to understand the interactions of the particle spin with its solid-state environment and to make useful devices based on this knowledge.¹ How spin polarisation of electrons can be manipulated, what the mechanisms of spin relaxation and dephasing are, what the involved time scales are and how spin detection can be realized all are key questions in this research area. An example of a well-known application of spintronics is the read head of a hard disk in which magnetic elements are used for data storage. Here the giant magnetoresistance (GMR) effect is used to read our data. The current main focus is on downscaling of the involved structures to increase data density. An alternative approach is offered by new device architectures, for example a spin transistor, which allows for the combination of logic operations, storage and communication. In addition, the relevant energy scale for spin-based devices is smaller than for charge-based devices, so spintronic devices are potentially fast and less energy consumptive. Most devices in the field of spintronics still use the combination of spin and charge. Spin is only used as internal variable, while final variables are charge-based, which requires multiple back and forth conversion from spin to charge. Behin-Aein et al.² proposed a all-spin logic device with memory functionality in which spin is used in every step.

Organic matter is what constitutes living creatures. No single definition of organic materials exists, but usually they are characterised by the fact that they contain carbon and hydrogen. A very wide range of materials is contained in this class. Organic materials usually are light weight, mechanically flexible, easy to process and in many cases bio-degradable and have the possibility of extra functionality, such as chemical tuning of electrical properties. Conventional electronics relies on semiconductors for a very wide range of its applications. Therefore, organic semiconductors are considered as potentially very useful materials. Several materials consisting of only carbon atoms exist. These materials are not considered organic themselves, although they are common in organic electronics. Some have already been known for a long time and the best examples are graphite, which can be found in a pencil, and diamond, which is used in jewellery and also in industry because of its hardness. Another carbon allotrope is graphene,

which is a single sheet of carbon atoms that are arranged in a honeycomb structure. Graphene was believed to be unstable for a long time, but a few years ago it was successfully isolated. This led to the Nobel prize in physics in 2010 for Andre Geim and Konstantin Novoselov who pulled graphene layers from graphite using Scotch tape. Theoretical treatment shows graphene to have peculiar electronic properties (it is a zero-gap semiconductor and has a linear dispersion of electronic bands near the Fermi level), which resulted in the development of the field of graphene electronics. Furthermore, very high mobilities of $\sim 10,000 \text{ cm}^2/(\text{Vs})$ are observed,³ which makes it extremely useful for electronic applications. In addition to the promises of graphene itself, understanding its properties also is helpful in research on semiconducting materials with similar structure, such as silicene, which is a single sheet of silicon atoms arranged in a honeycomb structure.

Carbon-based materials usually have, in addition to the beneficial properties mentioned above, small spin-orbit coupling, due to the relatively low atomic mass of the constituting elements.⁴ In graphene hyperfine interactions are small as a result of the delocalised π -orbitals and very little nuclear spin. This suggests potentially very long spin-relaxation times, which allows for multiple spin operations before equilibrium is reached. Therefore, attention is drawn to organic spintronics, where organic materials are applied to transport and control spin polarised signals. The extra advantage especially is true for graphene and graphite, since these materials do not contain any heavy atoms. The advantages of organic materials mentioned before generally makes it cheaper to use organic materials rather than other materials. In very little cases all-organic devices are used. The devices actually are hybrid devices in which organic and inorganic materials are combined. Transport in organic materials is not as well understood yet as it is for the materials used in conventional electronics. Furthermore, large scale production of high-quality materials for conventional electronics currently is more reliable than it is for organic materials. Therefore these materials still are the standard.

Karpan *et al.* predicted perfect spin filtering in a system which exploits the beneficial properties offered by organic spintronics, in particular spintronics based on graphene/graphite.^{5,6} They theoretically treated a system consisting of a thin graphite film sandwiched between two ferromagnetic electrodes (in this case nickel or cobalt) of the same material. The lattices and electronic structures of these materials match in such a way that only electrons with a certain spin direction can be transmitted, which results in spin filtering.

The goal of this master assignment is to design, optimise and fabricate a device to test the theoretical prediction made by Karpan *et al.* This prediction has been studied before, but the proposed measurement technique has not been used yet. It is based on the splitting of the density of states of a superconductor for the two spin directions in a magnetic field, as predicted by Tedrow and Meservey.⁷ The realisation of such a device would allow for a practical way of perfect spin filtering to create a completely spin polarised current. Obvious applications are spin injection and spin detection, but the proposed spin filter can be applied in a very wide range of spintronic devices. For example, spin filtering in combination with one-electron quantum dots is proposed as the basis for a method to convert single spin into single charge measurements and provides an important ingredient for quantum computing.^{1,8} Quantum dots in the Coulomb blockade regime in a magnetic field are used to realise a spin filter and spin memory.^{9,10}

This assignment is performed in the NanoElectronics group of the University of Twente during the period between November 2013 and October 2014 under supervision of dr. ir. M.P. de Jong and ir. E. van Geijn. The work done will be presented in this thesis, which starts with a chapter on the theoretical concepts and a chapter concerning the experimental methods used. The design and the fabrication process will be explained, followed by the results obtained in the different experiments. Finally, conclusions will be drawn and recommendations will be made.

Chapter 2

Theory

This chapter offers to the reader the theory on which this report is based. First the basic concepts reciprocal space and density of states will be treated. After that the basic properties of graphene are discussed, followed by a treatment of the concepts of spin, spintronics, magnetism and magnetoresistance. Then the article in which the effect of interest is predicted will be discussed and to conclude the theory on which the measurement technique is based is explained.

2.1 Reciprocal space, energy and density of states

In addition to the (real space) crystal lattice of a material a so-called reciprocal lattice is defined. The wave vectors \mathbf{G} in the plane wave $e^{i\mathbf{G}\cdot\mathbf{r}}$ that yield a wave with the periodicity of the real lattice together form this reciprocal lattice. These reciprocal wave vectors \mathbf{G} connect the lattice points of the reciprocal lattice. The reciprocal lattice of a reciprocal lattice is the original lattice. Mathematically this is expressed as

$$e^{i\mathbf{G}\cdot(\mathbf{r}+\mathbf{R})} = e^{i\mathbf{G}\cdot\mathbf{r}} \rightarrow e^{i\mathbf{G}\cdot\mathbf{R}} = 1$$

for all \mathbf{R} , where \mathbf{R} is the set of lattice vectors of the crystal lattice and \mathbf{r} is the position vector. The Fourier transform of the spatial wave function is represented in this reciprocal space, which also is referred to as k-space or momentum space. Different points of specific interest, the so-called high symmetry points, are defined in k-space. Among them the centre of the Brillouin zone (Γ) and for hexagonal lattices i.a. \mathbf{K} and \mathbf{M} on the edges of the Brillouin zone. Reciprocal space especially is helpful for the interpretation of diffraction experiments and, in contrast to real space, has a direct relation with the energy levels in a material, as will become clear below.

The Schrödinger equation and the boundary conditions in a solid yield relations between the wave vector \mathbf{k} , momentum \mathbf{p} and energy E . The relation between momentum and energy is called the dispersion. States only exist for discrete wave vectors and thus energy values. Within a solid this results in continuous energy bands separated by band gaps. The number of states per unit of energy and unit volume as a function of energy is called the density of states (DOS). For example, for a parabolic dispersion corresponding to free electrons ($E(k) = \frac{\hbar^2 k^2}{2m_e}$) it can be shown that the 3-dimensional DOS is proportional to the square root of E .

In a metal all energy levels up to the Fermi energy (E_F) are filled, while the states above E_F are empty. Electronic conduction mainly is due to electrons at this Fermi level. The 3D generalization of the Fermi level is the Fermi surface, which is the constant-energy surface in reciprocal space corresponding to the occupied states with highest energy (the Fermi energy). If (for a particular wave vector) no states exist with energy equal to E_F there is no Fermi surface (associated with that particular wave vector). The Fermi surface can be projected on planes

in the crystal, which shows the states corresponding to the wave vectors associated with that particular plane.

2.2 Graphite and graphene

Graphite, the ground state of solid carbon, consists of several weakly bonded sheets of carbon atoms. Such a single sheet, in which the carbon atoms form a honeycomb structure of hexagons, is called graphene (or monolayer graphite).¹ This planar trigonal structure is the result of the sp^2 -hybridisation between a s-orbital and the two in-plane p-orbitals forming a σ -bond. The third p-orbital is not influenced by the hybridisation. It is perpendicular to the sheet and forms covalent bonds with neighbouring atoms forming a π -band. After filling the hybridised orbitals one electron per carbon atom remains, so each perpendicular p-orbital contains one electron and the π -band is half-filled. Graphene can be thought of as composed of benzene rings stripped from their hydrogen atoms.¹¹ Figure 2.1 schematically depicts the structures of graphite and graphene.

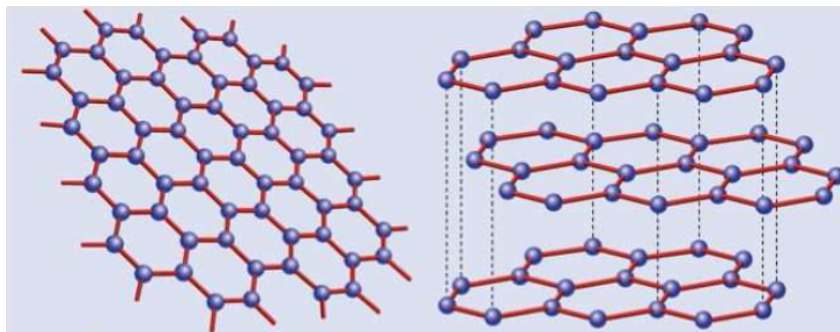


Figure 2.1 – Graphene (left) and graphite (right) both are carbon allotropes. Graphene is a single layer of carbon atoms with a honeycomb structure of hexagons and graphite consists of several graphene layers.¹¹

The hexagonal structure of graphene can be represented by a triangular lattice with a lattice constant $a \approx 1.42 \text{ \AA}$ and two atoms per unit cell. The tight-binding method can be employed to get an expression for the energy bands of graphene.¹¹ Figure 2.2 shows the lattice in real space, the corresponding reciprocal space and the energy spectrum for graphene.

In Figure 2.2 it can be seen that the \mathbf{K} and \mathbf{K}' points in reciprocal space, with $\mathbf{K} = (\frac{2\pi}{3a}, \frac{2\pi}{3\sqrt{3}a})$ and $\mathbf{K}' = (\frac{2\pi}{3a}, -\frac{2\pi}{3\sqrt{3}a})$, are of specific interest, because the Dirac cones are connected at these points.¹¹ Expanding the full band structure around these points gives a linear dispersion. The Dirac cones for electrons and holes touch each other at the Fermi energy and thus the Fermi surface for graphene is only formed by the \mathbf{K} and \mathbf{K}' points.

A system of more than one graphene layer, which thus strictly speaking is graphite, has a different band structure.¹¹ For a bilayer without a potential difference between the layers the material still does not have a gap, but more Dirac points exist. If a potential difference is applied a gap opens. Technological application may benefit from the ability to open a gap in bilayer graphene.

¹ Only in this theoretical section a clear distinction between graphite and graphene will be made. In the experimental work it is difficult to make the distinction and it is not of that much importance.

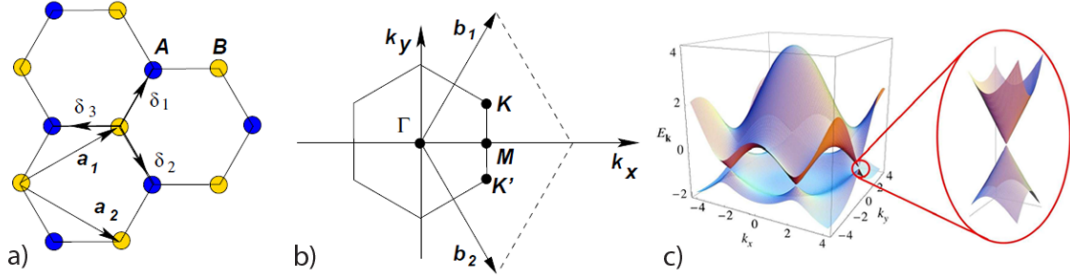


Figure 2.2 – Graphene (a) The lattice in real space with lattice vectors \mathbf{a}_1 and \mathbf{a}_2 . A unit cell contains two carbon atoms. (b) The corresponding reciprocal lattice with reciprocal lattice vectors \mathbf{b}_1 and \mathbf{b}_2 . The high symmetry points Γ , M , K and K' are indicated. (c) A 3D plot of the energy spectrum for graphene with a zoom of the dispersion around the K point. Adapted from Castro Neto et al.¹¹

2.3 Spin

In addition to its orbital angular momentum \mathbf{L} a particle has an intrinsic angular momentum, which is referred to as spin \mathbf{S} . The total angular momentum is given by $\mathbf{J} = \mathbf{L} + \mathbf{S}$. A particle has two quantum numbers related to spin, s (an intrinsic property) and m . For given s , m can take the $2s + 1$ values separated by unity between $-s$ and s : $m = -s, -s + 1, \dots, s - 1, s$. The magnitude of the total spin angular momentum is given by s : $\mathbf{S}^2 |sm\rangle = \hbar^2 s(s + 1) |sm\rangle$. The component of the spin along one of the quantization axes (usually the z -axis) is given by m : $S_z |sm\rangle = \hbar m |sm\rangle$. Intuitively spin can be thought of as the sum of the orbital angular momenta of the individual small mass elements building up the particle, which is the result of the rotation of a particle around its axis. However, for a structureless point particle, such as an electron, this analogy does not hold, since it is not composed of smaller elements. Quantitatively it gives impossible outcomes such as an infinitely high angular velocity. Nevertheless, spin also is called self rotation. For charged particles angular momentum, thus also spin, has a magnetic moment associated with it. The spin component of the magnetic moment is given by $\boldsymbol{\mu}_S = g \frac{q}{2m} \mathbf{S}$. Here g is a particle dependent dimensionless number known as the Landé g -factor and q and m are its charge and mass respectively.

For electrons $s = \frac{1}{2}$, so there are only two possible values for m , $\frac{1}{2}$ and $-\frac{1}{2}$. These states are referred to as spin-up and spin-down. The corresponding magnetic moment for electrons is in the direction opposite to the spin, due to its negative charge, and has magnitude $\mu_S \approx \frac{e\hbar}{2m_e} = \mu_B$, where μ_B is the Bohr magneton. The half-integer value for s means that electrons are fermions, so they obey Fermi-Dirac statistics and are subject to the Pauli exclusion principle. This principle requires the total wave function for a system to be anti-symmetric under exchange of particles, which also can be stated as: two particles can not occupy the same quantum state. The full wave function consists of a spatial part and a spin part and either the spatial or the spin part should be anti-symmetric, but not both, because then the total wave function again is symmetric. It can be shown that the average distance between electrons is different for the symmetric and anti-symmetric spatial wave functions. As a result, the Coulomb interaction between all constituents of atoms (both electrons and nucleus) is different for the two configurations and thus the energy depends on whether the state is spatially symmetric or anti-symmetric, which is equivalent to an anti-symmetric or symmetric spin-state. This is called the exchange interaction, but it is due to the Coulomb forces and there is no direct interaction. In a simple picture the exchange interaction favours parallel spin alignment in individual atoms, because the distance between electrons is larger, which reduces the Coulomb energy. Hund's rules determine the electron

configuration of the ground-state of multi-electron atoms more precisely, but these rules also have their limitations.

2.3.1 Spin-orbit coupling and hyperfine interaction

Spin-orbit coupling is a quantum mechanical relativistic effect. A particle moving at a relativistic velocity experiences a static electrical field as a magnetic field due to a Lorentz transformation. This magnetic component depends on the motion of the particle and interacts with the magnetic moment of a particle with non-zero spin. Spin-orbit coupling thus is an indirect coupling between an electric field and spin due to the orbital motion. The resulting energy shift causes the degeneracy of different spin states that would otherwise have the same energy to be lifted. This energy shift is part of the fine structure of the energy spectrum.

The electric field causing the coupling can have different origins of which the charged nuclei is one example. For hydrogen-like atoms spin-orbit coupling scales with Z^4 and in general it grows quickly with atomic number Z .⁴ Two other important contributions to spin-orbit coupling in solids can be identified, the Dresselhaus and the Rashba contribution, wherein the electric field is caused by asymmetry in the material. The Dresselhaus contribution is caused by the lack of bulk inversion symmetry (i.e. the crystal is changed by the operation $\hat{r} \rightarrow -\hat{r}$). This, for example, occurs in the zinc-blende structure and causes small potential steps in the material. Without inversion symmetry the energy of electrons depends on the direction of their movement. Electrons travelling in opposite direction with the same spin do not have the same energy, which means that the orbital motion and the spin of electrons are not independent. The Rashba contribution is related to structural inversion asymmetry, which for example occurs at surfaces and an interface between two materials. This result in an electric field.

The spins of the particles in a nucleus add up and yield a total nuclear spin, which can be zero, but also can have a finite value. A nucleus with non-zero spin forms a magnetic dipole, albeit with a much smaller dipole moment than that of an electron due to the larger mass of the nucleus. Hyperfine interaction is the interaction of the nuclear dipole moment with both orbital angular momentum and spin angular momentum of electrons. The latter contribution also is called spin-spin coupling. The origin is the motion of the charged electrons through the magnetic field directly generated by the nuclei.

2.3.2 Spintronics

Critical issues for spintronics are creating a spin polarised system, spin-transport and spin-detection. A system can be polarised by generating an unbalanced spin population. Traditionally orienting spins was done by means of optical techniques, but electrical spin injection is more favourable for practical applications.¹ Optically spins can be oriented by using circularly polarised light. Spin-orbit coupling then causes net angular momentum to be transferred from the photons to the electrons. For electrical injection of spins a ferromagnetic material is used, which possesses a spin dependent density of states. A current flowing from a ferromagnetic lead into a sample subsequently is spin polarised. The extent to which the current is polarised depends on the characteristic resistances (contact resistance and resistances of the two materials) involved.¹ This manifests itself clearly in what is known as the conductivity mismatch: due to the large difference in resistance a current flowing from a ferromagnetic material into a semiconductor usually has a negligible spin polarisation. Spin accumulation μ_s is the difference between the electrochemical potentials for the different spin orientations ($\mu_s = \mu_\uparrow - \mu_\downarrow$) and thus is not only dependent on the difference in number of majority and minority electrons (such as current polarisation and magnetisation), but also on the density of states for both types of electrons. It is important to note that an efficient spin injection (highly polarised current) does not always

lead to a large spin accumulation in the resulting system, while this is the measured quantity in several detection techniques. Both spin polarisation and accumulation usually decay inside a normal metal away from an interface with a ferromagnetic material.

Spin transport essentially is nothing more than the flow of a spin polarised current. However, spin is not a conserved quantity, so in the process of transport spin information can be lost. This will be discussed in more detail below.

Several methods exist for spin detection. Most of them do not directly measure spin, but rely on the measurement of signals that depend on the spin.¹ The method used in this work in that sense is not different and will be discussed in a next section.

Spin relaxation and dephasing

Since spin is a quantum mechanical property it is impossible to know the spin components both parallel and perpendicular to the quantisation axis. Spin can be said to have an orientation along a quantisation axis around which it precesses. A phase is associated with this precession. Spin information (orientation and phase) is lost in several processes in which spin equilibration takes place. Spin relaxation is the loss of a collective spin orientation along the quantisation axis due to the individual spins taking different orientations in scattering processes. Usually spin is conserved in scattering, but processes exist in which angular momentum is transferred and the electron spin is changed. Spin dephasing is, as the term already suggests, the loss of phase coherence of a spin ensemble as a result of fluctuations in the precession frequency. The time and length scales of these processes are of importance for spintronic applications. Important mechanisms of spin relaxation and dephasing in metals and semiconductors are Elliot-Yafet, D'yakonov-Perel', Bir-Aronov-Pikus and hyperfine interaction. These mechanisms will be discussed below. For the following the works of Žutić et al.¹ and Naber et al.⁴ are used as a reference. These reviews contain a more detailed description of the different mechanisms and the first article also contains a mathematical description.

The first three mechanisms mentioned above all originate from spin-orbit interaction. Momentum scattering can cause a change in the electron spin if the orbital motion and the spin of an electron are coupled. These mechanisms directly affect spin relaxation and have an indirect effect on spin dephasing. Elliot-Yafet (also called spin-flip scattering) results from the mixing of the Pauli spin-up and spin-down states in the Bloch states in a material in the presence of spin-orbit interaction. This implies that momentum eigenstates are no spin eigenstates. In that situation momentum scattering can be accompanied by a flip of the electron spin. The Dresselhaus contribution to spin-orbit coupling plays a role in the D'yakonov-Perel mechanism. The non-degeneracy of states with the same momentum but different spin directions (which in this case are eigenstates) leads to randomisation of the quantisation axis due to scattering. The last mechanism, Bir-Aronov-Pikus, occurs in p-type semiconductors and involves electrons and holes that can exchange their spin. The hole subsequently undergoes relatively fast spin relaxation as a result of stronger spin-orbit coupling for holes in the valence band than for electrons in the conduction band, which is caused by the larger effective mass for holes. This, for example, occurs in p-doped silicon. The total spin then is changed compared to before the spin exchange between electron and hole.

Hyperfine interaction causes spin relaxation as a result of exchange of spin between electrons and nuclei and spin dephasing due to fluctuating nuclear spins. Delocalised electrons are influenced by many nuclei. In that case the random nuclear spins average out. Therefore, hyperfine interaction is strongest for localized electrons.

Organic materials usually consist of light elements (in particular carbon) and therefore have a small spin-orbit interaction. Theoretical treatment of graphene show both intrinsic and Rashba

spin-orbit coupling to be very small.^{12,13} In both articles a typical electric field is assumed to estimate the strength of the Rashba contribution, but its actual value will depend on the environment. The most abundant carbon isotope (^{12}C) has zero nuclear spin, so no hyperfine interaction takes place for these atoms. Other isotopes, such as ^{13}C , and other elements like hydrogen and nitrogen do have non-zero nuclear spin and can cause important effects related to hyperfine interaction. However, their effect is small in most cases. In graphene electrons are delocalised, so also hyperfine interaction is small. This leads to the conclusion that in organic materials long spin lifetimes are expected, which allows for multiple operations before equilibrium is reached.⁴

2.3.3 Ferromagnetism and nickel

The exchange interaction favours parallel spin alignment on individual atoms, which is reflected in Hund's rule that the spin is maximized in free atoms. In a solid-state system the exchange interaction also affects the alignment of spins on neighbouring atoms, which depends on the interatomic distance and the spatial distribution of the wave functions of the states that take part in the magnetic behaviour. Which of the orientations, parallel or anti-parallel alignment (or more formally the triplet or singlet configuration), is energetically more favourable depends on the details of the system. For the 3d transition metals iron, cobalt and nickel parallel alignment is favoured, which results in a non-zero magnetization. This is called ferromagnetism.

The preference for parallel alignment is reflected in a down shift in energy for one of the spin directions relative to the energy for the other spin direction. As a result the DOS is asymmetric (spin polarised) for the two spin orientations and the energetically favorable spin orientation is more abundant. Whether spin-up or spin-down (or any other orientation) is favoured depends on the history of the system. Usually the two orientations are referred to as majority and minority electrons. The system is spin polarised and in general the DOS of the two spin directions have different values at the Fermi level. This is depicted for nickel in Figure 2.3.

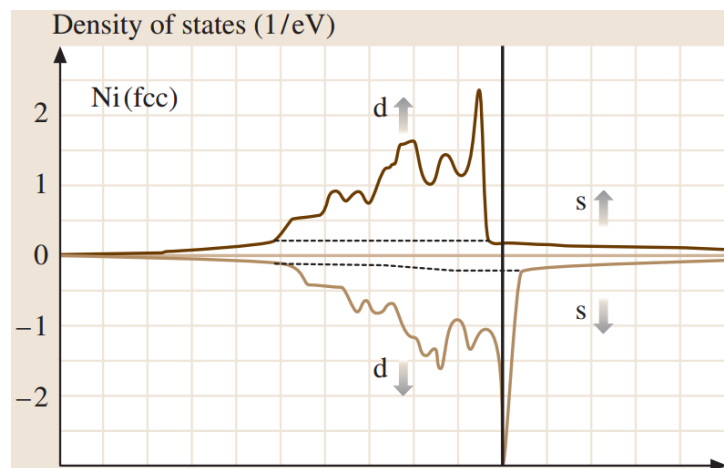


Figure 2.3 – Spin dependent density of states for nickel as obtained from numerical calculations using the linear muffin-tin orbital (LMTO) method. For the majority electrons (here indicated by an up arrow) the Fermi level is above the 3d states, while it crosses these states for the minority electrons (down arrow).¹⁴

The Fermi surface projection for the close-packed (111) surface of the FCC lattice of nickel (Figure 2.4) shows that there are no majority spin states close to the K point in reciprocal space whereas minority spin states exist (almost) everywhere in the surface Brillouin zone.

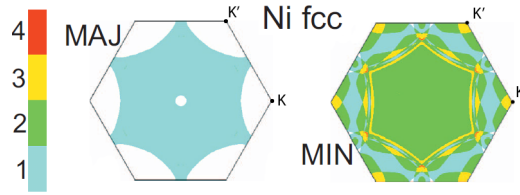


Figure 2.4 – Fermi-surface projection onto the close-packed plane Ni(111) for both majority and minority spin. The colour bar indicates the number of Fermi-surface sheets. The \mathbf{K} and \mathbf{K}' are located at the corners of the hexagons. Adapted from Karpan *et al.*⁶

2.3.4 Magnetoresistance

Magnetoresistance is the effect of a change in resistance as result of a changing magnetic field. There are many different types of magnetoresistance, which have different physical origins and are related to different device structures. Examples are ordinary magnetoresistance, giant magnetoresistance (GMR) and tunnelling magnetoresistance (TMR). The behaviour of GMR and TMR is quite similar, but, again, the physics is different. The model commonly used to explain magnetoresistance effects will be presented below and tunnelling magnetoresistance will be discussed as an example.

Two current model

Scattering events limit the transport of electrons. In these events both wave number and energy can be affected, but events in which the spin of electrons is flipped are rare. This lead N.F. Mott to the assumption that the spin orientations are effectively decoupled and the current can be assumed to be the combination of independent contributions for both spin orientations.¹⁵ This is justified for systems in which the spin relaxation length is much larger than the typical length scale of the system. The system can then be modelled by a network with parallel resistors for the majority and minority electrons.

According to Fermi's golden rule the scattering probability is related to both the matrix elements connecting initial and final states and the density of final states. Since conduction mainly takes place at the Fermi level the DOS at the Fermi level is important for the conductance. This explains why there is a difference in resistance for the majority and the minority channel in a ferromagnet. The current in a ferromagnet thus is spin polarised.

The model, adjusted by Campbell *et al.* (1967) and Fert and Campbell (1968), has shown to be very useful in explaining magnetoresistance.

Tunnelling magnetoresistance

Tunnelling magnetoresistance (TMR) is an effect occurring in a magnetic tunnel junction (MTJ), which consists of two ferromagnetic (FM) leads separated by an insulating layer. As in scattering, also in tunnelling spin flips are rare and spin is preserved. The tunnelling probability depends on the number of empty final states (Fermi's golden rule), but also on the number of filled initial states. These facts can be used as an intuitive explanation for TMR. As a result of the spin polarised DOS in ferromagnets the tunnelling current also is spin polarised. Furthermore, the resistance is different for parallel (P) or anti-parallel (AP) alignment of the ferromagnets. This is because for the P case majority (minority) electrons in one FM are also majority (minority) electrons in the other FM, but for the AP situation majority (minority) electrons in one electrode become minority (majority) electrons while tunnelling to the other electrode. Both the spin polarisation and the dependence on alignment of the FMs are depicted in Figure 2.5. In reality

the physics involved is more sophisticated than this, but it serves to give a feeling for the origin of tunnelling magnetoresistance.

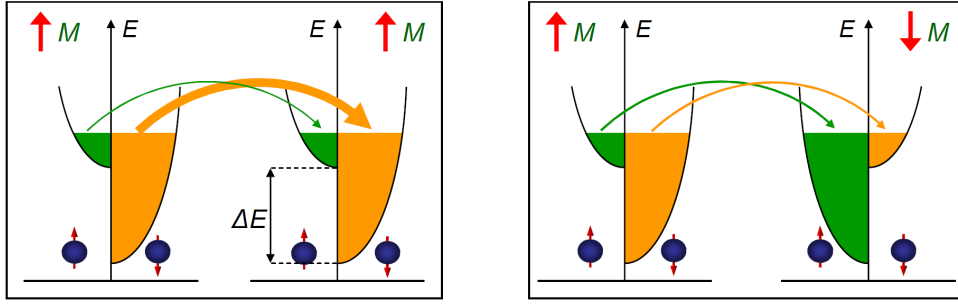


Figure 2.5 – Tunnelling between two ferromagnetic leads. In the case of parallel alignment (left) a low resistance channel exists for the majority electrons (orange), while the minority electrons experience a large resistance (green). For the anti-parallel case a low resistance channel is absent, because there are either only a few initial or final states. Source: Compendium NanoElectronics by Michel de Jong.

2.4 Spin filtering at interfaces between nickel close-packed surfaces and graphene

Karpan *et al.* combined the properties of graphene/graphite and ferromagnetic materials to predict perfect spin filtering at interfaces between ferromagnetic materials and graphite. They theoretically treated systems of a thin graphite film sandwiched between two (111) surfaces of nickel or cobalt. The results are published in *Physical Review Letters* in 2007⁵ and more elaborately in *Physical Review B* in 2008.⁶ Such a system is an example of carbon spintronics and would be very helpful in the further development of this field. The surface lattice constants of nickel and cobalt match the in-plane lattice constants of graphene and graphite almost perfectly. For the Ni(111)|Gr interface the lattice mismatch is only 1.3%. Fermi-surface projections can be directly compared in the case of perfect lattice matching, which is a reasonable approximation for a Ni(111)|Gr interface. As explained in section 2.2 there are only states available in graphene at the \mathbf{K} (and \mathbf{K}') point in reciprocal space.

The comparison of the Fermi surface projection for Ni(111) (as shown in Figure 2.4) with that of graphene suggests no transmission of majority electrons, while minority electrons can be transmitted. This is depicted in Figure 2.6. If the graphite film is thick enough, such that tunnelling can be neglected, perfect spin filtering is expected. There are several methods to measure this effect and one of them is a second ferromagnetic layer at the other side of the graphite layer. For parallel magnetisation majority (minority) electrons on one side of the graphite also are majority (minority) electrons on the other side. In that case there is a conduction path for the minority electrons and a current can exist. For anti-parallel alignment the conductance vanishes, since majority (minority) electrons on one side are minority (majority) electrons on the other side and there is no conduction path available for any of the electrons. This results in an exponentially high magnetoresistance effect (close to 100% in the pessimistic definition²) that saturates to a value independent of the number of layers.

The strong interaction at an interface between graphene and nickel destroys the characteristic electronic structure of graphene for the lowest energy configuration, but calculations show that this is not the case for a sandwich geometry. Karpan *et al.* investigated the influence of lattice

² Pessimistic definition magnetoresistance: $MR = \frac{R_{AP} - R_P}{R_{AP}} \times 100\% \equiv \frac{G_P - G_{AP}}{G_P} \times 100\%$

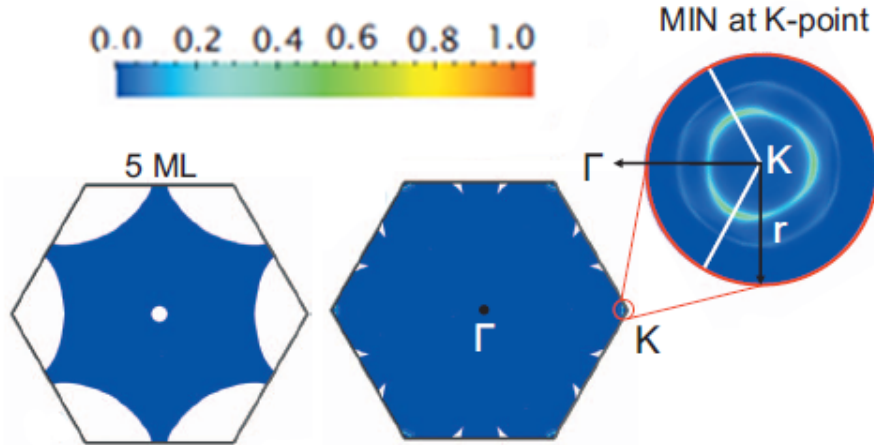


Figure 2.6 – Transmission for five layers of graphite between two Ni(111) surfaces. For both majority (left) and minority (middle) the transmission is low. The only non-negligible transmission is for the minority electrons around the K point as is depicted in the magnification on the right. Adapted from Karpan et al.⁶

mismatch, interface roughness and interface disorder. An upper limit for the effect of lattice mismatch was obtained by matching 19 x 19 unit cells of Ni to 20 x 20 unit cells of graphite, which corresponds to a mismatch of 5%. Interface roughness and disorder was modelled by removing a certain percentage of the top layer atoms and incorporating a certain amount of copper atoms in the surface layer respectively. This leads to the conclusion that the lattice mismatch should not be a limiting factor (magnetoresistance decreases from 100% to 90% in the pessimistic definition). Interface roughness of 50% reduces the magnetoresistance to about 70% and a single surface layer of Ni₅₀Cu₅₀ results in a reduction to 90%. The predicted magnetoresistance effect should be relative insensitive to both roughness and disorder. This makes the effect promising for spintronics applications.

2.5 Spin polarisation measurements: Tedrow-Meservey

The measurement of spin polarisation has been subject of different studies and several methods can be used. For example tunnelling between two ferromagnetic materials with a well-defined polarisation of one of the electrodes. Tedrow and Meservey investigated the tunnelling between thin films of superconducting aluminium and ferromagnetic materials. They found the tunnel current to be spin polarised and developed a model to explain their observations. This shows that thin superconducting films can be used to determine the spin polarisation of a current.⁷ Due to the long coherence length in superconductors it is the most unambiguous method to measure the spin polarisation of a tunnelling current.¹⁰ An intuitive explanation of the principle behind this type of measurements is given in section A.1.

The DOS of a superconductor shows an energy gap and sharp peaks at the edges of this gap. In a magnetic field the energy levels of spin-up and spin-down electrons are shifted due to Zeeman-splitting and the result is a spin-dependent DOS as is depicted in Figure 2.7. For this purpose superconductivity should not be quenched by applying the necessary magnetic field. The critical field of very thin aluminium films is increased by several orders of magnitude in comparison with the bulk value,¹⁶ which makes it a suitable material for this kind of experiments. For non-magnetic metals, in which the numbers of spin-up and spin-down electrons are equal, this still results in a tunnelling current which is symmetric in bias voltage. However, for ferromagnetic

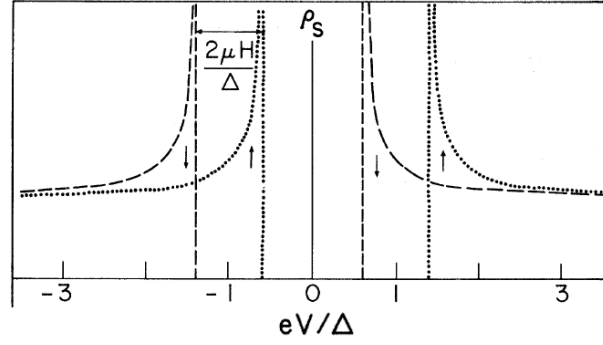


Figure 2.7 – Density of states for a superconductor showing an energy gap of width 2Δ . In the presence of a magnetic field the energy levels for spin-up (dotted) and spin-down (dashed) are shifted up and down by μH respectively (μ is the electron’s magnetic moment). This results in an energy difference of $2\mu H$ between the two spin directions. Adapted from Tedrow and Meservey.⁷

metals spin-up and spin-down electrons contribute differently to the tunnel current due to the spin-dependence of the DOS (correcting for the energy shift still gives a different contribution), which results in an asymmetric conduction around $V = 0$.⁷ Figure 2.8 shows the theoretical normalised conductance for tunnelling between a superconductor and both a normal and a ferromagnetic metal.

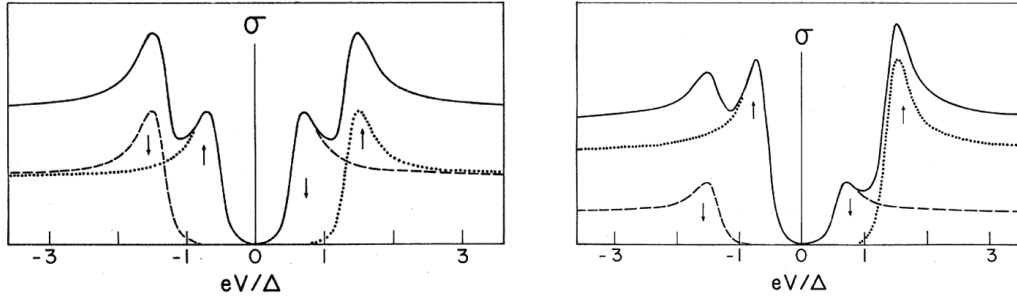


Figure 2.8 – Theoretical normalised conductance for superconductor-normal metal tunnelling (left) and superconductor-ferromagnet tunnelling (right). Dotted and dashed lines indicate the spin-up and spin-down conductances respectively, while the solid lines corresponds to the total conductance. Adapted from Tedrow and Meservey.⁷

The conductance curves measured in the presence of a magnetic field can be used to obtain a value for the spin polarisation P and an expression for the unsplit conductance function in the absence of the magnetic field, $f(x)$.⁷ The imbalance in the number of spin-up and spin-down electrons is expressed by $a = \frac{n_\uparrow}{n_\uparrow + n_\downarrow}$. The polarisation is then defined as

$$P \equiv \frac{n_\uparrow - n_\downarrow}{n_\uparrow + n_\downarrow} = 2a - 1 \quad (2.1)$$

Referring to Figure 2.9 for the σ_i ’s and the measured total conductance curve $F(x)$ (solid line), a and $f(x)$ can be calculated by

$$a = \frac{\sigma_4 - \sigma_2}{\sigma_4 - \sigma_2 + \sigma_1 - \sigma_3} \text{ and } f(x - h) = \frac{aF(x) - (1 - a)F(-x)}{2a - 1} \quad (2.2)$$

This analysis only holds if spin-orbit interaction can be neglected both in the superconductor and the tunnel barrier, which is experimentally shown to be true for Al-Al₂O₃-Al junctions.¹⁷ If

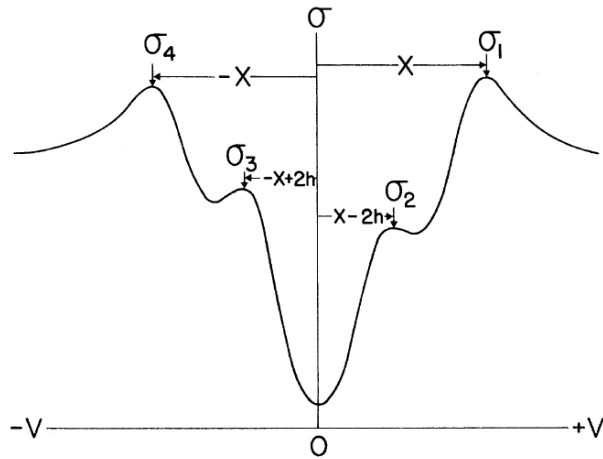


Figure 2.9 – Chosen values for the σ_i 's to determine the polarisation a and original conductance curve $f(x)$.⁷

spin-orbit coupling can not be neglected the DOS for the different spin orientations is not the same function of energy.

Meservey and Tedrow investigated different aspects of spin polarised electron tunnelling.¹⁸ For materials to be suitable for the type of measurement described above they should be able to withstand quite high magnetic fields, such that electron spin effects (like Zeeman splitting of the density of states) are the dominant response to a magnetic field. In order to achieve this orbital depairing as the result of circulating currents (the Meissner effect) should be small. Orbital depairing is shown to be suppressed in thin films, because the magnetic field penetrates the film almost uniformly, such that screening currents are minimal. In addition, as already mentioned, spin-orbit coupling should be small to be able to neglect the effect of spin mixing. Aluminium is a relatively light element, so spin-orbit coupling is not too strong, and has the advantage that very thin layers can be easily made. In 1983 Meservey *et al.* wrote: '*It happened that the only common superconductor in which the spin-orbit interaction was small enough to closely approximate a BCS superconductor in its spin properties was Al*'.¹⁹ Other materials exist that satisfy the aforementioned requirements, but in most, if not all, cases these materials have other disadvantages.

Chapter 3

Experimental methods

Scientific research is based on a wide variety of techniques to fabricate, characterise and measure samples. The work done for this thesis is not different, so several techniques are used. This chapter gives an overview of the most important techniques used in this project, which serves as a background on how the devices are fabricated, as will be explained in chapter 4, and on the experimental results that are presented in chapter 5. As general reference *The Materials Science of Thin Films* by M. Ohring²⁰ is used for this chapter.

3.1 Fabrication

The samples are fabricated in the cleanroom of the MESA+ Institute for Nanotechnology located in the Nanolab building on the campus of the University of Twente. In the cleanroom advanced equipment is available for device fabrication. Below, the techniques used in this work are explained.

3.1.1 Photolithography

Photolithography is a technique utilised to define (small) structures on a sample. The obtained structures can consist of several layers and the geometries can be of varying complexity. It is not a main technique for construction, but supports other techniques.

The main principle behind photolithography (which is Greek for 'writing with light') is the reaction of polymers to light. These polymers are dissolved in a solvent to obtain what is called photoresist. A layer of resist is applied to a sample and subsequently heated to evaporate the solvent and promote substrate adhesion. Exposure to light through a mask causes a reaction to occur in the resist. This reaction either strengthens or weakens the resist. Photolithography is finished by development, which removes the parts of the resist that are soluble in the developer from the sample. What is a suitable developer depends on the used resist. Which parts of the resist are soluble and which are not depends on the type of resist and on the mask used during exposure. The mask determines which parts are exposed and which are not. Photoresist exists in two types, positive and negative resist. These names refer to the image obtained after development. Positive resist becomes soluble by exposure, while negative resist becomes insoluble. As a result, for positive resist the exposed parts are removed during development, which creates a positive image of the mask pattern, while for negative resist the exposed parts remain on the sample, which creates a negative image. After development several etching techniques can be used to transfer the image in the resist layer to the sample. This results in a structured layer on the sample. The next step in the fabrication process can be performed after removing the

remaining resist. This can be another photolithography step or a different technique can be used. The process of photolithography is depicted in Figure 3.1.

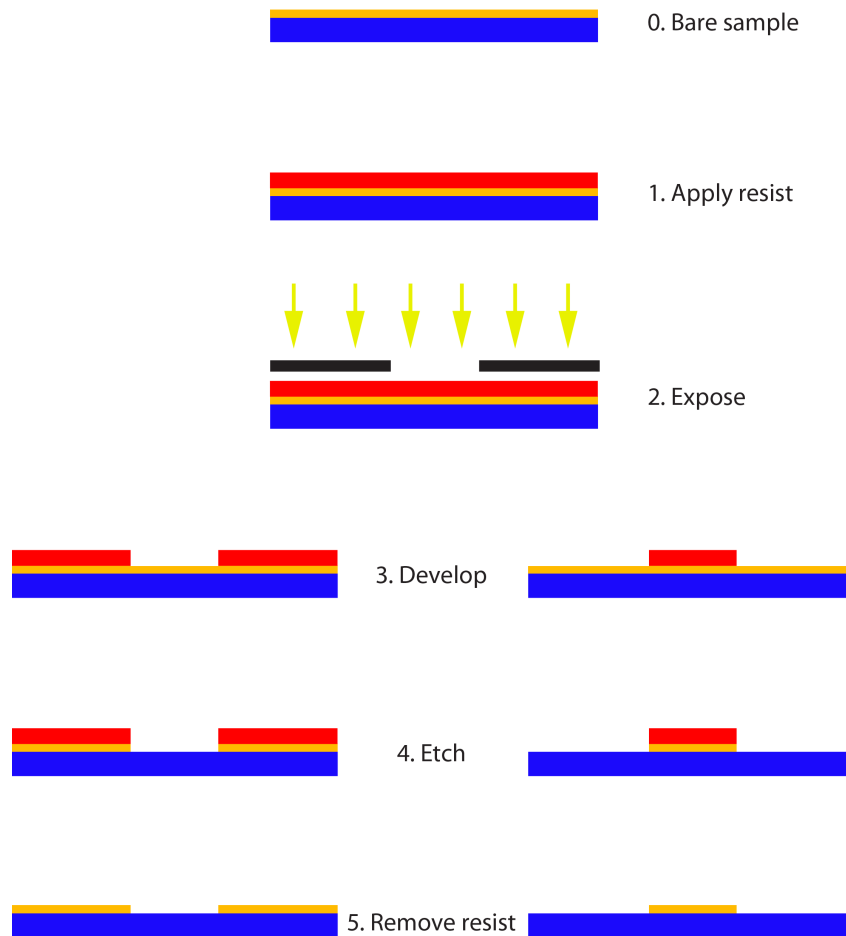


Figure 3.1 – Process flow for photolithography. In this example a bare sample consist of a substrate (blue, often silicon is used) and a layer of another material (orange, for example nickel). Photoresist (red) is applied to a sample (1) and exposed though a mask (2). Development results in either a positive image of the mask for positive resist (3, left) or a negative image in the case of negative resist (3, right). Etching (4) and removing the remaining resist (5) transfers this image to the sample and a structured layer is obtained.

An alternative photolithography method is lift-off in which a layer is deposited on top of the developed resist layer. Subsequently, the remaining resist is removed, which takes along the material on top, while the material remains on the sample where there is no resist left after development. As an advantage of this technique no destructive method as etching is needed. No lift-off lithography is used for this project.

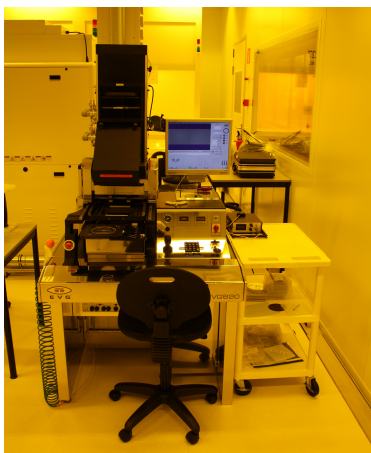
The minimum feature size that can be obtained by photolithography is limited by the used optics, the wavelength of the light and the choice of process parameters, e.g. the type and thickness of the resist and the contact mode. The equipment available in the MESA+ cleanroom limits the feature size to the order of one micrometer.

In this work exposure is done in an EV620 Bond Aligner made by EVG Japan. This machine uses a broadband Hg light bulb to create light in the near UV range 350-400 nm with an intensity of 12 mW/cm². A photo of this system is shown in Figure 3.2(a).

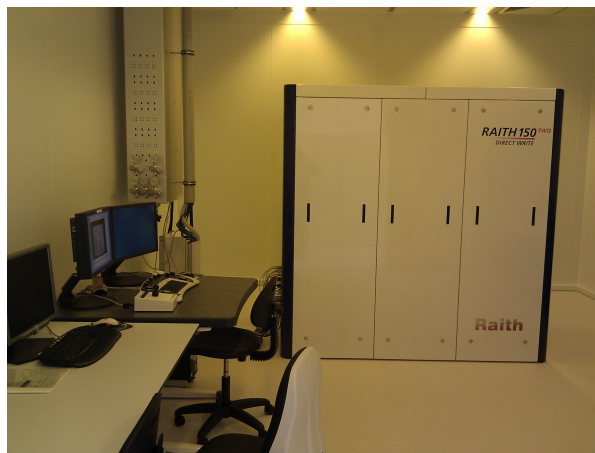
3.1.2 Electron beam lithography

The working principle of electron beam lithography (EBL) is the same as for photolithography, but the polymers used in the resist are sensitive to exposure by electrons. In contrast to photons, electrons have a non-zero mass and according to De Broglie their wavelength is given by $\lambda = \frac{h}{\gamma m v}$, where γ accounts for relativity. The wavelength of electrons in general is smaller than the wavelength of light, which makes it possible to obtain a higher resolution and define smaller structures. An extra advantage of EBL is the ability to write without a mask, which makes it possible to adjust the pattern each time it is written. Because of the smaller length scale involved in EBL several points require extra attention. Among them are alignment and the applied dose.

In the MESA+ cleanroom a RAITH150-TWO is available which uses a maximum acceleration voltage of 30 kV and is able to write structures down to 10 nm. A photo of this system is shown in Figure 3.2(b).



(a) EV620 Bond Aligner for exposure in the photolithography process



(b) RAITH150-TWO for exposure in the EBL process

Figure 3.2 – Lithography equipment in the MESA+ cleanroom. Photos by the MESA+ cleanroom staff.

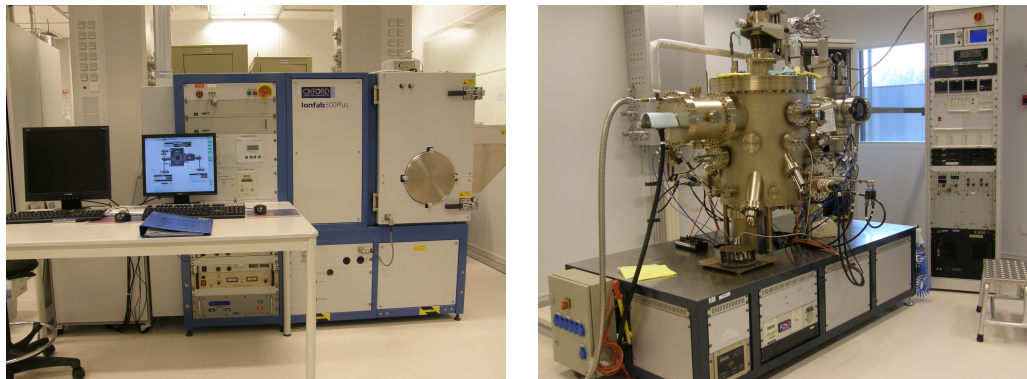
3.1.3 Ion beam etching

A common method for etching away material is (reactive) ion beam etching, (R)IBE, which is a form of dry etching (no liquid etchant is used). In addition, also wet etching techniques exist. For ion beam etching electrons are liberated from a filament by heating in an ultra-high vacuum (UHV) chamber. Ions are created from neutral atoms by bombardment with these electrons and form a plasma. Argon gas is a common source of these ions. The ions are accelerated towards the sample by means of an electric field. The impinging ions erode the sample of which parts can be protected by a layer of photoresist or an etch mask. The amount of etched material can be controlled by the process parameters and the etching time. It also strongly depends on the material being etched.

For reactive ion beam etching reactive gases, such as oxygen and nitrogen, can be deliberately added to the process chamber. In this case a plasma with reactive ions is created and reactions take place during etching.

An Oxford Instruments Ionfab[®]300Plus, shown in Figure 3.3(a), is used for etching. The

system is equipped with a secondary ion mass spectrometer (SIMS) for element and endpoint detection. Both the option of reactive etching and the SIMS are not used.



(a) Oxford Instruments Ionfab®300Plus system for (reactive) ion beam etching (b) DCA Instruments M600 system for electron beam evaporation

Figure 3.3 – Equipment in the MESA+ cleanroom. Photos by the MESA+ cleanroom staff.

3.1.4 Electron beam evaporation

Electron beam evaporation is a technique used in materials science to deposit thin films in an UHV environment. Electrons are thermally emitted from a filament by resistive heating. A combination of an electric field and a magnetic field serves to both accelerate and deflect the electrons. The electron beam is focused on the target, which is mounted in a cooled crucible, to evaporate the material. This way the target is locally heated, which eliminates the disadvantage of contamination by material originating from the used equipment (e.g. crucibles). Furthermore, there is no power limitation as in resistively heated evaporation, so virtually all materials can be evaporated at nearly any rate. The sample is mounted such that it faces the target and a shutter is placed in between the target and sample to control the film formation.

In this project electron beam evaporation is done in the DCA Instruments M600 system, which is available in the MESA+ cleanroom and property of the NanoElectronics group. The system has a base pressure in the order of 10^{-10} mbar and is equipped with two e-beam evaporators and two effusion cells, which offers the possibility to deposit several different materials. Growth rate monitors (quartz microbalances) are used to control the film thickness. In-situ oxidation can be done in the load lock (base pressure 10^{-7} mbar) by filling it with O_2 gas using a mass-flow controller. For plasma oxidation an oxygen plasma can be created by a DC power source. The system is shown in Figure 3.3(b).

3.2 Characterisation

Besides the cleanroom facilities the MESA+ Nanolab also houses a variety of techniques for analysis. The analytical techniques used for this assignment are explained in this section. Not all the labs offering these techniques are in the Nanolab building. Some of them are located in the labs in the Carré building.

3.2.1 Atomic force microscopy

An atomic force microscope (AFM) employs the force between the sample and a sharp tip with a radius on the order of 10 nm to obtain an image of the sample. The forces that are most

important depend on the sample. Amongst their origin are Van der Waals forces, electrostatic forces, magnetic forces and chemical bonds. An AFM tip, which is attached to a cantilever, is brought close to the sample. Forces between the tip and the sample cause the cantilever to deflect, which is measured by the change in reflection angle of the laser beam that is focussed onto the cantilever tip. The changing angle is monitored with a photodiode. An AFM can be used in different modes of which contact mode, non-contact mode and tapping mode are the most widely used. The measurements done here are done in tapping mode. The cantilever oscillates close to its resonance frequency and meanwhile gently taps the tip on the surface. The oscillation amplitude depends on the forces acting on the cantilever. To obtain a map of the sample the tip is scanned over the surface, while a feedback loop keeps the distance (force) between tip and sample constant. A schematic drawing of an AFM is depicted in Figure 3.4. For this project a Veeco DI3100 AFM is used to make topographic maps of the samples.

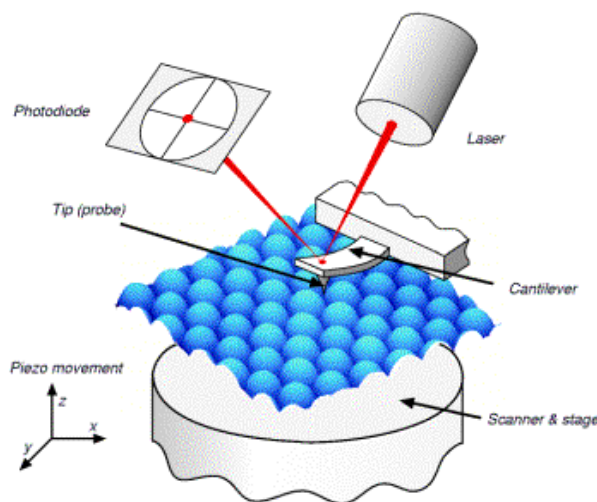


Figure 3.4 – Atomic force microscope. Source: www.farmfak.uu.se (courtesy of YKI).

3.2.2 Raman spectroscopy

Raman spectroscopy is a method to obtain information on vibrational and rotational modes in a material by means of inelastic scattering of monochromatic light. The probed modes are low-frequency modes (only the first few excited modes play a role) and vibrational modes are more important than rotational modes. Only in the gas phase rotations have much influence, which give rise to rich spectra with many peaks close to each other. Changing into the liquid phase suppresses rotations in molecular collisions. In Raman spectroscopy a laser with a frequency in between the vibrational and electronic frequencies is used to illuminate a material, which results in the material being excited to virtual (unstable) states. The used light usually is in the visible part of the spectrum, which corresponds to a wavelength of 10^{-6} - 10^{-7} m and an energy of a few eV. The radiation frequency is much higher than the frequency of the involved vibrational states, which are in the infrared part of the spectrum, so no direct transition to the vibrational excited state occurs. Depending on the initial and final states involved three events can take place: elastic (Rayleigh) scattering in which the molecule returns to its initial state, relaxation to a state with higher energy than the initial state (Stokes Raman scattering) and relaxation to a lower energy state in anti-Stokes Raman scattering.³ These effects are schematically depicted

³ Note: Rayleigh scattering is not the same as infrared scattering in which the excited state is a real vibrational (or rotational state) with higher energy, while in Rayleigh scattering the excited state is a virtual state. The

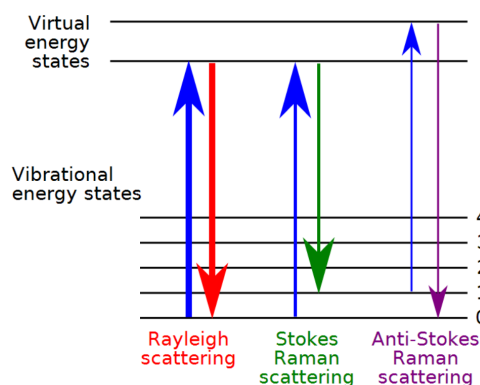


Figure 3.5 – Energy diagram indicating the process of Rayleigh scattering, Stokes Raman scattering and anti-Stokes Raman scattering. Adapted from wikipedia.org (courtesy of Moxfyre).

in Figure 3.5. The cross section for both Stokes and anti-Stokes Raman scattering usually is small and elastic Rayleigh scattering strongly dominates. The two former effects, which are both inelastic scattering effects, are used in Raman spectroscopy, while elastically scattered photons are filtered on purpose. Both inelastic effects result in a shift in energy, and thus the frequency, of the photon. Stokes Raman scattering is associated with a lower frequency, while anti-Stokes Raman scattering causes a higher frequency. The resulting frequency shifts are caused by the difference in energy between the vibrational states (i.e. the phonon frequencies) of the system and are characteristic for a material. Phonon frequencies depend for example on chemical composition and structural properties, which thus can be investigated with this technique. Raman spectra usually are reported as a graph of intensity vs. relative wave number: $\sigma(\text{cm}^{-1}) = \frac{10^7}{\lambda_{exc}} - \frac{10^7}{\lambda_{sc}}$. Here λ_{exc} and λ_{sc} are the excitation wavelength and the wavelength of the scattered light respectively. Both are in nm. In these spectra peak positions depend on molecular weight and bond strength, their width is related to the dynamics in the scattering process and the amplitude corresponds to the scattering cross section, which in turn depends on (the change in) the polarisability of the material involved. Raman shifts are practically independent of excitation energy, but the cross section (and thus the intensity) varies as λ^{-4} . In some cases the shifts however do depend more strongly on excitation energy, because the momenta of the phonons involved depend on the excitation energy.²¹ This is the result of coupling of phonon wave vectors to the electronic structure in double resonance processes.²²

Special measures, such as filters and other instruments, are used to reduce the signal originating from Rayleigh scattering and improve the Raman spectra. Several techniques exist to enhance the Raman signal of which stimulated Raman and coherent anti-Stokes Raman spectroscopy (CARS) are examples. Both techniques have the limitation that only one Raman active mode is probed. In CARS this mode can be tuned, but stimulated Raman is limited to the strongest mode only.

Raman spectroscopy is done in two experimental set-ups. The first set-up is located in the Carré building on the University of Twente and is property of to the Medical Cell BioPhysics (MCBP) group. The other belongs to the company HybriScan Technologies[®] of which Cees Otto from the MCBP group is one of the founders. This set-up integrates a Raman spectrometer with an optical and a scanning electron microscope, which offers the possibility to correlate the different types of measurements in the same system.

frequency of the involved radiation also is different.

Graphene

Since the discovery of graphene Raman spectroscopy developed into one of the general techniques to characterise its properties, such as number of layers, stacking order, disorder and doping. A detailed study of available literature has been done to determine the possibilities to investigate different properties of graphene. In the near future this will be useful for the NanoElectronics group, because it will become possible to grow graphene in the MESA+ cleanroom in a newly purchased CVD furnace. A broad overview of the possibilities of Raman spectroscopy in graphene research will be given here. The experimental results used in this project are discussed in subsection 5.1.2.

A typical Raman spectrum for both monolayer graphene and graphite is shown in Figure 3.6. The graphene spectrum consist of two main peaks: the G (for graphite) peak around $\sim 1580 \text{ cm}^{-1}$ and the 2D peak (or G') around $\sim 2700 \text{ cm}^{-1}$. A smaller peak exist around $\sim 2450 \text{ cm}^{-1}$. This peak is named G*.²¹ The D (for defect) peak can exist around $\sim 1350 \text{ cm}^{-1}$, but is not always present as is the case in the image shown here. This peak also is important for a general analysis. It should be noted that only the D and G peak always have the same label. Other peaks can have more labels and there is no consensus concerning their usage. Sometimes different people even use the same label for different peaks.

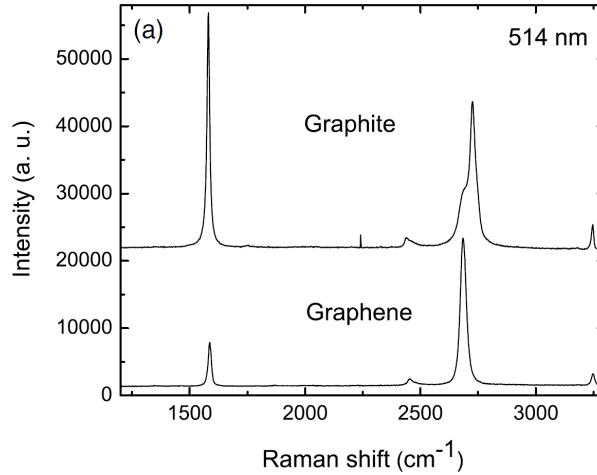


Figure 3.6 – Typical Raman spectra for (defect-free) monolayer graphene and graphite at 514 nm scaled to have similar height of the 2D peak. The G ($\sim 1580 \text{ cm}^{-1}$) and 2D ($\sim 2700 \text{ cm}^{-1}$) peaks are clearly visible. Source: Ferrari et al.²²

The G peak stems from the emission of an optical phonon with zero wave vector from the Γ point and is the only one-phonon process allowed in clean graphene. The D peak is defect induced and related to emission of an optical phonon near the \mathbf{K} or \mathbf{K}' points at the boundary of the Brillouin zone.^{22,23} Momentum conservation implies that the sum of the wave vectors of the involved phonons should be equal to the wave vector transferred in the light scattering event. The transferred wave vector obviously can not be larger than the excitation wave vector. The zone-boundary wave vector is approximately 1000 times larger than this excitation wave vector, so one-phonon processes at the zone boundary are not allowed in defect-free graphene. However, the second order⁴ of the D peak, the 2D peak, is visible, because it involves two phonons with essentially equal and opposite wave vectors near the \mathbf{K} and \mathbf{K}' points.²⁴ In that case momentum is conserved, because the small difference in magnitude between the wave vectors of these phonons

⁴ Second order means nothing more than a double Raman shift, so has nothing to do with the frequency of the involved phonons.

matches the transferred wave vector. For the 2D peak also the label G' sometimes is used, because the peak is not induced by defects. The D' peak, at 1620 cm^{-1} , also is induced by defects and is related to optical phonons with a small wave vector. A peak at 3250 cm^{-1} stems from the emission of two phonons with opposite wave vector near the Γ point in the center of the Brillouin zone and therefore referred to as the 2G peak. 2D' also is used sometimes for this peak to reflect the fact that its frequency is double the frequency of D'.²³

The intensity of the D peak thus is a measure for the quality of graphene. A negligible intensity of the D peak indicates high-quality graphene. The Graphene Supermarket²⁵ considers a D vs. G ratio below 0.3 an indication of appropriate quality. Figure 3.6 shows that the ratio between the G and 2D peaks is different for graphene and graphite. It is found that the ratio G/2D increases with the number of layers. The intensity of the G peak increases almost linearly with the number of layers. For less than five layers the 2D peak is found to be more intense than the G peak.²⁶ Apart from this trend, a numerical relation to exactly determine the number of layers from this ratio is not found, so it is not possible to judge quantitatively on the number of layers based on this observation.

A closer look at the 2D band reveals the possibility to obtain more information on the thickness and even the stacking order of the layers. Several articles show a dependence of the shape of this peak on the number of layers.^{21,22,26} For more than one layer the 2D peak consist of more than one component as can be seen in the spectrum for graphite. The general trend is a single peak for monolayer graphene with a shoulder developing on the higher relative wave number side of the peak, which increases with the number of layers and eventually becomes the main peak. Both Ferrari *et al.* and Nguyen *et al.* found a dependence of the 2D peak position on the excitation energy. This is due to this peak being related to a double resonance process, which links the phonon wave vectors to the electronic structure.²² This scattering process involves phonons in the ΓK direction.²¹ In graphite and multilayer graphene two stacking orders, ABA or Bernal stacking and ABC or rhombohedral stacking,²⁷ exist. Nguyen *et al.* recently showed a clear dependence of the 2D peak and other peaks on the stacking order of multilayer graphene. The shoulder of the 2D peak develops quicker for ABA stacking compared to ABC stacking. These results are shown in Figure 3.7. Nguyen *et al.* established criteria for unambiguous determination of the thickness and stacking order of multilayer graphene in which they used several features in the Raman spectrum of graphene and different excitation energies. Besides the already mentioned 2D peak also the G* band ($2400\text{--}2450\text{ cm}^{-1}$), the M band ($1700\text{--}1800\text{ cm}^{-1}$), the N band ($\sim 1500\text{ cm}^{-1}$) and some weak mode in the range $1780\text{--}2250\text{ cm}^{-1}$ are used. For example, measurements with two different excitation energies of the 2D band allows for determination of both the number of layers and the stacking order in the case of more than two layers. With increasing excitation energy the peak blueshifts and the shape is dependent on excitation energy, number of layers and the stacking order as can be seen in Figure 3.7. Other combinations of measurements for different features and excitation energies can be used to obtain and verify this information.

It should be noted that theoretically a monolayer of graphene on nickel does not show a Raman spectrum.²⁸ However, a Raman signal of monolayer graphene on nickel has been reported. This can be the result of decoupling of graphene and nickel or graphene actually being multilayered.

3.2.3 Scanning electron microscopy

In a scanning electron microscope (SEM) electrons are thermally emitted from a filament to form a collimated beam of electrons that is focused on a sample. This results in different events inside the sample, which can be used to image and characterise the sample. The wavelength of

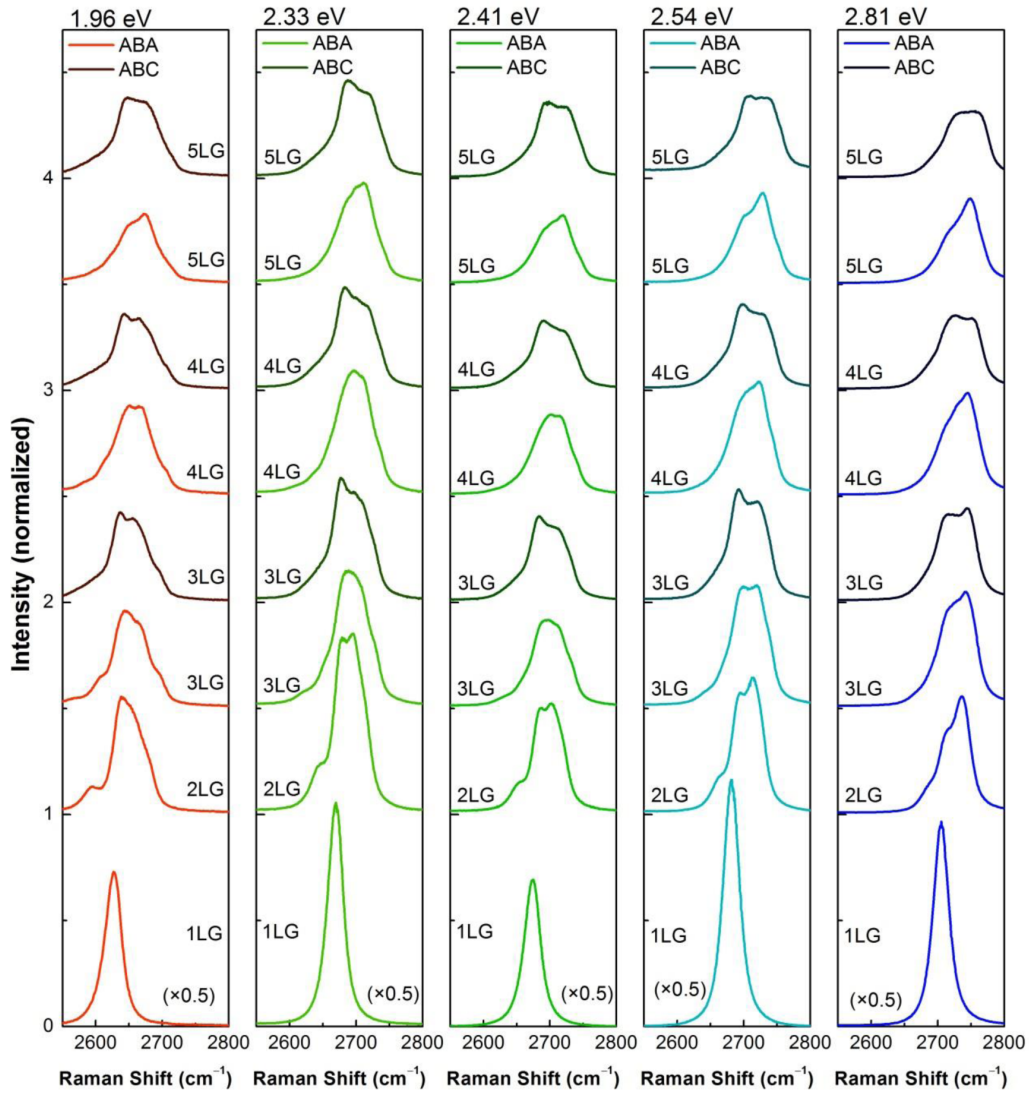


Figure 3.7 – 2D band of graphene with both ABA and ABC stacking under 5 different excitation energies. Intensity is normalised to the intensity of the G peak. The used excitation energies correspond to 632.8, 532, 514.5, 488 and 441.6 nm respectively. Source: Nguyen et al.²¹

electrons is shorter than that for photons, so the resolution is larger for a SEM than it is for an optical microscope. Among the signals used are secondary electrons, elastically backscattered electrons and X-rays. The most widely used method in SEM employs the secondary electrons. These are electrons that are liberated from a sample in a cascade process. Impinging electrons result in a sort of avalanche of secondary electrons. These electrons have a low energy and therefore only electrons originating in the first few nanometers can escape the sample and reach the detector. The orientation of the sample with respect to the incoming beam affects the number of secondary electrons. Perpendicular impingement gives the lowest yield, while sloping surfaces produce a larger number of secondary electrons. With this information an image of a sample can be created.

In the MESA+ Nanolab a Nova 600 dual FIB (focused ion beam) system is available, which is shown in Figure 3.8. In addition to imaging by means of electrons, the system is able to mill the sample by using an ion beam. This offers the possibility to obtain a depth profile by making several images and etching away material in between the images. In this work the focused ion

beam is not used. Operator assistance is needed, due to the complexity of the system. This is done by Johnny Sanderink.

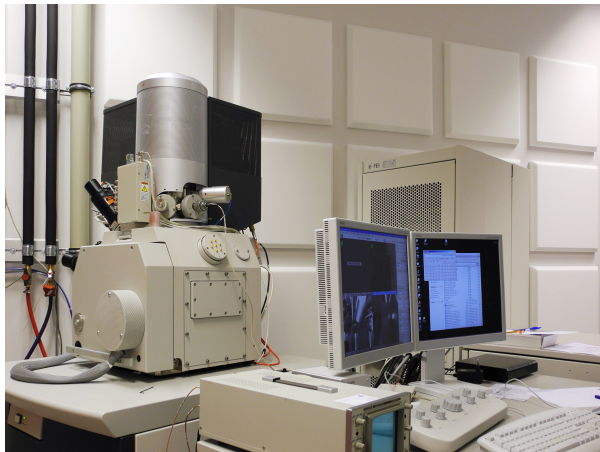


Figure 3.8 – Nova 600 dual FIB in the Nanolab. Photo by the MESA+ cleanroom staff.

3.2.4 Vibrating sample magnetometry

A vibrating sample magnetometer (VSM) is an instrument capable of measuring the magnetisation of a sample. By varying the externally applied uniform magnetic field the magnetisation vs. magnetic field curve can be obtained. In a VSM a sample is attached to a sample holder, which is made to vibrate. The vibrating sample induces a changing inductance through a pick-up coil, which translates to a voltage across the coil. The voltage is proportional to the magnetic moment of the sample, but does not depend on the applied magnetic field, because this is static. Usually, a lock-in amplifier is used to measure the voltage. The actuator signal of the sample holder is used as reference.

3.2.5 X-ray diffraction

X-ray diffraction (XRD) is a technique that employs X-rays to obtain a diffraction pattern, which gives structural information on a sample. A sample is illuminated with monochromatic light of known wavelength and interference occurs between rays that are reflected by different crystal planes in the sample, which results in maxima and minima in a plot of intensity versus incident angle. This effect is called Bragg reflection and according to Bragg's law constructive interference occurs for $m\lambda = 2d\sin\theta$, where m is an integer corresponding to the diffraction order, λ is the wavelength of the incident light, d is the spacing between crystal planes and θ is the diffraction angle. From this relation it is clear that smaller wavelengths offer a better resolution. The wavelength of X-rays is on the order of the atomic spacing, so information on the crystal structure can be obtained.

Different angles are involved in XRD measurements. The most important angles are the angle of incidence (ω) and the detector rotation (2θ). These angles are indicated in Figure 3.9. For a sample with grains parallel to the sample surface, the angle of incidence and the detection angle for these grains is equal if $\omega = \theta$. For grains that are not parallel to the surface an offset Δ has to be introduced to fulfil this condition: $\omega = \frac{1}{2}(2\theta) + \Delta$. In the most common measurements source and detector are moved in a coupled manner to keep this condition fulfilled. This type of measurement is referred to as a coupled scan. In the meanwhile the intensity is measured to determine the Bragg diffraction angle for which diffraction peaks occur. The diffraction angles

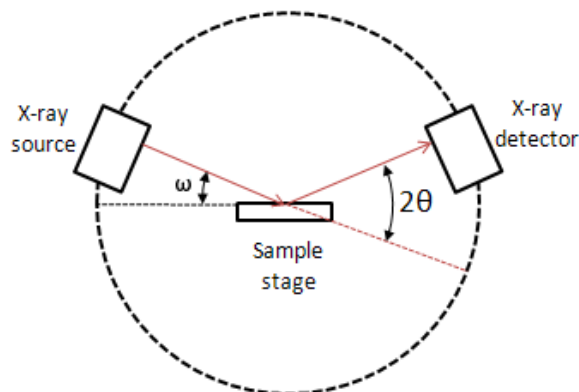


Figure 3.9 – Angles in XRD measurements. The angle of incidence is indicated by ω and 2θ is called the detector rotation, which is the angle between incident beam and the line from sample to detector. Adapted from chemwiki.ucdavis.edu.

are directly related to the crystal orientation and the peak width yields information on the size of individual crystallites (L). For this purpose Scherrer's equation²⁹ can be used:

$$L = \frac{K\lambda}{FWHM \cdot \cos(\theta)} \quad (3.1)$$

Here λ is the wavelength of the incident X-rays, $FWHM$ is the full-width at half maximum of the peak, θ is the Bragg angle and K is a numerical constant taking into account the definition of the peak width and crystallite size, the shape of the crystals and the size distribution. K ranges from 0.62 and 2.08. If the FWHM is used for spherical crystals 0.94 is a commonly used value.

So-called rocking curves are obtained by varying ω , while the angle between source and detector (2θ) is fixed. This can be achieved by tilting (rocking) the sample with fixed position for source and detector. This yields information on the relative orientation of crystallites with the same crystal orientation, which can be slightly tilted with respect to each other.

3.2.6 X-ray photoelectron spectroscopy

In X-ray photoelectron spectroscopy (XPS) photons with wavelengths in the X-ray range (0.01-10 nm) are used to liberate electrons from a material. These electrons are called photoelectrons, because light is used to liberate them. The kinetic energy and the number of electrons is measured. The measured kinetic energy is directly related to the binding energy of the electrons in the sample: $E_{binding} = E_{photon} - E_{kin} - \phi$. Here ϕ is the work function of the detector, which takes into account the energy loss upon absorption by the detector. The kinetic energy is the difference between the total photon energy and the energy needed to liberate and detect an electron, which is given by the sum of the binding energy and the work function. A plot of intensity versus binding energy yields direct information on the elements present in the sample and thus can be used to characterize the sample surface. Only electrons originating close to surface are able to leave the sample, so XPS is a surface sensitive technique.

3.3 Transport measurements

The experiments discussed in the previous section all mainly serve to investigate parts of the fabricated device and to improve the design and fabrication process. The experiments of par-

ticular interest in this work are transport measurements in which at least current and voltage play a role, but also other parameters can be varied and/or measured. The different types of transport measurements will be explained below.

Generally, in a measurement one independent variable (swept quantity), one dependent variable (measured quantity) and one or more bias parameters are involved. Bias parameters are kept constant during a single measurement, but can be adjusted in subsequent measurements. Usually either current or voltage is the dependent variable. Examples of other quantities involved, either as bias parameters or as independent variables, can be temperature and magnetic field.

Most transport measurements are done in the four-terminal configuration, which is schematically shown in Figure 3.10. In this configuration two wires are used to source a current to the device, while the other two wires are used to measure the voltage. In all measurements a current is sourced, but a set point can be chosen for either the current or the resulting voltage as the independent quantity, while the other one is measured as the dependent quantity. This method offers the possibility for more accurate measurements and eliminates resistances from contacts and connection wires from the measured values.

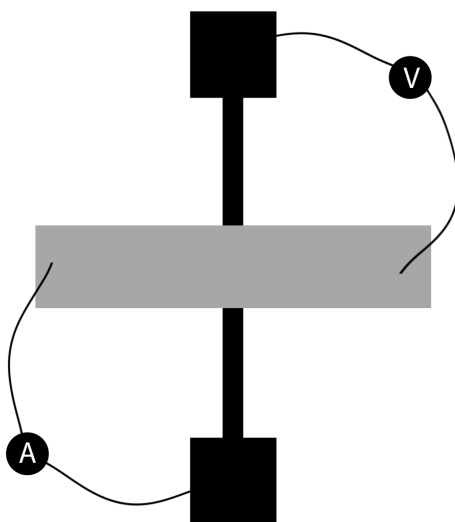


Figure 3.10 – Four terminal configuration (schematic) for the device used in this project. Two contacts are connected to a voltage source (meter) and two other contacts are connected to a current meter (source).

Different measurement setups are used for transport measurement. The used systems are called Bruker, Oxford, Heliox and Triton and all of them can be used for measurements at reduced temperatures and in the presence of an externally applied magnetic field. The ranges for temperature and magnetic field are different for the different systems. Pictures of the used set-ups are shown in Figure 3.11.

Different electronics are used for measurements, namely a Keithley multimeter 2000, Keithley sourcemeters 2400 and 2401, Keithley Nanovoltmeter 2182A and Keithley current source 6221. Furthermore, several different modules of the available Delft electronics⁵ (i.a. source modules, measurement modules and adapters) are used.

⁵ <http://qtnwork.tudelft.nl/~schouten/index-list.htm>

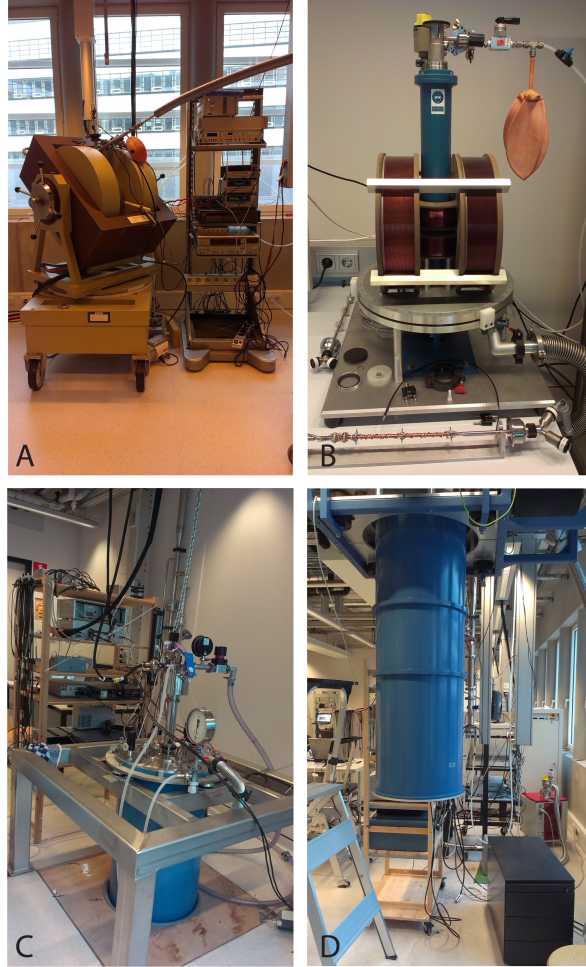


Figure 3.11 – Measurement setups. A) Bruker, B) Oxford, C) Heliox and D) Triton

3.3.1 Current-voltage (IV) measurements

One type of transport measurement is a current-voltage (IV) measurement in which a voltage is applied across a junction, while the resulting current is measured. This can be done in both a two- and four- terminal configuration. The graphs obtained in these measurements are called IV or conductance curves and yield information on the transport properties and mechanisms involved. The derivative of an IV curve with respect to V ($\frac{dI}{dV}$) is called the (differential) conductance, which is the inverse of the (differential) resistance. For an Ohmic device the IV curve is linear and thus $\frac{dI}{dV}$ is constant.

To obtain more information on the type of transport and the possible presence of defects IV measurements can be done at different temperatures. Due to the temperature dependence of the Fermi-Dirac distribution there is a weak decrease in resistance with increasing temperature. In addition to this dependence, different transport mechanisms and defects depend differently on temperature, which makes it possible to identify the type of mechanism and/or defects involved.

The type of measurements proposed by Tedrow and Meservey as discussed in section 2.5 also are IV measurements. Tedrow-Meservey measurements are performed in the presence of a bias magnetic field, which is not changed in between measurements, since it only serves to split the energy levels.

3.3.2 Magnetoresistance

In the previous chapter magnetoresistance was discussed. Although the different effects (GMR, TMR etc.) usually have a very different origin these effects have in common that (as the name suggests) they are measurable in the presence of an external magnetic field. In magnetoresistance measurements the external magnetic field is applied along a certain axis, which has to be chosen with care, and the magnitude of the field is swept. A bias of either voltage or current is applied and the other quantity (voltage or current) is measured. If current is measured and a constant bias voltage is applied the measurement is referred to as IB measurement. On the other hand, a VB measurement refers to measuring voltage in the presence of a constant bias current. Depending on the type of magnetoresistance effect, the measured curves can be used to characterise a device and test theories and hypotheses.

3.4 Data analysis

The data obtained in the different experiments has to be analysed and interpreted. In order to do so the raw data should be processed. For most measurements straightforward methods are used, which are assumed to be obvious and therefore omitted here. A more sophisticated method is used for the analysis of Raman measurements. This method is called cluster analysis and is explained below.

3.4.1 Cluster analysis

Cluster analysis is a common technique for statistical data analysis and refers to the general task of grouping similar data to make it easier to interpret. All objects in a data set can be represented by a point in a n -dimensional coordinate system where each of the n coordinates corresponds to a particular property. These properties in principle can be anything and depend on the specific data. People, for example, can be represented by a point in a two-dimensional coordinate system with on one axis their length and on a second axis their weight. Of course other properties (age, shoe size etc.) can be used as well. In this example the values assigned to the properties is obvious, but the properties can be more abstract (e.g. someone's looks) and consequently assigning corresponding values is more difficult. It can be impossible to assign objective values.

Different algorithms are used to divide objects in groups (clusters), which all have in common the goal to obtain clusters of objects that have more similarities with objects in the same cluster than with objects in other clusters. A correct algorithm can not be determined objectively and an appropriate algorithm should be chosen experimentally, but not all algorithms can be used for all data sets. Some examples of used grouping methods are centroid-based, density-based and connectivity based clustering. Centroid-based clustering uses a single vector/point in the coordinate system to represent each cluster. Objects are then assigned to the nearest cluster. In most cases the number of clusters has to be fixed in advance. In density-based models clusters are formed by regions in the coordinates system with a higher object density, while cluster boundary have a lower density. Connectivity based (also called hierarchical) models depend on the distances between data objects. Several methods to calculate these distances are used. Two different strategies exist in hierarchical clustering: a agglomerative and divisive approach. The former starts with all elements separated and aggregates the most similar (groups of) elements until the desired number of clusters is reached. The later start with all elements grouped together and divides this groups into smaller groups of elements that have the most similarities until the desired number of clusters is reached.

The resulting clustering is the set of all clusters and their properties and also specifies the mutual relationships. A clustering can be hard or soft. In the first case each object either does or does not belong to a cluster, while in the second case objects are member of each cluster to a certain degree. It is possible to allow for so-called outliers, which are objects that are not a member of any cluster, because they differ too much from other objects. This serves for example to prevent unwanted linking of clusters.

In this project a hierarchical form of cluster analysis resulting in a hard clustering of the Raman data is used. It is implemented in a Matlab executable made in the group of Cees Otto. Several options for data treatment are available in this program, but these are not discussed here, because they are not used and the details are too sophisticated.

Chapter 4

Design and fabrication

Several devices were used in this project, which differ in the details, but all are variations on the same design. This design was already made before the start of this master assignment. During this assignment minor changes to the original design are made based on experimental results. The evolution of the used device design will be explained. In the first part of this chapter the design is described and the second part is devoted to the fabrication process. The details of the designs used for the different experiments are stated in a next chapter.

4.1 Design

Figure 4.1 gives an impression of the device design used in this master project. This design was made by Elmer van Geijn. A sample is 11 mm by 11 mm. A device consists of a crossbar structure in which the junction area is formed by a contact hole in an insulating layer that separates the bottom electrode from the perpendicular top electrode. The bottom electrodes are formed by a nickel layer covered by a few monolayers of graphene. A layer of resist serves as the insulating layer between bottom and top electrodes and square contact holes are defined in this layer. The top electrode consist of a few (at least two) layers. The materials used for the top electrodes depend on the type of experiment. Originally, a device contained ten bottom electrodes and three top electrodes, which resulted in 30 junctions per device. For later devices only one top electrode is deposited to prevent possible parallel conduction paths. This reduces the number of junction on a single sample to ten.

It should be noted that the used design does not reflect the ideal situation as was considered by Karpan *et al.* and it is worthwhile to discuss the differences. First, the theoretical treatment assumes the nickel surface to be perfectly crystalline and the interface to be free of disorder. Both conditions will not be fully met in practice. Theoretically interface roughness reduces the magnetoresistance effect from 100% to about 70% for a roughness of 50%. Interface disorder of a single layer of random alloy reduces the magnetoresistance to 90%. Second, perfect alignment between graphene and nickel was assumed, which means that the lattices are not rotated, tilted or shifted with respect to each other. Graphene growth starts on a nickel(111) grain on which it is aligned, but the combination of optical and AFM images show graphene to grow over grain edges. Alignment is not expected for neighbouring grains. The theoretical effect of this deviation from the ideal situation was not investigated. Thirdly, perfect lattice matching was used in the theoretical treatment. The mismatch is small, only 1.3% for graphene on a nickel (111) surface, but not absent, so even for well-aligned graphene the real situation is less ideal. However, Karpan *et al.* showed the influence of lattice mismatch to be small (5% mismatch would decrease the magnetoresistance to 90%). Fourthly, theoretically the graphene is assumed to be a perfect layer of known thickness, but in reality a patched layer is used and the patches

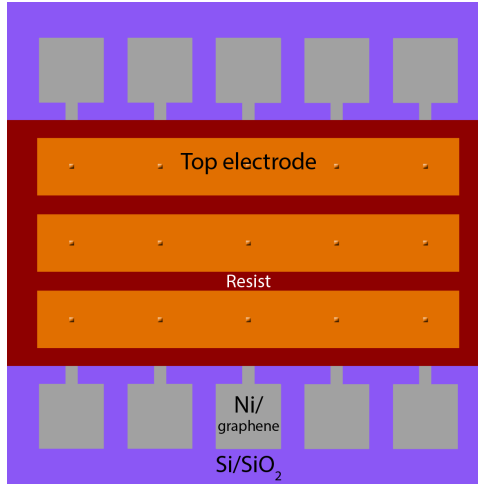


Figure 4.1 – Impression of the device design used in this project. In this image a devices consists of five bottom electrodes (grey) and three perpendicular top electrodes (orange) separated by a insulating layer of resist (red). In reality ten bottom electrodes and one or three top electrodes.

can be of different thickness. As a result, the thickness of the graphene below the contact holes is not well-defined for randomly placed contact holes. In addition, the thickness of the used graphene layer is between one and seven monolayers, but to suppress tunnelling a layer of at least three monolayers is preferable. This will probably not be the case for all randomly placed junctions. The differences in thickness on the one hand is a disadvantage, but it also offers an opportunity to investigate the predicted thickness dependence. This is one of the reason to choose for EBL instead of photolithography to define contact holes. Finally, it should be noted that the interaction between graphene and nickel destroys the electronic structure of graphene, which is one of the ingredients of the predicted spin filtering. This does not occur in a geometry with a ferromagnetic electrode on both sides of the graphene layer, but in the used device design only one ferromagnetic electrode is used.

4.2 Fabrication

The workflow for the final fabrication process is depicted in B.2 and the corresponding fabrication recipe is described step by step in B.1. This process is roughly described here and important parts are explained in more detail in the remainder of this section. The used techniques are discussed in chapter 3.

The fabrication starts with a Si/SiO₂ substrate covered with a nickel layer and 1–7 monolayers of graphene. The graphene was deposited prior to purchase by chemical vapour deposition,³⁰ which resulted in patches of graphene with different thickness and a size of approximately 3 to 10 microns.²⁵ The wafer is diced in smaller chips, cleaned in acetone to remove the protective photoresist layer and a layer of positive photoresist (OiR 907/17) is spin coated. The samples are put on a hotplate, exposed through a mask as shown in Figure 4.2 in the EVG620 Bond Aligner, put on a hotplate again and subsequently developed in OPD-4262 (a solution of tetramethylammonium hydroxide (TMAH) in water) to define the bottom electrodes in the photoresist layer. Different widths of the bottom electrodes are available on the photolithography mask: 4, 6, 8, 10, 15, 20, 40 and 60 μm . The bottom electrodes should not be too narrow to prevent the contact hole from not being completely on top of the bottom electrode in case of randomly placed contact holes. This is not an issue for contact holes defined by EBL, but wider bottom electrodes leave a larger area on which junctions can be placed, so bottom electrodes with a

width of 60 μm are used.

Ion-beam etching is used to etch away the graphene and nickel that is not protected by the photoresist leaving only the narrow strips with contact pads as bottom electrodes on the substrate. Etching is done in the Oxford Ionfab[®]300Plus with standard settings. The photoresist layer is removed by cleaning the samples in acetone and, if necessary, by short oxygen plasma treatment.

Originally, the contact holes were defined by means of photolithography. For these samples a new layer of photoresist (diluted OiR 906/12) is spin coated. The samples are put on a hotplate, exposed through a mask as shown in Figure 4.2 in the EVG620 Bond Aligner, put on a hotplate again and subsequently developed in OPD-4262 to define the contact holes in the photoresist layer and remove the photoresist on the contact pads. For reasons explained later, the contact holes are defined by means of EBL for later samples. In this case a layer of EBL resist is spin coated, while using Scotch tape to keep the contact pads free from resist. Poly(methyl methacrylate) (PMMA) A4 is used as EBL resist. Here A4 refers to the dilution. The Scotch tape is removed, the contact holes are written in the RAITH150-TWO and the resist is developed in a 1:3 mixture of methyl isobutyl ketone (MIBK) and IPA to define the contact holes. More details on the contact holes are given below.

Top electrodes are deposited through a shadow mask as shown in Figure 4.2 using electron beam evaporation in the DCA Instruments M600 and consist of a few layers. This will be discussed in more detail below.

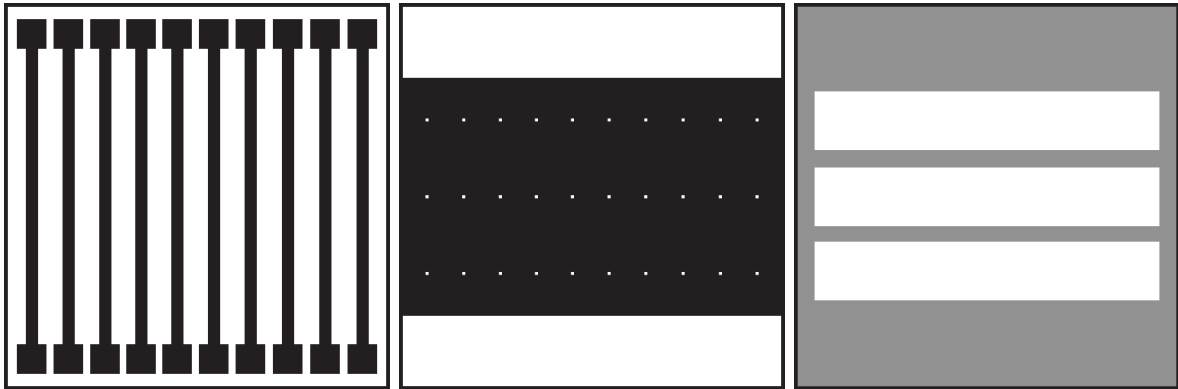


Figure 4.2 – Masks used for first (left) and second (middle) photolithography step and the shadow mask for electron beam evaporation (right). In photolithography the black parts are not exposed and in electron beam evaporation the white strips are open. The Clewin layout of the photolithography mask is depicted in section B.3. For later devices the mask in the middle is not used to define the contact holes, but (maskless) EBL is used instead. For later devices only one top electrode is deposited by covering the two outer strips of the mask with tape.

4.2.1 Contact holes

Defining the contact hole requires special attention for different reasons. The first reason is the roughness of the nickel-graphene layer used for the bottom electrodes. As will be shown later, the height difference between peaks and valleys in the nickel layer is quite large. Moreover, to ensure good electrical conductance the top electrode should be continuous at the edge of a contact hole.

A good conductance requires good step coverage of the contact hole edge, which therefore should not be too steep. Not too steep walls can, in the case of photolithography, be accomplished by a thinner layer of resist and suitable parameters for exposure and development. To obtain a

thinner layer than achievable with standard photoresist a diluted photoresist is used. OiR 906/12 photoresist is diluted by mixing 70 vol.% OiR 906/12, 18 vol.% methyl-3-methoxypropionate (MPP) and 12 vol.% ethyl-3-ethoxypropionate (EEP) and leaving it in an ultrasonic bath for half an hour to improve mixing. On the photolithography mask square holes of 2, 3, 4, 6, 8 and 10 μm are available. Optical microscopy and AFM are used to determine the best combination of exposure and development times. Most of this work was already done before the start of this assignment. Images of the obtained photoresist layers and contact holes are shown in chapter 5. Samples are exposed for 5 seconds and developed for 20 seconds to define the contact holes.

In order to have a well-defined junction and a continuous superconducting layer the contact hole should not extend over many grains. This means that the contact holes should be small. For this reason contact holes are made by means of EBL for later devices, because smaller dimensions are achievable with this technique. Furthermore, the location of the contact holes can be chosen instead of them being randomly placed. Due to the smaller dimensions the walls probably are steeper, which can cause problems with the continuity of the top electrode. To enhance the change of attaining a continuous top electrode a thin layer of EBL resist is used as insulating layer in the first place. PMMA A2 is spin coated at a high spin speed, but this resulted in a layer that was not insulating. For that reason there currently is no other choice than using a thicker PMMA layer with the risk of a non-continuous top electrode.

4.2.2 Top electrodes

The top electrodes consist of two or three layers and the used materials differ for different experiments. Deposition is done by means of electron beam evaporation. For most devices first a layer of aluminium oxide (Al_2O_3) is deposited, which serves as a tunnel barrier to electrically decouple the bottom electrode from the top electrode. The thickness of this layer is a few nm. Deposited aluminium oxide is known to be under-stoichiometric (AlO_x with $x < 1.5$),³¹ so after deposition of these layers the samples are left in the load lock under atmospheric pressure to let the aluminium oxide naturally oxidise further. This improves the quality of the tunnel barrier.

For the first experiments to investigate the quality of the tunnel barrier permalloy (a nickel-iron alloy with approximately 80% nickel) is deposited as second layer of the top electrode. For the measurements of spin polarisation based on the theory of Tedrow and Meservey a superconducting layer with a high critical field is needed. Therefore a layer of aluminium is deposited as second layer for these experiments. Not all samples contain a tunnel barrier. For the samples without a tunnel barrier the layer of permalloy or aluminium is the first layer of the top electrode.

To obtain good electrical contact a capping layer is deposited, which improves the coverage of the step edge of the contact hole. The properties of this layer are not very critical. Aluminium, platinum or copper is used for this top layer. Aluminium obviously can not be used as capping layer if a thin layer already is deposited to use its superconducting properties.

The results in the next chapter are accompanied by the actual materials used in the top electrode.

Chapter 5

Results and discussion

In this chapter the conducted experiments and their results will be discussed. First the experiments and measurements to characterise the used substrate and optimise the used design and fabrication process will be treated. This will be followed by transport measurements towards experiments meant to test the theoretical prediction of Karpan *et al.* by means of the measurement technique proposed by Tedrow and Meservey.

5.1 Sample characterisation

In this project two different wafers of the same supplier are used. Extensive characterisation of these substrates is important in order to alter the design and fabrication process accordingly. The results of the characterisation of the nickel and graphene layer and the consequences are presented in this section.

5.1.1 Nickel

The nickel layer on the purchased substrates is deposited by electron beam deposition, but the exact process parameters and the properties of the layer are not known to us. To characterise the nickel layers for both wafers different measurements are done of which the results are discussed here. The chemical structure is examined with XPS. The results of these measurements are shown in Figure 5.1. The observed Ni 2p spectrum is characteristic for metallic nickel, as desired for the spin filter experiments, and shows no oxide-related features. The O 1s signal is attributed to surface contamination. XPS is a very surface sensitive technique, so even a small amount of surface contamination results in a strong signal. The difference between the measurements before and after annealing for wafer 1 are probably caused by desorption of surface contamination. Some measurements show a peak corresponding to silicon (not shown here). This probably originates from the edge of the sample. A depth profile by sputtering the surface of wafer 1 during XPS measurements (done by Gerard Kip) shows expected results. The top layer consists of carbon, but the atomic concentration of carbon quickly drops, while the nickel concentration rises. The bottom layer is silicon. The nickel layer does not contain a significant amount of other elements, such as carbon and silicon.

The magnetic behaviour is investigated by means of VSM. Samples of 5 mm by 5 mm are mounted in the machine. The magnetisation curves are shown in Figure 5.2. The magnetisation curve for a 284 nm film measured at 300 K by Song *et al.*³² qualitatively is very similar. They obtained a saturation magnetisation density of $4.0 \cdot 10^5$ A/m.⁶ The measured coercivity is in the

⁶ $1 \text{ emu/cm}^3 = 10^3 \text{ A/m}$, <https://www.qdusa.com/sitedocs/UnitsChart.pdf>

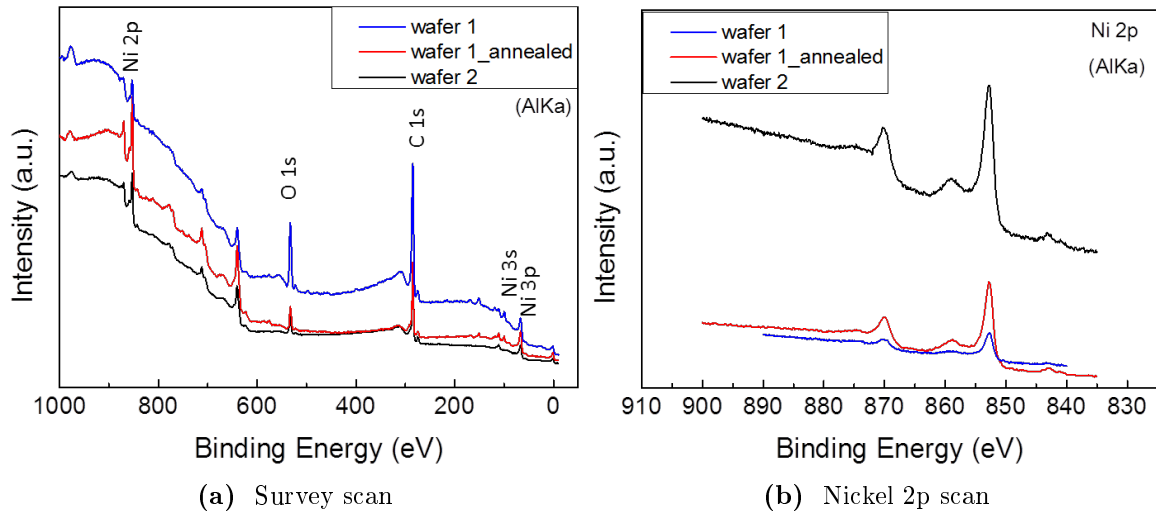


Figure 5.1 – XPS measurement for graphene on nickel. The left image shows a measurement for a large binding energy range. Peaks corresponding to nickel, oxygen and carbon are visible. The left image shows a detailed scan of the binding energy interval corresponding to the nickel 2p orbital. For wafer 1 measurements are done before and after in-situ annealing, which reduces the background signal. Measurements are done by Johnny Wong, Michel de Jong and Derya Ataç. Images are made by Derya Ataç.

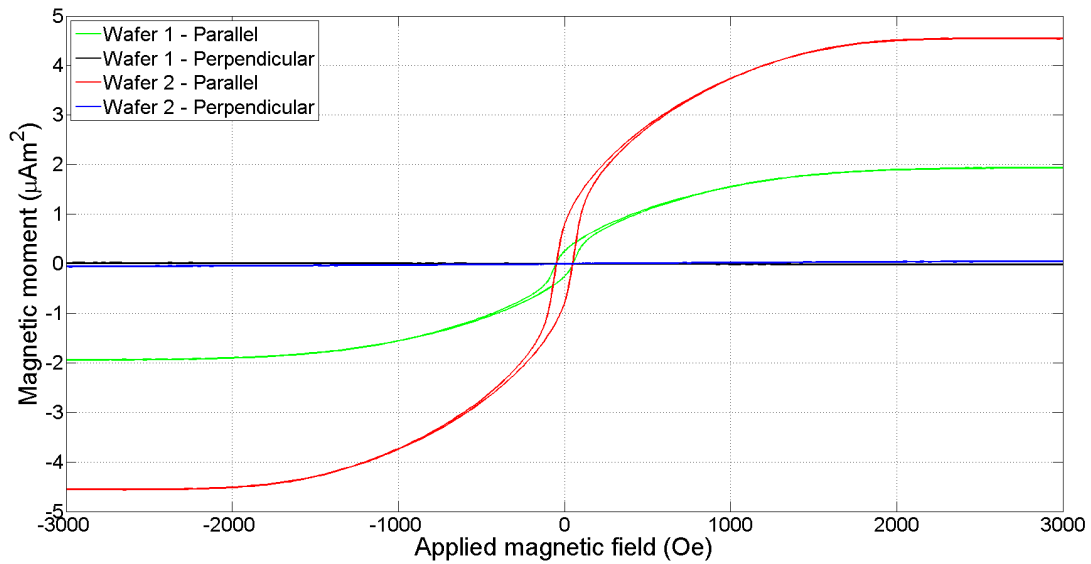


Figure 5.2 – Magnetisation curves for 5 mm by 5 mm samples of Si/SiO₂|Ni|Graphene. In the case of wafer 1 the sample is exposed to an ion beam for a few minutes to etch the graphene layer, but similar measurements for a sample with graphene do not yield significantly different results. Magnetisation perpendicular to the applied magnetic field is negligible. The saturation magnetisation parallel to the applied magnetic field is 1.95 μAm^2 and 4.56 μAm^2 respectively. The coercive field is approximately 50 Oe in both cases. Measurements are done by Elmer van Geijn.

range obtained by M.S. Miller *et al.* for rf sputtered nickel.³³ In order to calculate the saturation magnetisation density an estimate for the thickness of the nickel film is necessary. According to the supplier the thickness of the nickel on wafer 1 is 300 nm. However, SEM images show the thickness to vary quite a lot and an approximation for the thickness of about 225 nm seems more accurate. Using this value results in an estimate for the saturation magnetisation density of $3.5 \cdot 10^5$ A/m. A piece of peeled nickel on wafer 2 allowed for easy AFM measurement to determine the thickness to be approximately 500 nm for this substrate, which yields $3.6 \cdot 10^5$ A/m as an estimate for the saturation magnetisation density. Calculated values for the saturation magnetisation density based on experimental results and an estimate of the number of atoms are $4.9 \cdot 10^5$ A/m³⁴ and $5.2 \cdot 10^5$ A/m respectively. Differences between the results presented here and the measured and calculated values for the saturation magnetisation density probably are caused by errors in the dimensions, especially the thickness, of the measured sample and small misalignment of the samples in the VSM.

XRD measurements are done to characterise the structure of the nickel layers for both wafers. Figure 5.3 shows coupled scans for both wafers. Both measurements show peaks corresponding

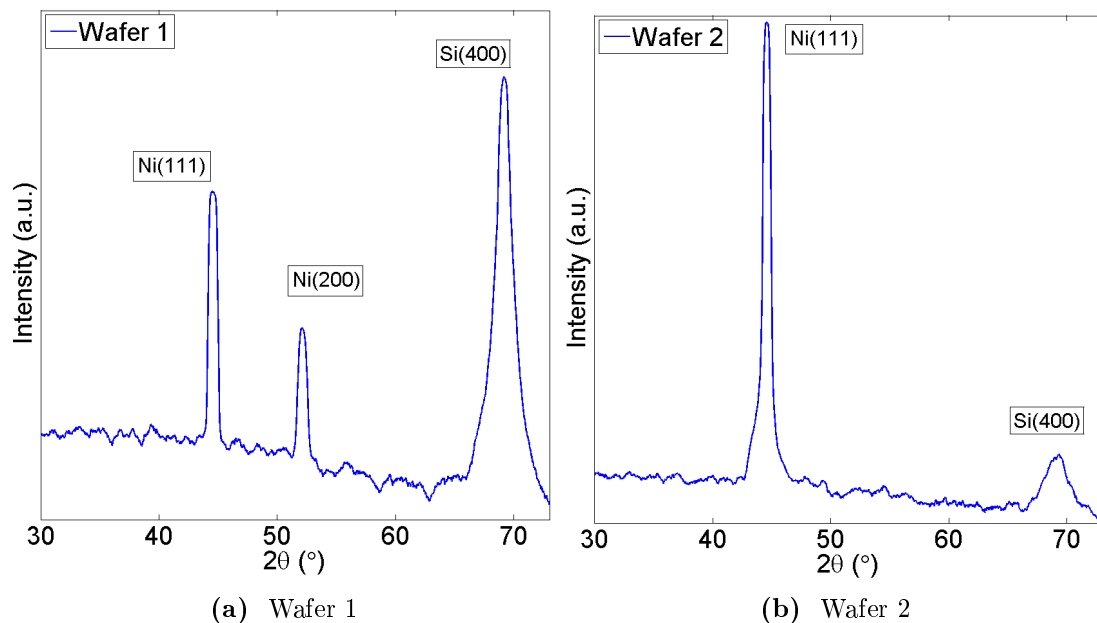


Figure 5.3 – Coupled XRD measurements (intensity vs. 2θ) for nickel on Si/SiO₂. Peaks corresponding to Ni(111) and Ni(200) are clearly visible. Also a substrate peak is visible. Measurements are done together with/by Elmer van Geijn.

to the Ni(111) plane and Si(400). The last peak originates from the substrate and is probably smaller for wafer 2 due to the thicker nickel layer on this wafer. For wafer 1 also a peak corresponding to the Ni(200) plane is visible. Scherrer's equation (Equation 3.1) is used to calculate the average crystallite size from the peak width. This amounts to 30–100 nm depending on the shape factor used. Rocking curves for both the (111) and (200) plane do not show very pronounced peaks for wafer 1, which means that the individual grains for almost the same out-of-plane orientation are slightly rotated and tilted relative to the sample surface. The presence of peaks for both the (111) and (200) plane and the absence of peaks in the rocking curves indicates a random crystal orientation, which is confirmed by comparison with the powder spectrum for nickel (see Figure 5.4(a)). Wafer 2 has a single crystal orientation, the (111) orientation. A corresponding rocking curve is shown in Figure 5.4(b). A clear peak is visible in the rocking curve, which indicates in plane alignment of the individual grains in the nickel film on wafer 2.

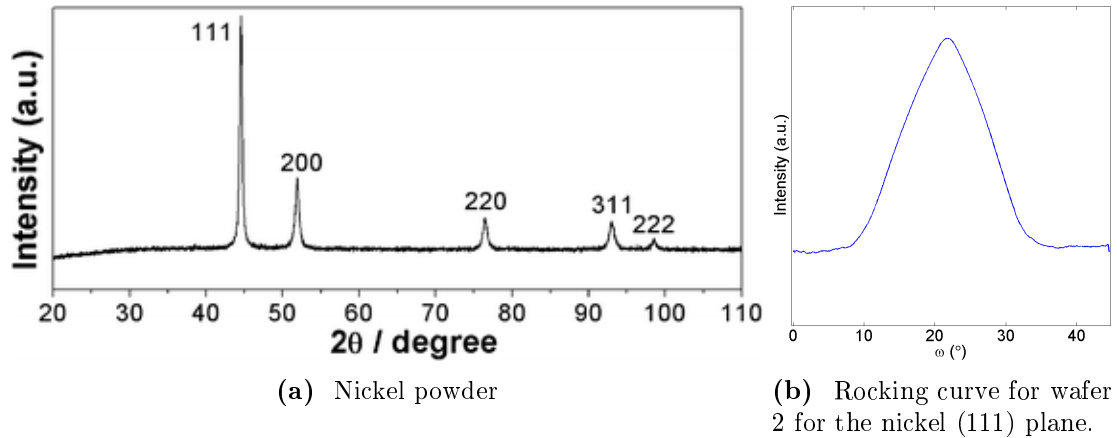


Figure 5.4 – Figure 5.4(a) XRD spectrum for nickel powder. Source: Wang et al.³⁵ Figure 5.4(b) Rocking curve (intensity vs. ω) for $2\theta = 44.54^\circ$. Measurement is done by Elmer van Geijn.

Figure 5.5 shows AFM images of the nickel surface. Both wafers are rough and show quite large differences in height, but wafer 2 is smoother than wafer 1 and shows larger grains.

The different experiments show the nickel films to be metallic and the surfaces are quite rough. The magnetic behaviour is as what would be expected for nickel. In the case of wafer 1 the nickel film is polycrystalline. A possible explanation for the roughness is the high temperature in the CVD process of graphene growth. This also is a possible reason for the random orientation of the crystallites in wafer 1. However, the exact details of the growth of the nickel and graphene are not known to us, so other explanations are also possible. On the one hand large nickel grains are more preferable, since this increases the chance for a contact hole to cover a single nickel grain. On these substrates a contact hole defined by photolithography of a few micrometers will probably cover more than one grain. On the other hand the probable recrystallisation that results in larger grains also causes the roughness, which can give problems in electrically separating the bottom electrode from the top electrode by means of an insulating resist layer. This will be discussed in more detail later. Based on these results it is decided to use EBL instead of photolithography to define the contact holes. With EBL features down to the nanometer scale can be defined and it is possible to choose their location based on for example images made with an optical microscope. This solves the problem of covering more than one grain, but for wafer 1 the orientation of the targeted grain still is random. This problem can not be solved for this wafer, but for wafer 2 it does not exist.

5.1.2 Graphene

Images made with an optical microscope reveal a patch work at the surfaces of the purchased samples as can be seen in Figure 5.6. It is tempting to think of these patches as graphene with their colour as an indication of their thickness. In what follows it will be shown that this is indeed the case.

Raman spectroscopy is employed to characterise the graphene layers on the nickel substrates. The fabrication process for this project is adjusted based on the knowledge presented in subsection 3.2.2 and the measurements done on the purchased samples. Not all available information in the Raman spectra is used in this project, but it probably will be valuable for the NanoElectronics group in the future.

Raman spectra obtained in measurements done in the MCBP group clearly show the characteristic main peaks for graphene, the G and 2D peaks. In Figure 5.7 two spectra are shown.

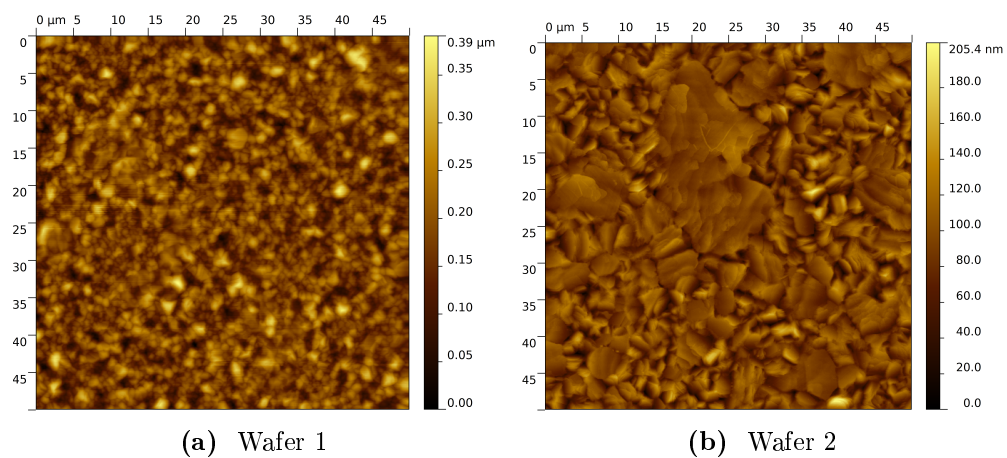


Figure 5.5 – AFM images of nickel surfaces covered with graphene. The surfaces are very rough, so the very thin graphene flakes are not visible.

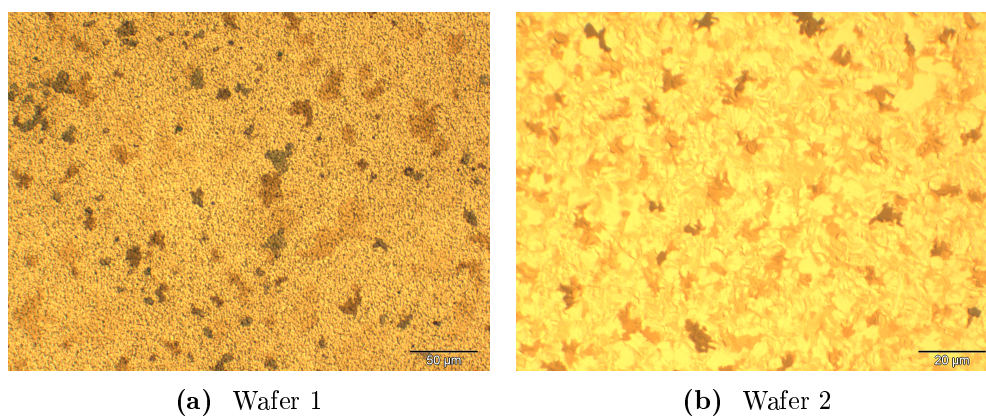


Figure 5.6 – Optical microscope images of nickel surfaces covered with graphene. Both images show patches of different darkness on the surface. The coverage of wafer 2 is better than the coverage of wafer 1.

Besides the main peaks several other peaks are visible. Some peaks are slightly shifted with respect to the expected value for the Raman shift. This can be caused by interactions between graphene and nickel that affect the vibrational modes. Furthermore, peak positions can depend on for example the number of layers. The increasing background with increasing Raman shift is due to the Raman response of nickel.

Measurements in the set up of HybriScan Technologies[®] offer the possibility to investigate the correspondence between optical images, scanning electron images and Raman measurements. Figure 5.8 shows results of these experiments and a clear correspondence between the images made with an optical microscope and a scanning electron microscope is observed. The SEM image is used to choose points and areas where Raman spectra are taken. Raman spectra taken at points with different shades confirm the darker areas to be graphene flakes, because the G peak is visible for these areas. The intensity of the G peak is stronger for darker areas, which suggests that darker patches are thicker graphene. To further investigate the correspondence between SEM images and Raman measurement a spatial Raman measurement is done. On an area of 11 μm by 11 μm 812 spectra are taken. For each spectrum the area under the G peak is determined. The result is plotted in colour scale and together with the SEM image shown in Figure 5.9. The darkest region in the SEM image exhibits the highest intensity of the G peak shown in yellow. A less dark region in the SEM images also is observed as a modest intensity shown in red. The correspondence between SEM images and Raman measurements is confirmed. Because of the correspondence between optical images and SEM images this means that images made with an optical microscope can be used to find graphene patches. In what follows it will be shown that it is possible to at least qualitatively judge on their thickness based on their colour.

For a more quantitative judgement on the thickness of graphene both the ratio of the intensities of the G vs. 2D peak and the shape of the 2D peak are used. Figure 5.10 shows spatial maps for one of the measurements shown in Figure 5.7. The left image shows the intensity ratio of the G vs. 2D peak. A larger ratio indicates a relatively higher G peak, which corresponds to thicker graphene. The right image is the result of a cluster analysis for the same measurement, which helps to use the shape of the 2D peak to determine the thickness. In this spatial map each colour corresponds to a particular cluster. There is a clear correspondence between the two

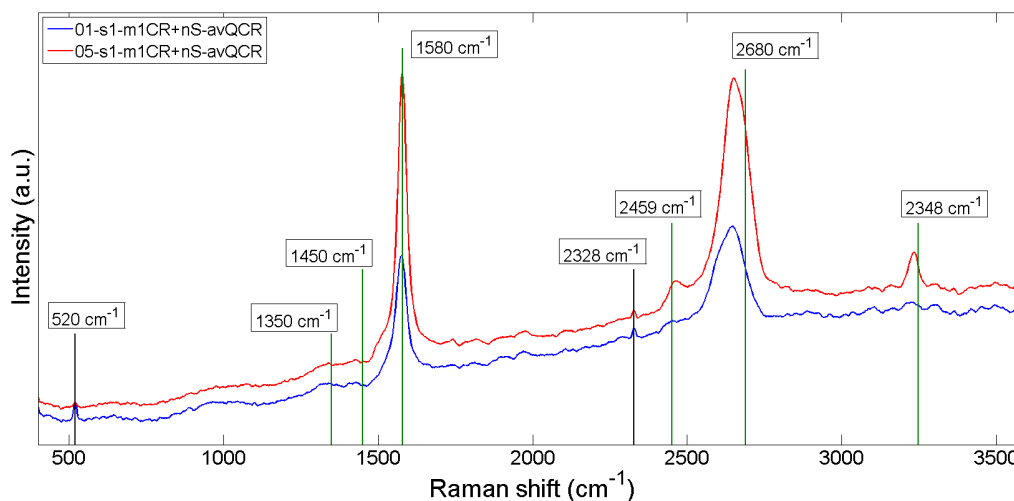
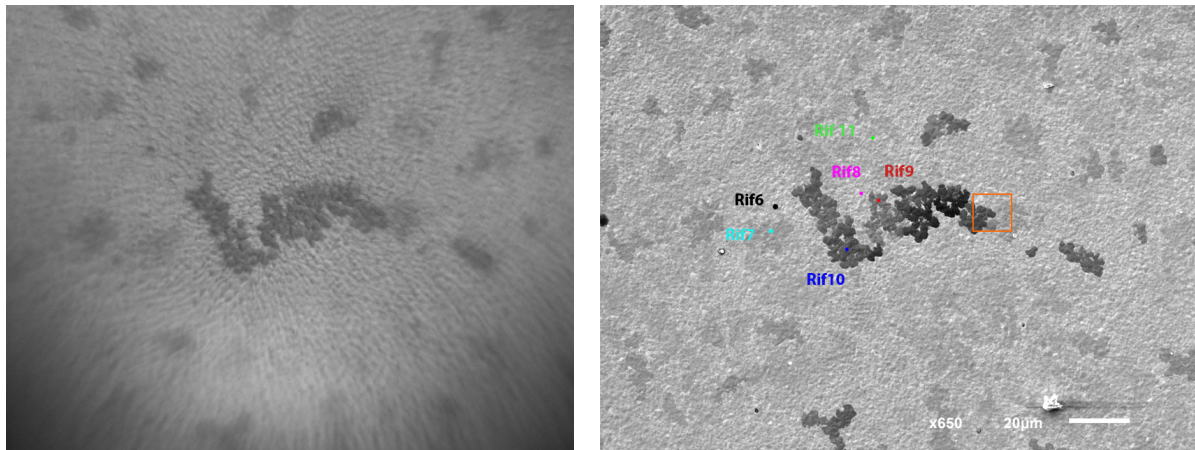
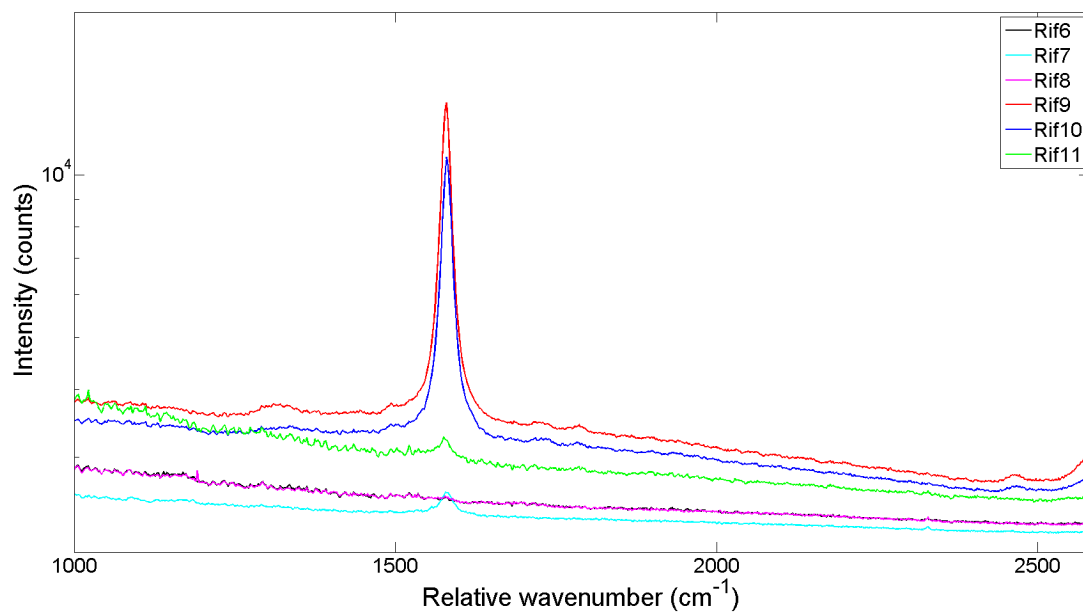


Figure 5.7 – Average Raman spectra for graphene on nickel (wafer 1) obtained in the MCBP group with an excitation wavelength of 647.1 nm. Each curve is the average of 4096 spectra obtained on an area of 30 μm x 30 μm . Green lines indicate the expected Raman shifts for graphene of the main peaks as well as some less pronounced peaks. Black lines mark peaks originating from silicon (520 cm^{-1}) and nitrogen (2328 cm^{-1}) respectively.



(a) Optical microscope

(b) Scanning electron microscope



(c) Average Raman spectra obtained with an excitation wavelength of 784.8 nm.

Figure 5.8 – Results of measurements done at HybriScan Technologies[®]. In Figure 5.8(a) and Figure 5.8(b) the same patch-like features are visible. The spectra shown in Figure 5.8(c) all are the average of five consecutive measurements that are taken at the points marked with matching colours in Figure 5.8(b). A spatial Raman measurement is done for the area marked by the orange square in Figure 5.8(b). The result of this measurement is shown in Figure 5.9.

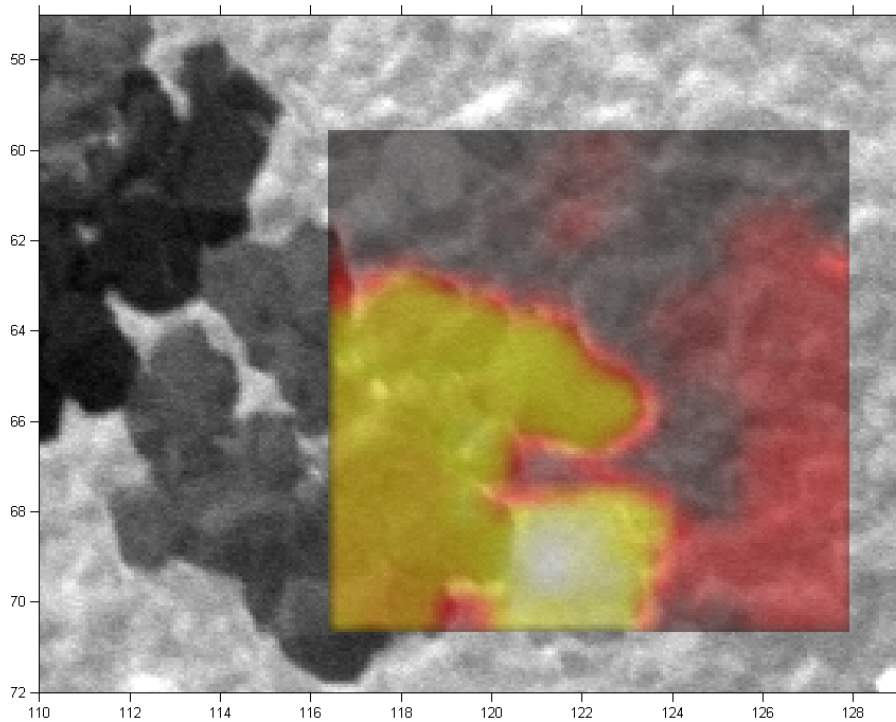


Figure 5.9 – Result of measurements done at HybriScan Technologies[®]. In colour scale the intensity of the G peak in Raman measurements with an excitation wavelength of 784.8 nm is shown. The background image is a SEM image. Numbers on the axis are micrometers.

spatial maps, but also differences are observed. For example, the region with highest ratio is not visible in the cluster image. The ratio images already shows more variation in this region and also the maps for the G and 2D intensities are noisy, which is assumed to be caused by surface enhanced Raman scattering (SERS) effects occurring in this region. Apparently this results in an almost negligible intensity for the 2D peak, which results in a high value for the G/2D ratio. No other data is available to find out what causes this. A typical spectrum for each cluster is determined. For four out of twelve clusters the typical spectrum is noisy, shows a large silicon peak at 520 cm^{-1} and has an intensity much larger than the other spectra. These clusters only occur for a few pixels and can be attributed to SERS effects, and are not taken into account in further analysis. Analysis of both the relative heights of the G and 2D peak and the shape of the 2D peak for different measurements showed that monolayer graphene can be distinguished from multilayer graphene by comparing the relative heights of the G and 2D peak. The thinnest regions have a spectrum in which the G peak is substantially smaller than the 2D peak, while for thicker regions these peaks have a comparable height. For the measurement shown here this yields that clusters 2 and 10 correspond to the thinnest regions. A more detailed analysis is done by using a scaled and zoomed image of the 2D peak for the relevant spectra as shown in Figure 5.11, which shows clear differences between the spectra. This confirms that clusters 2 and 10 correspond to a thin layer. The other clusters can be grouped from thin to thick as: (1 & 5), (3, 4 & 11) and (6). This order is in agreement with what one intuitively would consider thinner and thicker regions in Figure 5.10(b) and also corresponds to an increasing G/2D ratio. It is not possible to judge on the stacking order and the exact number of layers from this measurement. As discussed in section 3.2.2 this would be possible if different excitation wavelengths can be used.

To calibrate the different shades of the patches observed in optical images Raman measure-

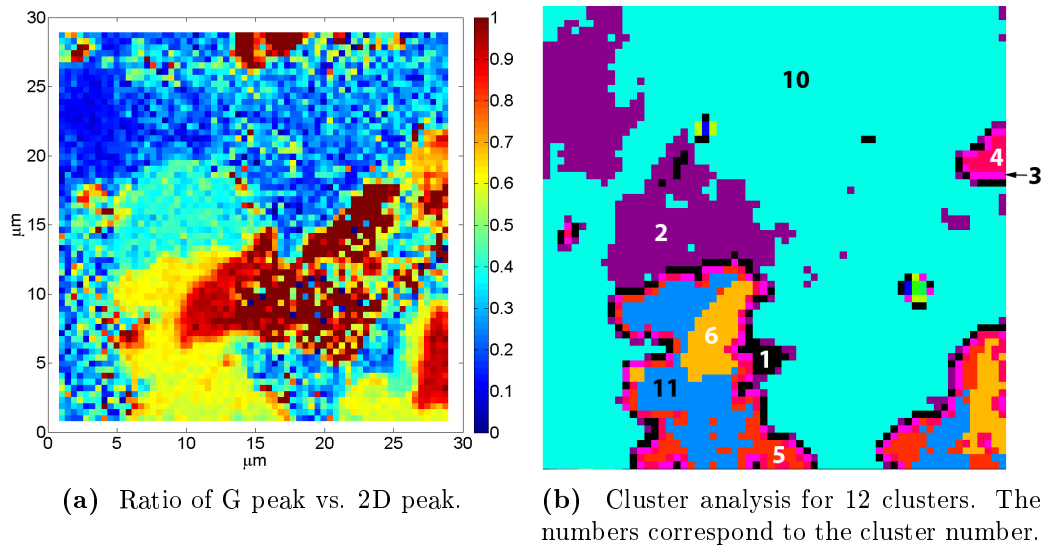


Figure 5.10 – Maps of spatial Raman measurement 05-s1-m1CR+nS-QCR. An area of $30\ \mu\text{m} \times 30\ \mu\text{m}$ is divided in 4096 pixels ($64\ \text{pixels} \times 64\ \text{pixels}$) and for each pixel a spectrum is taken with an excitation wavelength of $647.1\ \text{nm}$.

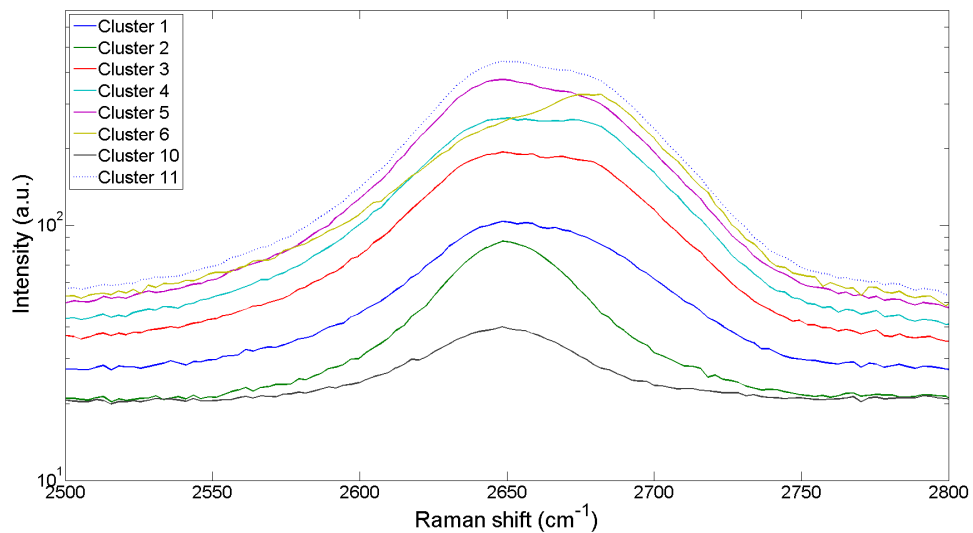


Figure 5.11 – Zoom of the 2D peak of Raman spectra for clusters of interest corresponding to the spatial map shown in Figure 5.10(b). Spectra are taken with an excitation wavelength of $647.1\ \text{nm}$.

ments are done on a sample that is covered with a marker pattern that can be recognised in both optical images and Raman measurements. For this purpose a method commonly used in the NanoElectronics group, which is referred to as bitmarkers, is used. Each marker is formed by a square that is subdivided in 16 smaller squares. Each of these smaller squares is either covered with material or left blank. This way a total of $2^{16} = 65536$ unique markers can be formed. These bitmarkers are written by means of EBL in a layer of resist. Other group members use a positive resist, deposit a metal and use lift-off to end up with markers formed by the metal. To simplify the fabrication process and because most metals do not have a pronounced Raman signal a negative resist (AR-N 7520) is used in this case. The markers are thus formed by the organic resist material. The small squares are $1.5 \mu\text{m}$ by $1.5 \mu\text{m}$, so a marker is $6 \mu\text{m}$ by $6 \mu\text{m}$. The distance between the markers is $25 \mu\text{m}$, because the maximum scan range for the used Raman set-up is $30 \mu\text{m}$.

Spatial images and spectra of the relevant clusters for one of these measurements are shown in Figure 5.12 and Figure 5.13 respectively. For these measurements an area of $30 \mu\text{m}$ by $30 \mu\text{m}$ is divided in 4096 pixels ($64 \text{ pixels} \times 64 \text{ pixels}$) and for each pixel a spectrum is taken. Suitable parameters are required to recognise the bitmarkers in cluster images. None of the available options are used. Clustering in two clusters is done for $1500\text{--}1650 \text{ cm}^{-1}$.

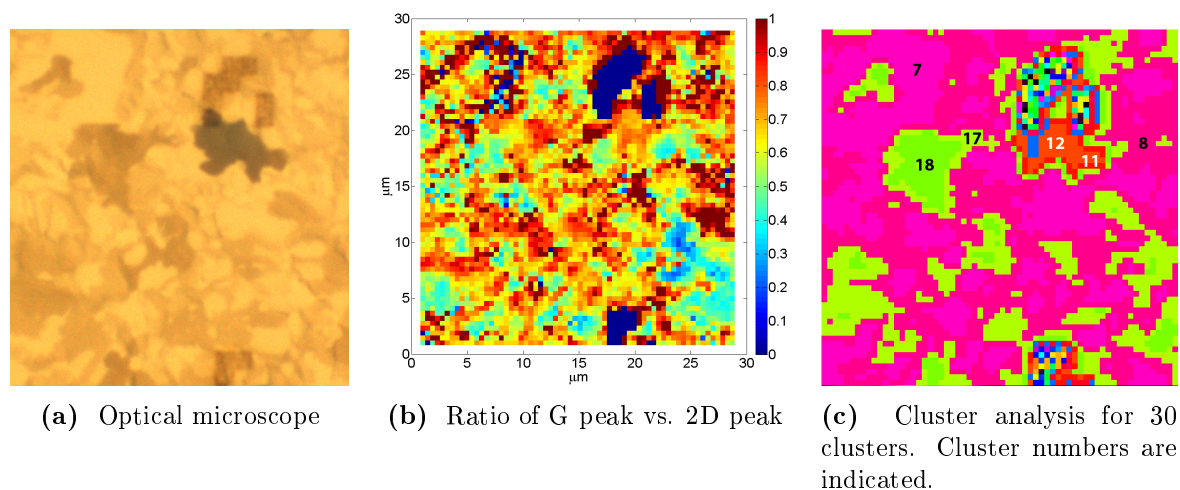


Figure 5.12 – Spatial images corresponding to a Raman measurement on a sample covered with bitmarkers. Markers are clearly distinguishable in optical images. The correspondence between the optical and cluster image is clear. Features in the ratio image can be recognised, but the correspondence is not as good as shown in Figure 5.10(a).

Cluster images for the different measurements done on the sample covered with bitmarkers are made for $2600\text{--}2750 \text{ cm}^{-1}$ without using any of the other options. The number of clusters is adjusted for each measurement in order to obtain the best results. These images show a beautiful correspondence with the corresponding optical images, i.e. flakes of different shade in the optical image can be easily recognised in the cluster image. For these measurements wafer two is used and it should be noted that the D peak is more pronounced than in the measurements for wafer one. This indicates that more defects are present in the graphene layer on this wafer, but there are still not too many defects. A higher intensity and a larger G/2D ratio is observed for cluster spectra corresponding to darker flakes. However, the spectra do not show as much difference in the 2D peak as is observed in previous measurements, such as shown in Figure 5.11. Only the curve for cluster 12, which corresponds to the darkest flake in all measurements, has a main peak at the higher relative wave number side of the 2D peak. Other curves do show a shoulder at this side, which is more pronounced for darker flakes, but in most cases this is not as pronounced

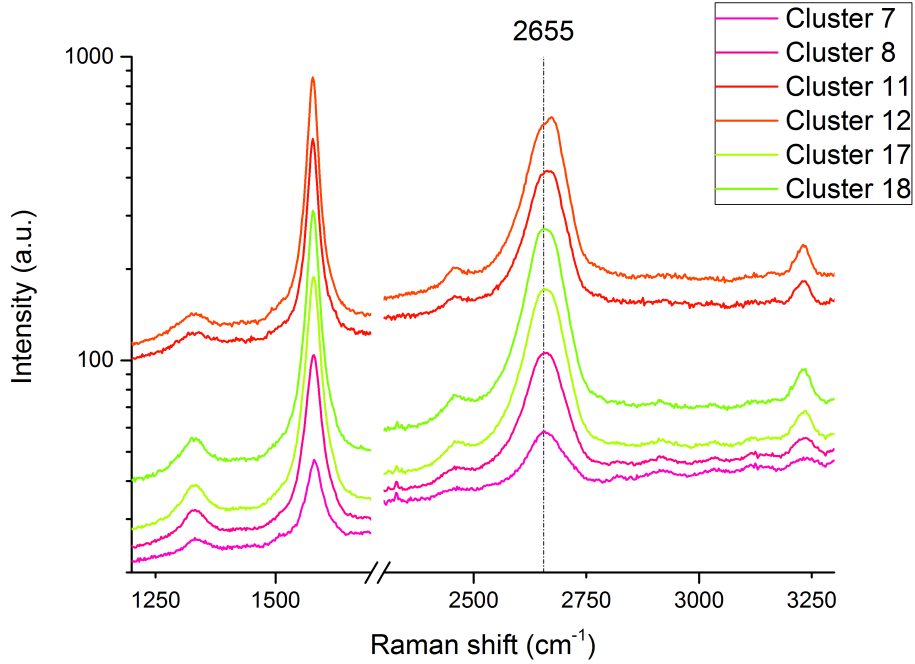


Figure 5.13 – Spectra of the relevant clusters as indicated in Figure 5.12(c). The vertical line at 2655 cm^{-1} shows the peak to shift a bit and to be slightly asymmetric for clusters 11, 12, 17 and 18. Clusters 7 and 8 are estimated to be a single layer, cluster 17 and 18 correspond approximately to three layers and clusters 11 and 12 have a thickness of about five layers. The excitation wavelength is 647.1 nm .

as seen before. This confirms that darker flakes are thicker graphene layers. The intensity is used to compare clusters in the same measurement and the G/2D ratio and the shape of the 2D peak are used to compare between different measurements. In addition, the graphs given by Nguyen *et al.* for 632.8 nm (1.96 eV) are used as reference. Several scans are combined to order the different observed shades and assign an estimate for the number of layers to them. However, these measurements do not allow for a decisive conclusion yet. Figure 5.14 gives the approximate number of layers for the different observed shades. In section C.1 more details are given. The obtained estimate of the thickness of graphene layers allows for thickness dependent measurement to verify the predicted dependence on thickness.

5.2 Device fabrication

In this section different steps in the fabrication process and the methods used to check them are discussed.

5.2.1 Lithographic alignment of junctions

The predicted spin filtering effect saturates at five graphene layers, so for a first proof of principle it is desirable to define junction on thicker graphene patches. Furthermore, the used measuring techniques requires high quality junctions, so a smooth junction area is preferable. This can be achieved by contact holes that are smaller than the nickel grains, but in order to obtain the smoothest junctions the contact holes should also be in the middle of a grain. These requirements can be met by using EBL to define the contact holes and use both optical images and AFM images for alignment of the contact holes.

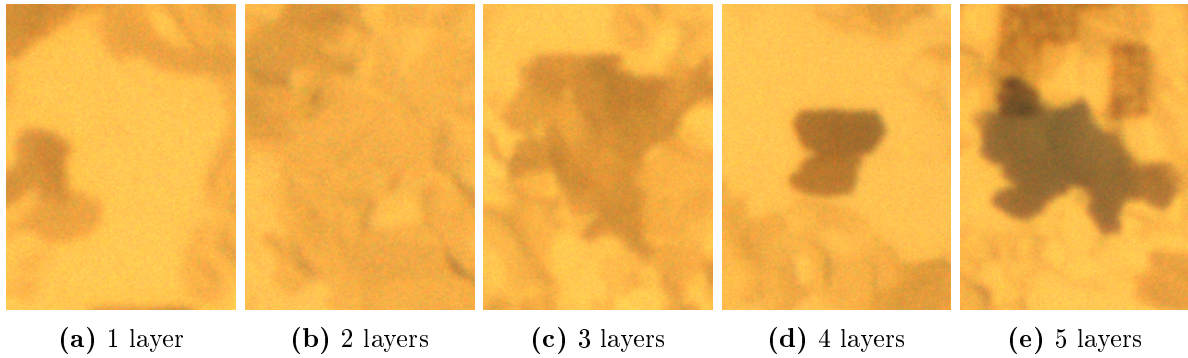


Figure 5.14 – Optical images of the shades corresponding to graphene layers of different thickness. The number of layers is an estimate based on comparison with curves given by Nguyen *et al.*, the observed intensities for different cluster in a single measurement and the observed shade. The width of the images is 7–10 μm .

As shown in the previous section optical images can be used to find suitable graphene patches. AFM measurements at these patches can be used to align the contact holes in the middle of a grain. In Figure 5.15 an optical images and a large AFM image of the same area are shown. Different software can be used to align these images by using the cross markers visible in the

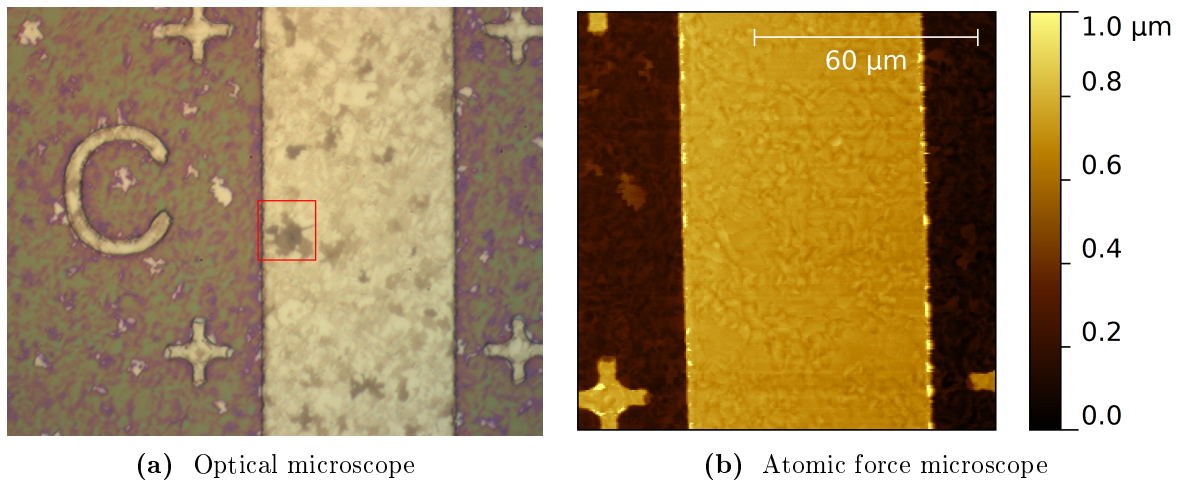
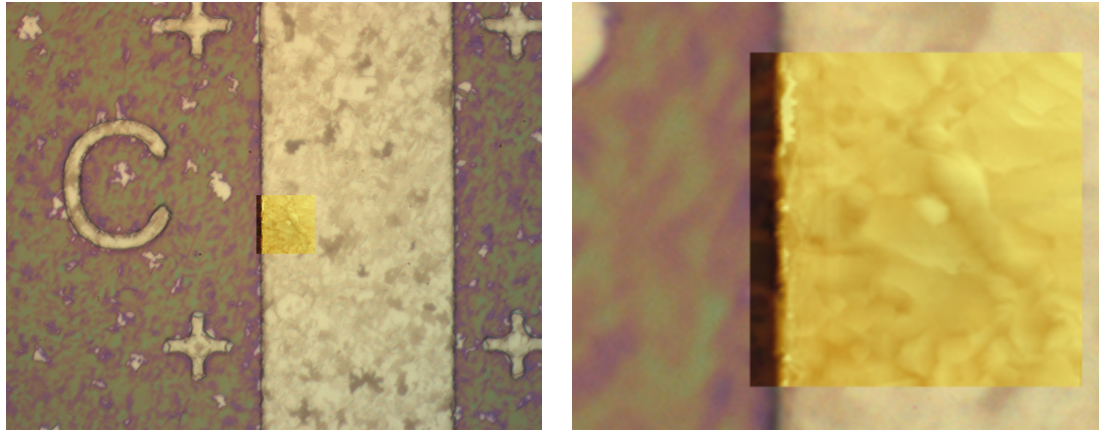


Figure 5.15 – Optical microscopy image and AFM image of the same area. In the optical image graphene patches are visible. Alignment is shown in Figure 5.16 for the area marked with the red square.

corners of both images. To begin with Photoshop is used for this purpose. Successive AFM measurement of smaller areas are aligned to the prior AFM scan by using features on the surface. The result is a detailed AFM scan aligned on an optical image as shown in Figure 5.16.

Comparing Figure 5.16(b) with Figure 5.15(a) obviously reveals the possibility to use such combined images to determine suitable locations for contact holes on top of a graphene sheet of preferred thickness, i.e. in the middle of a nickel grain. Subsequently, the optical image can be loaded into the EBL software and aligned to the photolithography pattern used to define the bottom electrodes.⁷ Finally, the contact hole can be placed in the EBL pattern at the chosen

⁷ Instead of using Photoshop or other graphical software it also is possible to load both the optical and the AFM image in the EBL software. However, the Photoshop option to let a layer be partially transparent is especially



(a) Overview. The distance between crosses is $100\ \mu\text{m}$.

(b) Zoom. The AFM scan is a bit smaller than $20\ \mu\text{m}$.

Figure 5.16 – Combined optical and AFM images. These images are the result of aligning Figure 5.15(b) on Figure 5.15(a) by using Photoshop. Successive smaller AFM images are aligned on the prior images. Only the smallest AFM scan is shown in the combined images. Figure 5.16(b) is a zoom of the relevant area of Figure 5.16(a).

location. In this project AFM images are not used yet and the location of the contact holes is only determined based on optical images, but in the preceding it is shown that using AFM images in addition to optical images would improve the fabrication process.

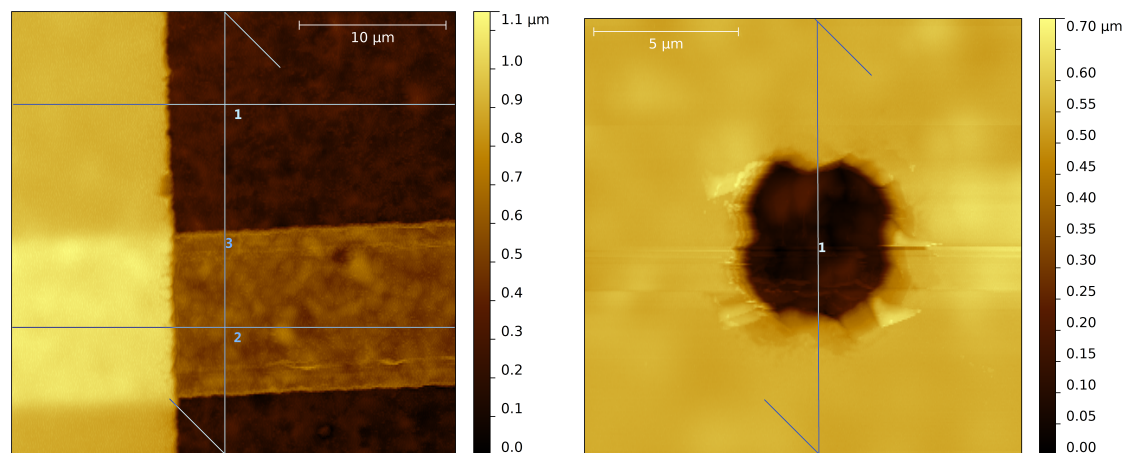
5.2.2 Bottom electrodes, resist layer and contact holes

The bottom electrodes are defined in the nickel-graphene layer by means of ion beam etching. It is important that in the etched areas the nickel layer is completely removed to make sure that there are no current paths between different bottom electrodes. It is no problem to etch deeper than strictly necessary, so the etching time in which all nickel is removed is roughly determined, but not too much time is spent to optimise this. The resistance between different bottom electrodes was measured to make sure that they are not connected. The found etching time is used thereafter and differed between wafer 1 and wafer 2 due to the different thickness of the nickel layer.

The resist layer as well as the contact holes defined in this layer are of significant importance, because the goal is to obtain well defined junctions at the locations where the contact holes are made without other current paths existing between bottom and top electrodes. On the one hand it is important that the resist layer is insulating. On the other hand the contact holes should allow for good contact between the bottom electrode and the top electrode. Throughout this project different types of resist have been used depending on the method used to define the contact holes (photolithography or EBL). The insulating properties of the resist layer have been tested by fabricating devices without contact holes and measuring the resistance between top and bottom electrodes. Diluted photoresist forms an insulating layer, but for PMMA this is not always the case. The standard spin speed of 4,000 rpm resulted in a resist layer with a finite resistance. Fabricating and testing devices with PMMA layers of different thickness by varying the spin speed during spin coating showed that reducing the spin speed to 2,000 rpm is sufficient to obtain an insulating layer for most bottom electrodes. However, a later test sample with the same fabrication conditions showed a finite resistance for several bottom electrodes. Time was

useful for alignment.

lacking to investigate this in more detail and completely solve the problem. Figure 5.17 shows AFM images of the edge of the insulating photoresist layer on top of a bottom electrode and of a photolithographically defined contact hole. The height of the bottom electrode is a bit more



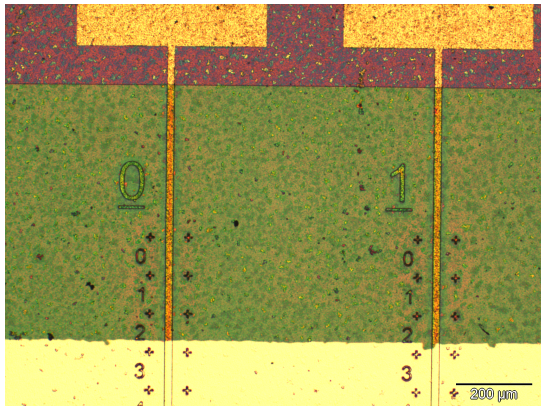
(a) Edge of photoresist on top of a bottom electrode fabricated with wafer 1. (b) Photolithographically defined contact hole.

Figure 5.17 – AFM images. Fits along the lines indicated in Figure 5.17(a) show the bottom electrode to have a height of a bit more than 300 nm and the photoresist to have a thickness of 0.6 μm next to the bottom electrode and 0.5 μm on top of the bottom electrode. From a fit along the line indicated in Figure 5.17(b) the depth of the contact hole is determined to be 0.5 μm.

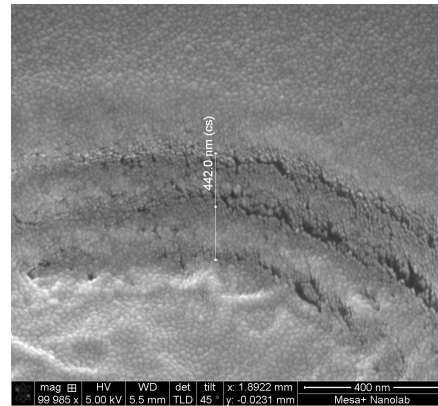
than 300 nm, as expected, because etching is done a bit deeper to make sure that the nickel layer is completely etched away. The photoresist layer is half the thickness of undiluted OiR 906/12 and it is observed that planarisation of the photoresist takes place to some extent. The depth of the contact hole is in agreement with the thickness of the photoresist. The walls are not very steep.

The alignment of photolithographic contact holes with the bottom electrodes is checked by means of an optical microscope. The alignment accuracy of $\sim 1 \mu\text{m}$ determines the maximum possible size of a contact hole for a given width of the bottom electrodes. Raman measurements showed signatures of amorphous carbon at the edges of the bottom electrodes, so to be on the safe side the contact holes should be at least 4 μm smaller than the bottom electrodes. Figure 5.18 shows an optical microscopy image and a SEM image of a finished device with photolithographically defined contact holes. In the optical image the purple area is the Si/SiO₂ substrate, the yellowish areas are the bottom electrodes, the large green area is photoresist and the top electrode is visible in white at the bottom of the image. The SEM image indicate the contact hole after deposition of the top electrode to be about 450 nm deep, which is a bit less than before the deposition, so the top electrode is a bit thicker in the contact hole than on top of the photoresist. The top electrode does not seem to be continuous everywhere at the edges of the contact hole. The ridges in the wall of the contact hole visible in the SEM image are caused by the standing wave pattern in the exposure step in photolithography. The different layers in the top electrode have an intended total thickness of 47.5 nm, but the thickness can not be inferred from this image.

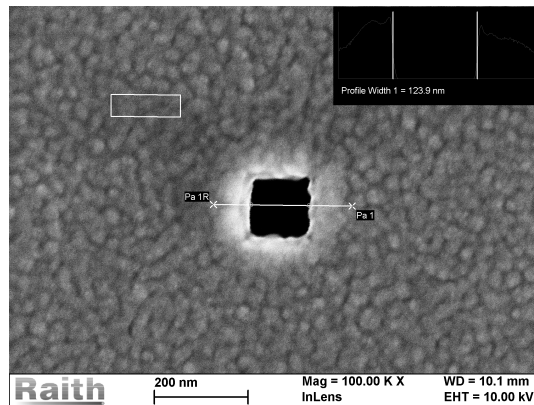
Contact holes defined by means of EBL are checked with SEM in the EBL set-up. The result is shown in Figure 5.18(c). The size of the contact hole is 124 nm, which is a bit smaller than the intended 150 nm. The intended total thickness of the top electrode for this device is 50 nm, but it is not possible to determine the actual thickness from this image.



(a) Optical microscope



(b) Scanning electron microscope



(c) Scanning electron microscope

Figure 5.18 – Images of finished devices. Figure 5.18(a) and Figure 5.18(b) are for a device with photolithographically defined contact holes. The optical image shows all different parts of the device. In the SEM image the contact hole is depicted. Figure 5.18(c) shows a contact hole defined by means of EBL.

5.2.3 Top electrode

The critical point for the top electrode is the continuity of the different layers, which can be hampered by the roughness of the used substrate. The top electrode as a whole should be continuous to enable measurements in general. In order to achieve this the layer of photoresist is made as thin as possible, while maintaining its electrically insulating properties. The observed planerisation as well as the not too steep walls of the contact holes are favourable for a continuous top electrode. A capping layer is deposited to increase the total thickness of the top electrode, which should ensure a continuous electrode. Furthermore, both the tunnel barrier formed by aluminium oxide (AlO_x) and the aluminium layer should be continuous and closed in the contact holes for Tedrow-Meservey measurements to be possible. If this is not the case for the AlO_x layer there is an Ohmic contact between top and bottom electrode, i.e. the electrodes are not decoupled sufficiently. In addition, Tedrow-Meservey measurements depend on the narrow gap in the density of states of a material in the superconducting state. This gap hampers transport for small bias voltages. If the superconducting layer is not closed conduction paths that bypass this layer can exist and transport is possible through these conduction paths for bias voltages inside the gap. As a result the gap does not manifest itself in the measurements and thus Tedrow-Meservey measurements are not possible. Both layers can not be made too thick, so the contact holes are made smaller and placed in the middle of a grain to reduce the roughness within the contact hole area. A thicker tunnel barrier reduces the current dramatically, because the wave function decays exponentially inside the barrier. This will result in a too low signal to noise ratio. The superconductor can not be too thick, because the critical field for bulk aluminium is too low to be able to do Tedrow-Meservey measurements. Other superconductors (i.a. Be, MgB_2 , VTi and Ta) are considered, but aluminium is the only simple to deposit superconductor with favourable properties and without major disadvantages like the materials being costly or toxic or the need for destructive deposition techniques.

The continuity of the top electrode as a whole simply is confirmed by passing a current from one side of the electrode to the other or through a junction. This was not a problem in any of the fabricated devices. A continuous AlO_x layer results in the non-linear IV curves characteristic for tunnelling. For a continuous aluminium layer no current can exist at very small bias and at temperatures for which the aluminium is superconducting. This will be discussed in the next section.

Other issues with the top electrode can be the quality of the tunnel barrier and the smoothness of the aluminium layer. A tunnel barrier of low quality can cause noise and unstable junctions. The quality of the tunnel barrier is enhanced by natural oxidation after deposition. The oxidation time varied between 60 and 90 minutes for different device batches. Without detailed research the yield and quality of the junctions seems to be better for longer oxidation times. Tedrow-Meservey measurements require a high quality junction with a smooth aluminium layer. This is hampered by surface roughness. Smaller contact holes placed in the middle of a grain also help to prevent this issue.

5.3 Transport measurements

The following section contains results of transport measurements on different samples. Because no general behaviour is observed the results are presented junction by junction. The subsections are named after a sample and junction number. For all experiments the exact device design is specified, i.e. width of the bottom electrodes, size of the square contact holes and the material and thickness of the layers in the top electrode. The layers of the top electrodes are mentioned in the order in which they are deposited, so from bottom to top.

5.3.1 Photolithographically defined contact holes

A lot of devices are fabricated with photolithographically defined contact holes. Only the most important ones will be discussed below. Due to the size limitation of photolithography the used contact holes have a minimum size of $2\ \mu\text{m}$. As a result the junction is likely to be on more than one nickel grain and there probably is a large height difference within the junction area. Both points are disadvantageous for well defined junctions. Furthermore, the location of contact holes is random, so the details of the junction (eg. the graphene thickness) are not known.

Device 140128-3 - Junction A9

For this device wafer 1 is used, the width of the bottom electrodes is $40\ \mu\text{m}$ and the size of the contact holes is $10\ \mu\text{m}$. The top electrode consists of $2.5\ \text{nm}$ aluminium oxide, $40\ \text{nm}$ permalloy and $5\ \text{nm}$ aluminium. The purpose of this device lay-out is to investigate the properties of the tunnel barrier formed by aluminium oxide. Permalloy is used in the top electrode, because it is a ferromagnetic material, which makes it possible to measure a TMR signal in addition to the normal tunnelling curves in order to further characterise the tunnel barrier. Results of temperature dependent IV measurement are shown in Figure 5.19. The measurements show non-linear tunnelling curves. There is a temperature dependence, but it is not too large. At $5\ \text{K}$ the zero-bias resistance-area product is $0.06\ \Omega\cdot\text{cm}^2$, which is quite low, but not unreasonable. Although tunnelling is observed in the IV measurement, the signal turned out to be too noisy to measure TMR. These results show that a tunnel barrier of good enough quality is achieved.

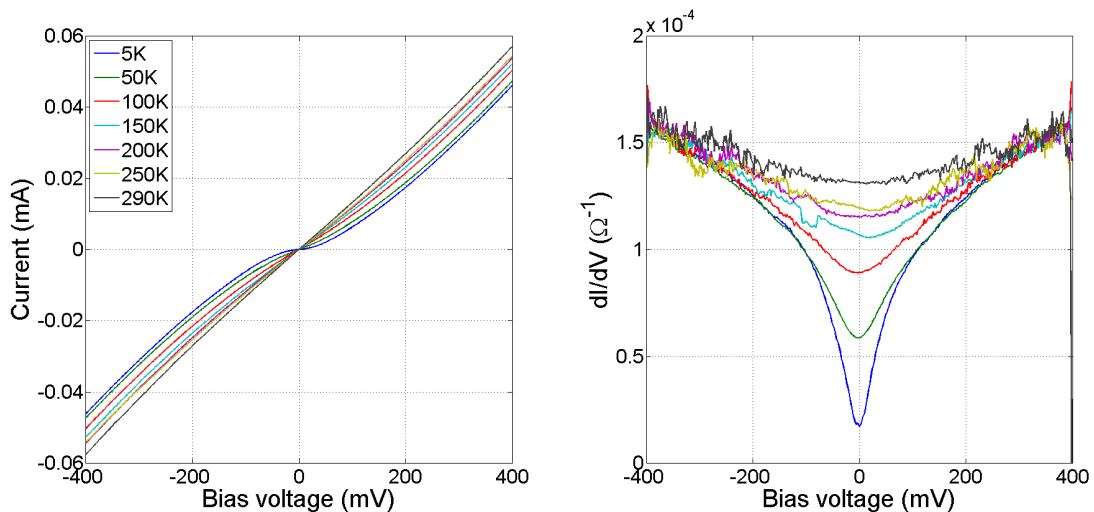


Figure 5.19 – Plots of current (I , left) and conductance (dI/dV , right) as a function of voltage (V) for junction A9 on sample 140128-3 at different temperatures. Curves are smoothed over 5 and 15 points respectively.

Device 140205-1 - Junction C3

For this device wafer 1 is used, the width of the bottom electrodes is $20\ \mu\text{m}$ and the size of the contact holes is $4\ \mu\text{m}$. The top electrode consists of $2.5\ \text{nm}$ aluminium oxide, $5\ \text{nm}$ aluminium and $62\ \text{nm}$ platinum. The curves corresponding to these measurements are shown in Figure 5.20. The results of these measurements in general show neat non-linear tunnelling behaviour. At $50\ \text{K}$ the zero-bias resistance-area product is $0.15\ \Omega\cdot\text{cm}^2$. However, at the lowest temperatures a region of negligible conductance is observed. This gap has a width of several tens of meV. It

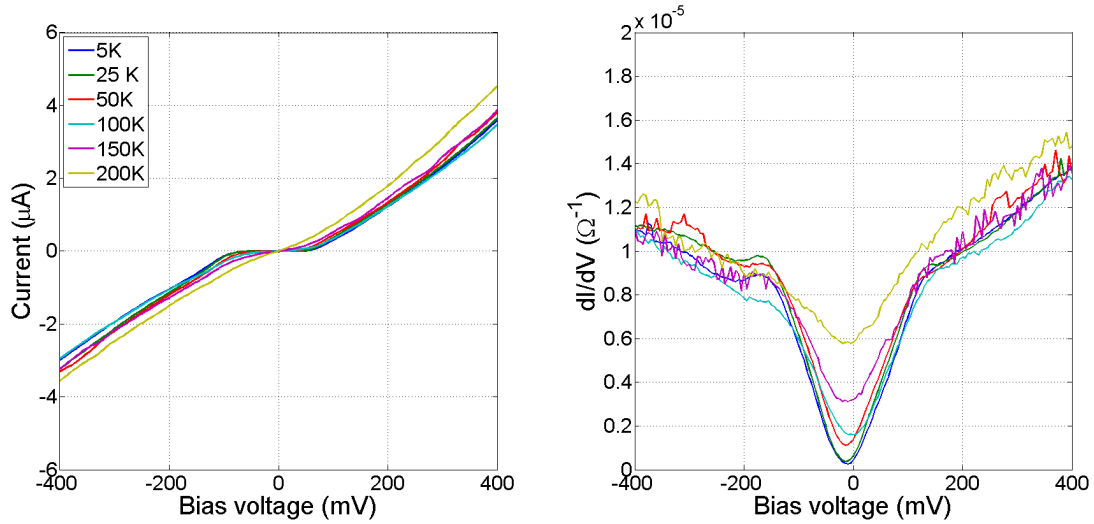


Figure 5.20 – Plots of current (I , left) and conductance (dI/dV , right) as a function of voltage (V) for junction C3 on sample 140205-1 at different temperatures. Curves are smoothed over 5 and 25 points respectively.

is observed for measurements up to 25 K, but is significantly reduced at 50 K. The size of the gap and its temperature dependence suggest Coulomb blockade, which arises when conduction takes place via an isolated 'nanoisland'. Nanoislands could be the result of a metallic defect in an otherwise rather insulating junction area. The tunnel barrier is of reasonable quality, but the observed gap will overwhelm any superconducting gap. Junctions that show such a gap are thus not suitable for Tedrow-Meservey measurements.

Device 140429-7 - Junction A6

For this device wafer 1 is used, the width of the bottom electrodes is 20 μm and the size of the contact holes is 10 μm . The top electrode consists of 2.5 nm aluminium oxide, 4.5 nm aluminium and 72.5 nm copper. Results are shown in Figure 5.21. In these low temperature

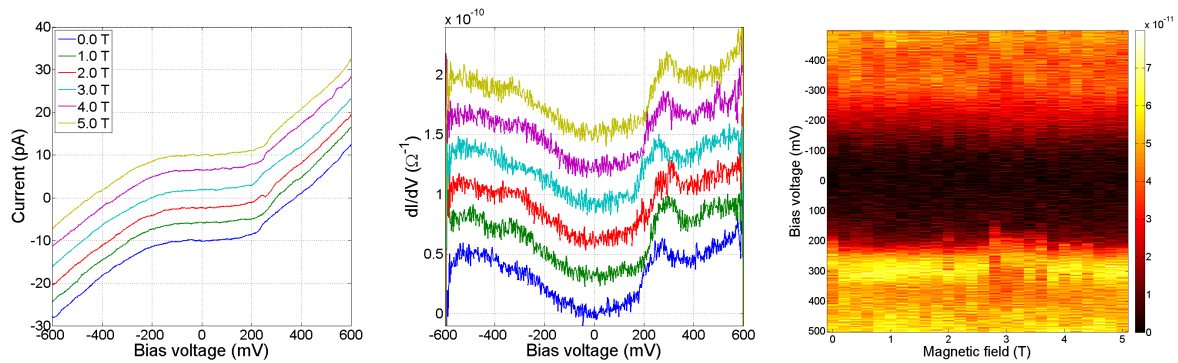


Figure 5.21 – Plots of current (I , left) and conductance (dI/dV , middle) as a function of voltage (V) for different magnetic fields for junction A6 on sample 140429-7 at 270 mK. Curves are displaced for clarity and smoothed over 5 and 40 points respectively. In the right image the conductance (in Ω^{-1}) is represented by the colour scale as a function of bias voltage and magnetic field.

measurements a gap with zero conductance is observed, but the gap is very wide (almost 400 mV) and the gap does not close with increasing magnetic field. This gap thus can not be related to superconductivity. As for the previously presented junction a possible explanation for this gap

can be a metallic defect in the junction area, which gives rise to Coulomb blockade. Obviously a gap like this makes it impossible to do Tedrow-Meservey measurement that depend on the very narrow superconducting gap. There is a slight dependence on magnetic field, but on this scale it is not possible to distinguish a Zeeman shift, because its expected magnitude is much smaller.

Device 140429-9 - Junction 4

For this device wafer 1 is used, the width of the bottom electrodes is $20\ \mu\text{m}$ and the size of the contact holes is $10\ \mu\text{m}$. The top electrode consists of $2.5\ \text{nm}$ aluminium oxide, $4.5\ \text{nm}$ aluminium and $72.5\ \text{nm}$ copper. Results are shown in Figure 5.22. Around zero bias voltage a region of sig-

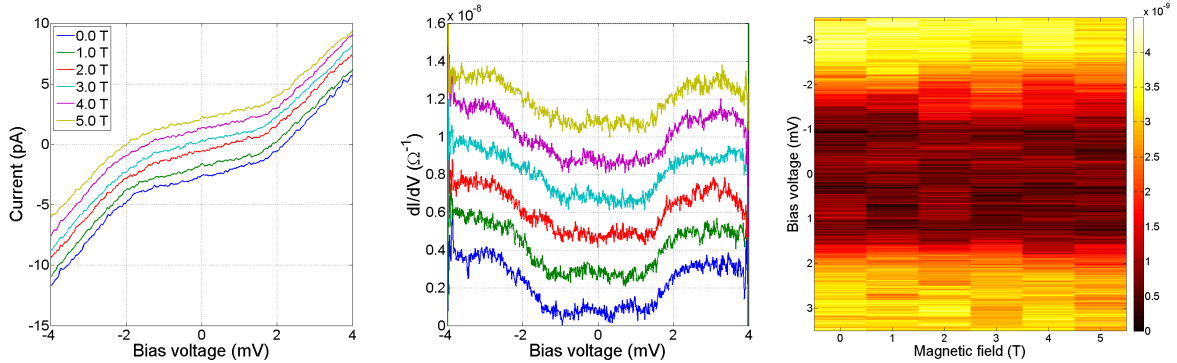


Figure 5.22 – Plots of current (I , left) and conductance (dI/dV , middle) as a function of voltage (V) for different magnetic fields for junction 4 on sample 140429-9 at a temperature below $50\ \text{mK}$. Curves are displaced for clarity and smoothed over 5 and 60 points respectively. In the right image the conductance (in Ω^{-1}) is represented by the colour scale as a function of bias voltage and magnetic field.

nificantly lower, but finite, conductance is observed. This can be caused by parallel conductance paths bypassing the superconducting aluminium layer or by the absence of superconductivity in combination with a defect state in the tunnel barrier that gives rise to the suddenly increasing conductance. To characterise the top electrode and search for signatures of superconductivity several wires are bonded at different points on this electrode and IV measurements are done at temperatures of several tens of mK. The measured resistance is finite and neatly scales with the length of the segment of the top electrode between the bonded wires. No (quenching of) superconductivity is observed in these measurements, but the maximum applied current is $20\ \mu\text{A}$ and no magnetic field is applied. For the case that all current would flow through the aluminium layer the current density is $3.70 \cdot 10^7\ \text{Am}^{-2}$, which is much lower than the value for the critical current for thin aluminium films reported in literature,³⁶ so it is questionable whether the critical current density is reached in case superconductivity would be present. From these measurements it can not be concluded whether superconductivity is present or not, which makes it impossible to determine the origin of the finite conductance within the gap.

5.3.2 Contact holes defined by means of EBL

The first batch of devices with contact holes defined by EBL suffered from a not insulating PMMA layer. This makes the location of the junctions uncertain, which is one of the main reasons to use EBL, and it is possible that more than one junction exist for a single bottom electrode. Therefore the thickness of the PMMA layer is increased by reducing the spin speed to $2,000\ \text{rpm}$, such that only the contact holes allow current to flow between top and bottom

electrode. In total five devices are fabricated with a thicker PMMA layer. Three devices (140820-2, 140820-4 and 140820-6) are fabricated in a first deposition run of the top electrode and the other two devices (140820-3 and 140820-5) are fabricated in a second deposition run. The difference between these two deposition runs is the thickness of the different layers in the top electrode. Two out of three devices in the first batch were measured. Only two junctions on these devices were not shorted, but in these junctions no superconductivity was visible. Therefore, in the second deposition run the thickness of the AlO_x tunnel barrier was increased from 2.5 nm to 3.5 nm and the thickness of the aluminium layer was increased from 5 nm to 10 nm. Most junctions of the devices made in the second deposition run showed an infinite resistance, which means that the resistance scales with the thickness of the tunnel barrier as expected, but the layer is too thick now.

Device 140617-2 - Junction 9

For this device wafer 1 is used, the width of the bottom electrodes is 60 μm and the size of the contact holes is 150 nm. The top electrode consists of 2.5 nm aluminium oxide, 5 nm aluminium and 42.5 nm copper. Curves of IV measurements for this device show that a working tunnel barrier also can be achieved with the altered device design with smaller contact holes defined by EBL. At 5 K the zero-bias resistance-area product is $5.6 \cdot 10^{-5} \Omega \cdot \text{cm}^2$. This is very low in comparison with what is observed in previous junctions, but this can be caused by a larger fraction of the total area really contributing to conduction. This is shown in Figure 5.23.

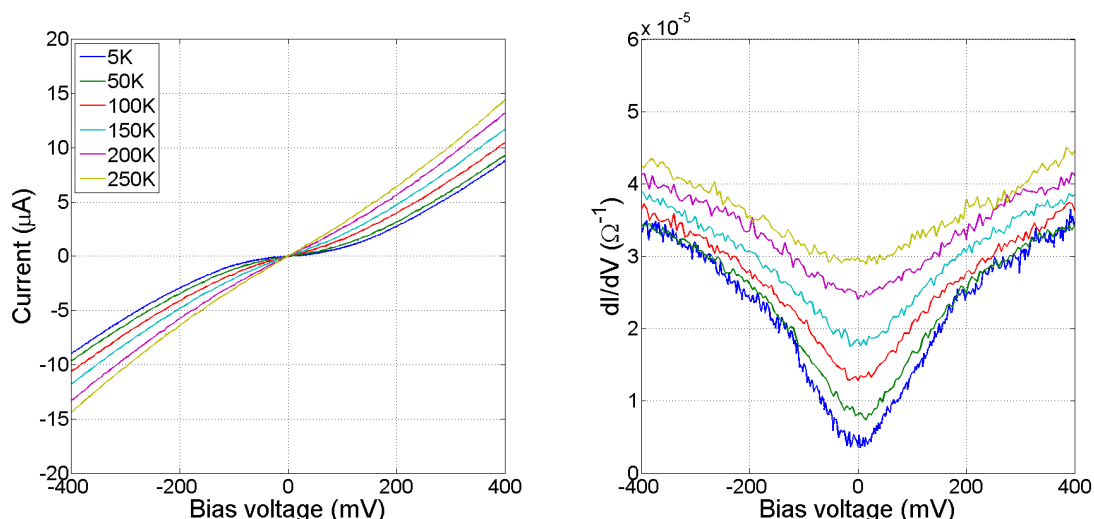


Figure 5.23 – Plots of current (I , left) and conductance (dI/dV , right) as a function of voltage (V) for junction 9 on sample 140617-2 at different temperatures. Conductance curves are smoothed over 15 points.

Device 140820-3 - Junction 9

For this device wafer 2 is used, the width of the bottom electrodes is 60 μm and the size of the contact holes is 150 nm. The top electrode consists of 3.5 nm aluminium oxide, 10 nm aluminium and 37 nm copper. Figure 5.24 shows the results of measurements for different values of the magnetic field. A region of reduced conductance around zero bias is observed, but inside this 'gap' the conductance is not completely zero. The zero-bias resistance-area product is $0.01 \Omega \cdot \text{cm}^2$. Furthermore, the IV curves show several kinks, which manifest themselves as peaks in the conductance curves. The peaks appear at asymmetric bias voltages and shift towards zero

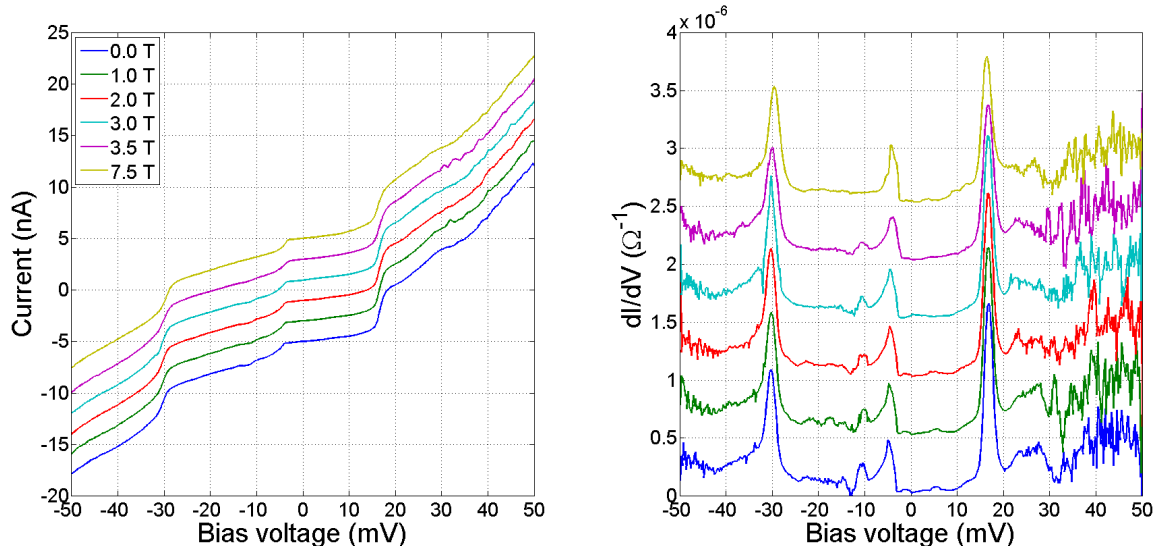


Figure 5.24 – Plots of current (I , left) and conductance (dI/dV , right) as a function of voltage (V) for different magnetic fields for junction 9 on sample 140820-3 at 297 mK. Curves are displaced for clarity and smoothed over 5 and 10 points respectively.

bias voltage with increasing magnetic field. For the peaks at -30 mV and 17 mV the general trend is a lower and wider peak for higher field, although not all curves follow this trend. For larger bias voltages the curves become noisy.

The non-zero conductance inside the gap can be explained by the complete absence of superconductivity or by an unclosed aluminium layer, such that parallel conduction paths are available. These parallel conduction paths can then account for the conductance for bias voltages inside the superconducting gap. A probable origin of the peaks are discrete defect states in the tunnel barrier. Defect states give rise to a peak for both positive and negative bias. Asymmetry in the peak positions is caused by an asymmetric geometrical location of the defect inside the barrier, which is referred to as the lever arm effect. A detailed explanation and analysis of the lever arm effect can be found in section A.2. The effect of the magnetic field on the peaks is understood from Zeeman splitting of these defect states, which causes each peak to split in two peaks. Peak broadening is a general effect due to the Zeeman effect, because these two peaks shift away from each other, while leaving their center unaffected. In the case of a spin polarised current, however, the peaks do not have the same height and thus contribute differently to the total peak. As a result their centre is changed, which is observed as a shift of the peak maximum. The combination of the energy of the defect with respect to the Fermi level (above or below the Fermi level) and which of the spin directions is more abundant in the current determines the direction of the peak shift. From these measurements it is not possible to determine which combination occurs.

The aforementioned lever arm effect also affects the peak shifts caused by Zeeman splitting, because Zeeman splitting effectively changes the energy of the defect as explained in section A.2. This can be used to determine which peaks correspond to the same defect. To compare the peak shifts zooms of the conductance curves are shown in Figure 5.25. The peak maxima and shifts are summarised in Table 5.1. Peaks with the same sign for the bias can not belong together, so it only makes sense to compare the ratios for peak 1 vs. peak 3 and for peak 2 vs. peak 3. The relevant ratios are also stated in Table 5.1. From the ratios it can be concluded that peak 2 and peak 3 do not correspond to the same defect. For peak 1 and 3, the ratio between the positions and the ratio between the shifts both are approximately two for the

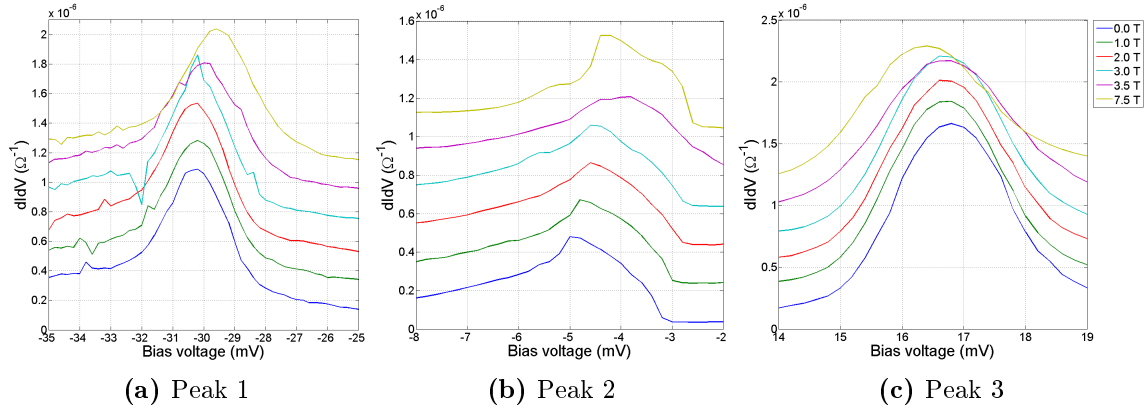


Figure 5.25 – Zooms of the conductance curves shown in Figure 5.24 for the three most pronounced peaks. Curves are displaced for clarity and smoothed over 10 points.

B (Tesla)	Peak 1		Peak 2		Peak 3		1 vs. 3		2 vs. 3		1 vs. 2
	Pos.	ΔV	Pos.	ΔV	Pos.	ΔV	Pos.	ΔV	Pos.	ΔV	ΔV
0.0	-30.3		-5.0		16.8		1.80		0.30		
1.0	-30.3	0.0	-4.8	0.2	16.7	0.1	1.81	0.00	0.29	2.00	0.00
2.0	-30.2	0.1	-4.6	0.4	16.6	0.2	1.82	0.50	0.28	2.00	0.25
3.0	-30.2	0.1	-4.6	0.4	16.7	0.1	1.81	1.00	0.28	4.00	0.25
3.5	-29.9	0.4	-3.8	1.2	16.6	0.2	1.80	2.00	0.23	6.00	0.33
7.5	-29.6	0.7	-4.4	0.6	16.4	0.4	1.80	1.75	0.27	1.50	1.17

Table 5.1 – The first three columns give the maxima of the peaks (Pos.) observed in Figure 5.25 and the corresponding shifts (ΔV) with respect to zero magnetic field. Positions and shifts are in mV. The general trend is a shift towards lower voltages, but deviations from this trend are clear. The columns titled '1 vs. 3' and '2 vs. 3' give the ratios between peak positions and peak shifts for the corresponding peaks. The last column ('1 vs. 2') only gives the ratio in peak shifts, because the position ratio is not relevant.

largest magnetic fields (for which the shifts are easier to evaluate), suggesting that these features originate from the same defect state in the barrier. Assuming this to be the case, taking a ratio of $\frac{1}{1.8}$ (the ratio of the peak positions is less sensitive to small variation) and using the expressions in Equation A.2 yields $x = 0.64$. The energy of the defect with respect to the Fermi level (either above or below) can be calculated from any of the first two expressions in Equation A.1: $E_D = 0.64 \times 16.8 = 10.8 \text{ meV}$. For a magnetic field of 3.5 T the weighted Zeeman shift is estimated by $\Delta E_D = 0.36 \times 0.4 = 0.14 \text{ meV}$. An estimate for absolute value of the Zeeman shift at 3.5 T is given by $E_Z = 2\mu_B B = 2 \cdot 9.274 \cdot 10^{-24} \text{ J/T} \cdot 3.5 \text{ T} = 6.5 \cdot 10^{-23} \text{ J} = 0.41 \text{ meV}$. Using Equation A.3 yields as estimates $P = \frac{0.14 \text{ meV}}{0.41 \text{ meV}} = 0.34$ and $a = \frac{P+1}{2} = 0.67$, which indicates that one of the spin orientations is about twice as abundant in the tunnel current as the other orientation. It should be noted that this analysis contains a lot assumptions and approximations, so its results should not be valued to much, but it can serve as a first general analysis. No other peak that can correspond to peak 2 is visible, so it is reasonable to assume this peak to be caused by a defect for which the lever arm effect is so strong that the corresponding peak at positive bias lies in the noisy region above 30 mV or even not in the measured bias window. Using the expressions in section A.2 results in $x \leq \frac{1}{7}$, $\Delta E_D \geq \frac{6}{7} \Delta V_-$ and $\frac{\Delta V_{-,1}}{\Delta V_{-,2}} \geq \frac{1-\frac{1}{7}}{1-0.64} = 2.4$. The ratios in the last column of Table 5.1 show it to be unlikely that the peak at positive bias corresponding to peak 2 will occur for such a high voltage, which indicates that this peak should be visible in the measured bias window. Reducing the lower limit of the possible bias region for this peak to 20 mV (where the curves already contain some noise) only reduces the last ratio to $\frac{\Delta V_{-,1}}{\Delta V_{-,2}} \geq \frac{1-\frac{1}{5}}{1-0.64} = 2.2$, which is still larger than the values in the last column of Table 5.1. Another possibility is that the peak is completely drown out by the noise.

IV measurements are done on the top electrode of this sample in a search for a signature of superconductivity. For small currents (so small bias voltages) it is expected that the aluminium layer is in the superconducting state. As the current exceeds the critical current superconductivity is quenched and an increase in the total resistance is expected. This would express itself as kinks in the IV curves. Since the critical current gets smaller with increasing magnetic field these kinks, if present, are expected for smaller currents (voltages) at higher magnetic field. The measurements showed a constant resistance over the whole bias range between -4 V and 4 V. The maximum applied current is 0.57 mA, which yields a current density of $4.75 \cdot 10^7 \text{ Am}^{-2}$ in the case that all current flows through the aluminium layer, which is still significantly lower than the value for the critical current of thin aluminium films reported in literature.³⁶ The resistance does not change with magnetic field. No signature of superconductivity is observed, but no conclusion can be drawn concerning the presence or absence of superconductivity based on these measurements.

Device 140820-5 - Junction 7

For this device wafer 2 is used, the width of the bottom electrodes is 60 μm and the size of the contact holes is 150 nm. The top electrode consists of 3.5 nm aluminium oxide, 10 nm aluminium and 37 nm copper. Of all measurements done the curves for this junction most closely resemble the expected curves, in particular features consistent with a superconducting gap in a narrow region around zero bias voltage, but not everything is as expected and not everything is understood. An optical image of the targeted graphene flake for this junction and both IV and conductance curves are shown in Figure 5.26. The conductance curves show a gap and peaks similar to the curves predicted and measured by Tedrow and Meservey. Although the curves are already smoothed they still contain a lot of noise, which is probably caused by the high resistance of the junction and consequently the small currents. Inside the gap the conductance is zero for this junction. The colour plot in Figure 5.27 provides more insight. The gap is

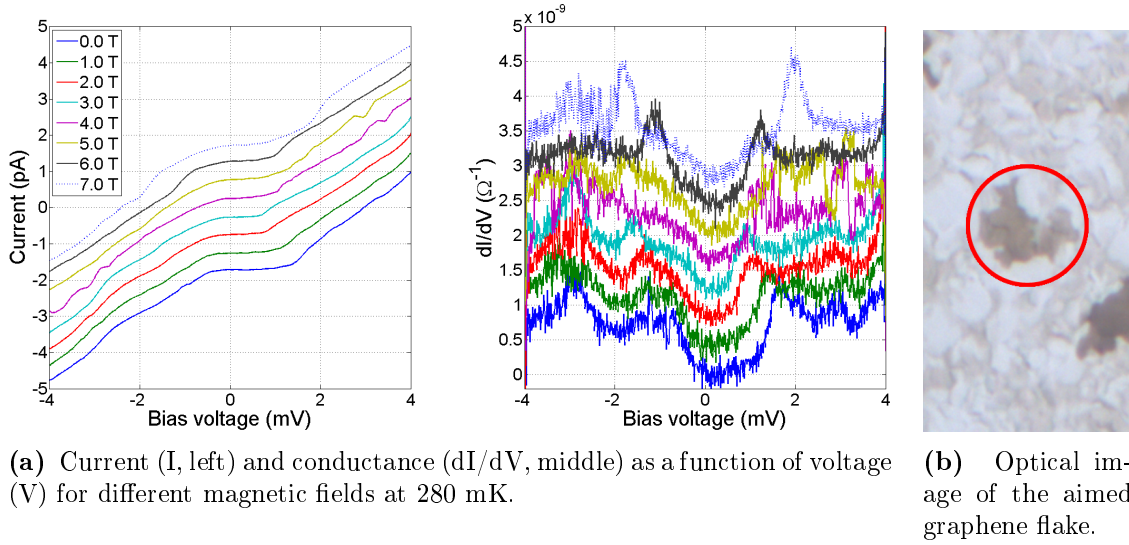


Figure 5.26 – Sample 140820-5 - Junction 7. Curves in Figure 5.26(a) are displaced for clarity and smoothed over 20 and 40 points respectively. The red circle in Figure 5.26(b) indicates the targeted flake.

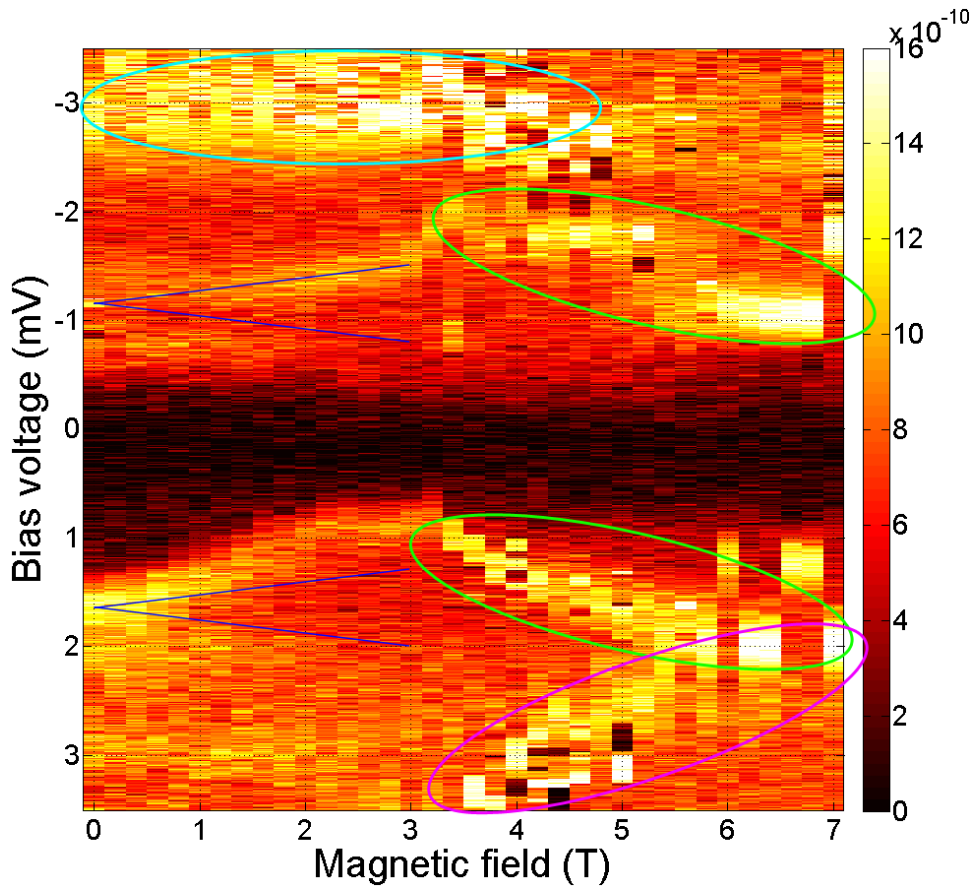


Figure 5.27 – Conductance (dI/dV in Ω^{-1}) represented in colour scale as a function of bias voltage and magnetic field for junction 7 on device 140820-5 at 280 mK. Data is smoothed over 30 points. Blue lines indicate the expected Zeeman shift and the pink and green lines are discussed later.

asymmetric around zero voltage and for magnetic fields up to 3 T the peaks at the gap edges shift upwards and the gap becomes narrower. Furthermore, less pronounced features starting at the same bias voltages at 0 T shift downwards. For magnetic fields above 3 T the width of the gap remains constant and several other features are observed of which the peaks indicated by pink and green ellipses are the most pronounced. What exactly causes the asymmetric gap is not known, but it has been observed before in similar measurements done in the NanoElectronics group. A possible explanation can be the asymmetry of the device in terms of materials at the different sides of the junction.

Temperature dependent IV measurements are done for different magnetic fields to find out whether the observed gap originates from superconductivity. These measurements show the gap to become narrower and eventually close at higher temperatures as is most clearly seen from the conductance curves, which is consistent with the suppression of superconductivity. Current and conductance curves as well as colour plots are depicted in Figure 5.28. The gap

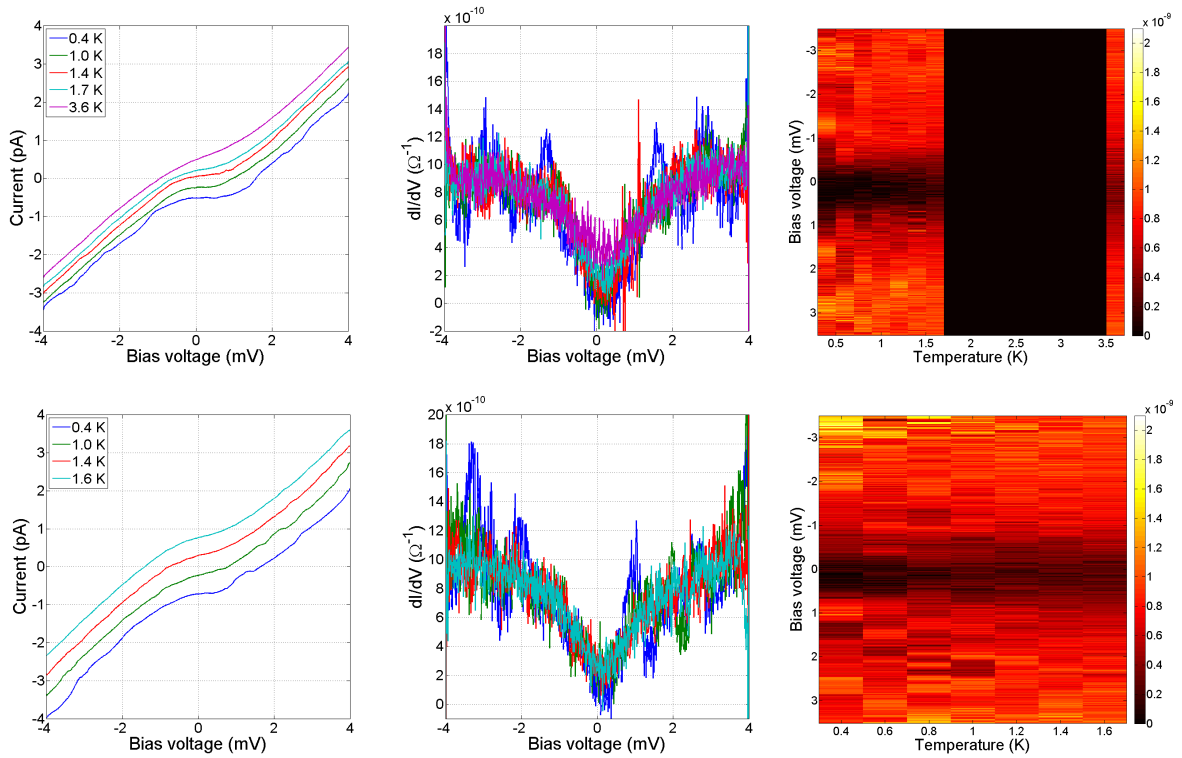


Figure 5.28 – Plots of current (I , left) and conductance (dI/dV , middle) as a function of voltage (V) for different temperatures for junction 7 on sample 140820-5 at both 0 T (top) and 6.9 T (bottom). Curves are smoothed over 20 and 40 points respectively and current curves are displaced for clarity. In the right images the conductance (in Ω^{-1}) is represented (again for 0 T and 6.9 T) in colour scale as a function of bias voltage and temperature. No measurements are done at the temperatures in the black region.

is less clear at 6.9 T and seems to be closed at lower temperature. However, the temperature dependence is weaker in this case. As will be explained later, the gap at 6.9 T is expected to not be caused by superconductivity, so care should be taken while comparing these images. The critical temperature is not obvious from these measurements, but from the measurements for 0 T a reasonable estimate seems to be a bit above 1.6 K. The critical temperature for bulk aluminium is 1.2 K. Meservey and Tedrow showed that the value for the critical temperature estimated here is not unreasonable for a thin aluminium film.¹⁶ Furthermore, superconducting features (i.e. a gap with peaks at the edges) are shown to disappear at high magnetic field, which

is in agreement with theory. The expected critical field for a thin aluminium film is a few Tesla, but not as high as almost 7 T. The observations made here are not in agreement with the known behaviour. The proposed explanation is that superconductivity is completely quenched at 3 T, but a gap with an other origin remains. What causes this gap is not certain, but a metallic defect that shows Coulomb blockade is a possible explanation. For a thin film with a thickness of 10 nm the expected critical field is approximately 2 T.¹⁶ The proposed explanation for the observed higher critical field of about 3 T is an aluminium film formed by islands due to the roughness of the underlying substrate. This causes a reduction in size in an extra direction, which has been shown to enhance critical parameters of a superconductor.³⁷ Although the film in this case is thicker than what Townsend *et al.* defined as Particulate "Films" their observations are considered applicable, because the film is deposited on a rough surface, so islands are expected even for thicker films.

Up to magnetic fields of about 3 T, the conductance curves are qualitatively similar to the expected curves of a junction comprising of a ferromagnetic material, a tunnel barrier and a superconductor, as studied previously by i.a. Tedrow and Meservey. Peaks in the conductance are observed close to the gap edges that shift linearly with magnetic field, consistent with Zeeman splitting of the superconducting DOS. Based on literature the expected Zeeman splitting is approximately 0.12 meV/T,³⁸ which is represented by the blue lines in Figure 5.27. The observed peaks in principle can then be used to calculate a value for the spin polarisation following the method of Tedrow and Meservey. According to the theoretical prediction of Karpan *et al.* the current through the junction is highly spin polarised for a thick graphene patch. The aimed flake is shown in Figure 5.26(b) and is approximately three layers thick. In that case the current mostly consist of electrons that are the minority electrons in nickel. Following this argument, the most pronounced peaks are attributed to these minority electrons, while peaks corresponding to majority electrons are expected to be very faint. For negative bias the blue lines are close to the observed maxima, but for positive bias the observed shift seems larger. Asymmetry is not expected, but care must be taken in determining the conductance peak positions, however, since the current curves are quite noisy due to the very high junction resistance (in the order of 1 G Ω), such that the extracted conductance maxima become somewhat dependent on the exact data averaging procedure used. Therefore, it is not certain whether to apparent asymmetry is real or an artefact. Since the value for the spin polarisation P strongly depends on the choice of conductance maxima it is not relevant to do the calculations.

Ferromagnetic states of the nickel are not expected to show a dispersion with magnetic field. The bulk DOS of nickel does not have peaks close to the Fermi level, but surface states can exist at, in this case, the nickel/graphene interface. The intense peak at -3 meV indicated by the cyan ellipse seems to be independent of magnetic field up to 4 T and therefore most probably is caused by such a ferromagnetic surface state of the nickel layer. Other features do depend on magnetic field, so they can not be attributed to electronic states at this interface.

The peaks for higher magnetic fields indicated by the pink and green ellipses in Figure 5.27 can not be explained by features of the aluminium layer, the nickel layer or the nickel/graphene interface as explained before. They do not shift linearly with magnetic field, which contradicts the behaviour expected from the regular Zeeman effect and therefore also rules out defect states in the tunnel barrier. Nonetheless, other phenomena with a non-linear response on magnetic field exist. The only layer left that possibly can cause these features is the (multilayer) graphene. An example of a phenomenon that shifts non-linearly with magnetic field is formed by Landau levels in graphene. Landau levels are the result of the presence of a magnetic field, which only allows electrons to occupy orbits that coincide with the cyclotron orbits that have discrete energy values. In regular materials Landau levels are equidistant and their energy depends linearly on magnetic field, but due to the linear dispersion in graphene the energy for Landau levels in

magnetic field B are given by $E_n = \pm v_F \sqrt{n \hbar e B}$, where v_F is the Fermi velocity and n is the level index. However, the distance between the peaks indicated by green ellipses is more or less constant and the two peaks for positive bias shift towards each other. Both points are not possible in the case of Landau levels. Furthermore, Landau levels are only expected to form in a magnetic field perpendicular to the plane, while in this case the magnetic field is applied parallel to the graphene sheet. Therefore, Landau levels are excluded as explanation for these peaks.

Another possible cause of these features is a quantum well formed in the two dimensional graphene layer between nickel and aluminium oxide. A quantum well is a potential well with discrete energy states due to quantum confinement in at least one direction. Although it is an extensively studied research field in semiconductors and finds its application in for example lasers not much is known about it in relation to graphene. The effect of a magnetic field perpendicular to the current in an AlGaAs/GaAs/AlGaAs structure has been studied by Ben Amor et al.³⁹ and their study shows some resemblance with the behaviour of the peaks observed here. Alisultanov and Meilanov theoretically treated the electronic structure of graphene on a thin metal film in the presence of an external magnetic field applied parallel to the substrate surface.⁴⁰ Their configuration is similar to the geometry used here. The biggest difference is the thickness of the film, which is larger in this project. Numerical calculations, however, showed that quantum well effects do not manifest themselves for a thickness of the metal film of more than 80 nm. Two-dimensional chiral electron systems, of which graphene is an example, were theoretically studied by Pratley and Zülicke.⁴¹ Their work treats magnetotunnelling spectroscopy of such systems with magnetic fields applied both parallel and perpendicular to the sample plane. The formation of Landau levels in the later of these cases also is discussed. Partially due to the theoretical nature of this research field time lacked to work out this possibility more elaborately, so at this moment this option can not be ruled out or confirmed yet.

To summarise, these measurements most closely resemble the expected curves and a large part of it is understood and can be explained. Signatures of superconductivity are observed, which is an important step towards the realisation of devices for the envisioned Tedrow-Meservey measurements. There still are aspects of this measurement that are not completely understood and require further research. Several explanations are suggested, but no final conclusion can be drawn concerning their origin.

Chapter 6

Conclusions and recommendations

During the course of working on this master assignment several different smaller and larger steps have been made. First the most important achievements will be summarised followed by a more elaborate discussion on some of these points.

- Although it is not optimised, the purchased substrate of CVD grown graphene on nickel is shown to meet the principle requirements to investigate the theoretical prediction of spin filtering by means of Tedrow-Meservey measurements on small vertical tunnel junctions.
- The correlation between images of the nickel/graphene surface made by optical microscopy, scanning electron microscopy and Raman spectroscopy has been established, which allows for quick estimation of the thickness of graphene.
- Alignment of atomic force microscopy images on optical images has been shown.
- In order to have control over the junctions a method has been developed to align contact holes on a single nickel grain and on top of graphene flakes of different thickness, and define the contact holes in an insulating resist layer by means of electron beam lithography.
- A non-destructive process to fabricate these tunnel junctions has been developed and it is verified that tunnelling is the main transport mechanism for the resulting junctions.
- Low-temperature magnetotransport studies for small, EBL defined junctions are demonstrated. Corresponding conductance plots show defect assisted tunnelling as well as a rich collection of features.
- Partial consistency with tunnelling into the DOS of a superconductor is demonstrated, while also presently unexplained features, which require further study, are shown.

The properties of the bought substrates showed to be subject to variations. Only two substrate are bought, but their properties are different in several aspects. Both wafers consist of nickel grains of several microns and deep valleys in between the grains, which are a result of the high temperature in the process of graphene growth, so the substrates are rough. The grains are smaller and the height differences are larger for the first wafer. The first wafer has a highly polycrystalline nickel layer and the individual crystallites have a random orientation, but for the second wafer a single crystal orientation is found. The proposed spin filter depends on the lattice match of graphene with the nickel (111) surface and on the combination of the electronic structures at this interface. The perfect spin filtering effect is not expected for other orientations of the nickel, so realising efficient spin filtering with the first wafer is problematic. Graphene flakes are larger than the nickel grains, so they grow over grain edges. For that reason also the

second wafer probably does not have the desired lattice match throughout the whole substrate. Currently, no way to involve this in the choice for the location of junctions is available. In case it would be possible to obtain less rough substrates this would be recommendable, but it is questionable whether this is possible due to the general process parameters in the CVD growth.

The properties of the graphene layers match the expectations. It consist of patches with a size of several microns and the patches have different thickness. However, optical comparison of the two wafers shows the coverage of the first wafer to be not so good. Raman spectroscopy showed the quality of the graphene layers to be reasonably good, but graphene on the second wafer has more defects. Extensive work is done in combining Raman spectroscopy with other kind of measurements, which include optical microscopy, scanning electron microscopy and atomic force microscopy. An elaborate literature study is done to get familiar with the possibilities of Raman spectroscopy in graphene research in order to use it both in this project and in the future research in the NanoElectronics group. Based on the results of the Raman experiments optical images are calibrated such that they can be used to obtain an estimate of the thickness of graphene. Furthermore, a method is developed to use both optical images and AFM images to choose the location of the junctions. This way information about the nickel and the graphene layers is combined, such that suitable spots on the substrate are used. This also offers the possibility to perform measurements for different thickness of graphene in the future.

Efforts in this work focussed on the properties of the bottom electrode and the placement of the junctions. Less work is done on the insulating layer to separate the bottom and top electrode and on the top electrode itself. Transport measurements showed that in general the device design works as intended, but improvements are necessary to obtain reliable and reproducible results. As insulating layer a resist is used, because it can be easily spin coated, but problems with its insulating properties are encountered. In this project this is partially solved by increasing the thickness of the resist layer, but it still is not completely certain that there are no shorts in this layer. In order to perform more reliable measurements it is recommended to invest more time in optimising the insulating layer. Although resist can be used, also other materials can be considered, for example a thick layer of aluminium oxide, but this makes the fabrication process more complex.

A tunnel barrier is successfully fabricated, but, although the tunnel barrier is not the biggest challenge, the EBL devices revealed challenges related to the thickness and the layer not to be closed. This is more critical for the EBL devices with smaller junction area. Several features in the transport measurements are attributed to defect states in the tunnel barrier, which shows that the tunnel barrier still needs improvement. Signatures of a higher device yield and better quality are observed for longer oxidation times of the aluminium oxide. Therefore more extensive characterisation and optimisation of the aluminium oxide layer, which includes optimisation of the oxidation process, is recommended. An alternative growth method can be considered in order to achieve a layer of higher quality. Atomic layer deposition (ALD) instead of electron beam evaporation can offer more control over the tunnel barrier and help to achieve an uniform layer. The growth of a thin aluminium oxide tunnel barrier by means of ALD recently is reported.⁴²

The thin aluminium layer turned out to be the most challenging. In most measurements no unambiguous signatures of superconductivity are observed, which either shows it to be completely absent or bypassed via other conduction paths. In both cases the aluminium layer requires attention. A neater aluminium oxide layer can be beneficial for the aluminium layer, because it is expected that the difficulties are at least partially caused by the substrate roughness. The used device design starts with an intrinsic rough substrate, which presumably only can be partially solved and thus this should be dealt with. A possible solution is to use the backside of the nickel film, which is in direct contact with the very smooth Si/SiO₂ substrate and thus is expected to be smooth as well. According to the supplier of the wafers used in this project graphene grows

on both sides of a copper film,²⁵ so it is considered worthwhile to investigate this option for nickel films. First attempts with a method referred to as template stripping are made. Indeed the backside is smoother, but no signatures of graphene are observed in Raman measurements. Optimising the fabrication process to facilitate the stripping of nickel, for example by annealing in helium, are possible in order to be able to use the smoother backside of the nickel film. While using the topside of the nickel film, in order to limit the influence of the roughness the junction area already is decreased to 150 nm by 150 nm and it can be considered to reduce it even more. This would require good control over the thickness and quality of the aluminium oxide layer, because the thickness showed to be more critical for the EBL devices and the resulting smaller current requires a lower noise level.

The very last measurements also are the measurements with the most rich and interesting results. Most important, although not decisive, these measurements showed the most clear signatures of superconductivity. This shows it to be possible to obtain working devices suitable for Tedrow-Meservey measurements in order to measure the spin polarisation of the current with the used device design. However, the measured curves exhibit too much noise to be able to draw quantitative conclusions, so less resistive devices are needed. Not all features in these measurements are completely understood. Without being conclusive, possible explanations for the observed peaks are suggested, such as Landau level and quantum well formation in graphene. However, it is argued that Landau levels do not occur and not so much is known about quantum wells in graphene, so currently no satisfying explanation is available.

In the preceding some suggestions and recommendations regarding the current device design are already made. Although this design seems to be the most logical and easy to fabricate design for the proposed measurements it can be worthwhile to consider other, creative, designs. As already noted the most critical layer is the aluminium layer, so it would absolutely be beneficial to start the fabrication process with deposition of aluminium on a smooth substrate. Starting here the most straightforward process is to deposit aluminium, oxidise the top layer, deposit nickel on top and subsequently grow graphene. However, it is questionable whether graphene grows at the interface between aluminium oxide and nickel in case these materials are neatly grown on top of each other. Graphene is required at this interface, because due to the short spin relaxation length in nickel it is not expected that the spin filtering effect can be observed if graphene only is located at the other surface of the nickel film. An alternative approach could be to not deposit the aluminium layer at all, but use it, for example, as the tip of a scanning tunnelling microscope (STM). This would also allow for optimal flexibility in choosing measurement locations. However, Tedrow-Meservey measurements require very low temperatures (superconductivity is needed) and quite high magnetic fields (the Zeeman effect has to be observed), which can be problematic to achieve at the same time in a single STM set up. These two examples of other device designs probably are not very suitable, but it shows that it can be worth it to be inventive.

Review and acknowledgements

Almost a year ago I started working on my master assignment in the NanoElectronics group and by now my time there is almost over. The envisioned work related to experimental realisation of spin filtering at the graphene-nickel(111) interface turned out to be much more challenging than expected. I started with the idea that the fabrication would not be too hard and that we would soon be able to obtain a first proof of principle after which we could extend our view and come up with all different kinds of interesting experiments. However, the realisation of working, stable and reproducible devices consumed more time and even is not completely finished yet. With this my assignment was a bit different from what I expected and that demanded a mind switch. Side steps, such as Raman spectroscopy, with more concrete results helped me with this. In addition, these sidesteps will allow for more valuable experiments later on and therefore were really nice to do. After all I am excited and proud of the work I did and what I accomplished during my master assignment. I already was doubting whether I want to do a PhD. By now I decided I want to do so and I am looking for a position. Although I'll not be able to do them myself, I am looking forward to results on the envisioned transport experiments, such as the Tedrow-Meservey measurements to measure the spin polarisation.

I would not have been able to successfully perform my master assignment work during the last year without the help of several persons. Due to my very broad interest the choice for a research group and a specific topic was a tough one and took some time, but it did not regret my choice at any time and I am pretty sure that I could not have chosen better. Getting to know the NanoElectronics group and its projects better showed that it was a group I really wanted to work in and I am glad I got that chance. I would like to thank all who helped me in that choice. My daily supervisors, dr. Michel de Jong and ir. Elmer van Geijn, of course were amongst them and to them I owe special thanks for the direct guidance and support. Together with prof. Wilfred van der Wiel they offered me the possibility to work in the NanoElectronics group. The discussions and meetings about the obtained results and steps to take were invaluable. Together with prof. Paul Kelly I thank the three of them for being part of my examination committee and assessing my work.

During my work I got help from several others of which I want to mention a few especially. Kai Wang for all his help in the cleanroom and with experiments both in Bruker and Heliox and Johnny Sanderink for his help with the DCA. Of course I also thank all other members of the NanoElectronics group, which are too many to mention here, for suggestions and tips and not to forget the very pleasant time I had there. Raman measurements would not have been possible without the help of Cees Otto and Aufried Lenferink of the MCBP group and HybriScan Technologies[®] for which I am very grateful. The last year I spent quite some time in the MESA+ cleanroom, which I really enjoyed. It is a special experience and I did not want to miss it. It is an inspiring environment to work in and the way everything is taken care of by the staff is very nice.

Although my time as student is not over yet this seems to be the right place and time to thank everyone for the nice time I had during my study in Enschede. I want to thank my

friends especially, but also all associations I was part of in general and S.V.A.T. Astatine in particular. I really liked the atmosphere within these associations and on the campus. I am going to miss being active in all kind of boards and committees. To conclude, I am grateful to all who supported me in my work and in my life in general.

JELMER M. BOTER

Bibliography

- [1] I. Žutić et al. “Spintronics: Fundamentals and applications”. In: *Reviews of Modern Physics* 76 (2004), pp. 323–410. DOI: 10.1103/RevModPhys.76.323 (cit. on pp. 1, 2, 6, 7).
- [2] B. Behin-Aein et al. “Proposal for an all-spin logic device with built-in memory”. In: *Nature Nanotechnology* 5 (2010), pp. 266–270. DOI: 10.1038/nnano.2010.31 (cit. on p. 1).
- [3] K.S. Novoselov et al. “Electric field in atomically thin carbon films”. In: *Science* 306 (2004), pp. 666–669. DOI: 10.1126/science.1102896 (cit. on p. 2).
- [4] W.J.M. Naber et al. “Organic spintronics”. In: *Journal of Physics D: Applied Physics* 40 (2007), R205–R228. DOI: 10.1088/0022-3727/40/12/R01 (cit. on pp. 2, 6–8).
- [5] V.M. Karpan et al. “Graphite and graphene as perfect spin filters”. In: *Physical Review Letters* 99 (2007), p. 176602. DOI: 10.1103/PhysRevLett.99.176602 (cit. on pp. 2, 10).
- [6] V.M. Karpan et al. “Theoretical prediction of perfect spin filtering at interfaces between close-packed surfaces of Ni or Co and graphite or graphene”. In: *Physical Review B - Condensed Matter and Materials Physics* 78.19 (2008), p. 195419. DOI: 10.1103/PhysRevB.78.195419 (cit. on pp. 2, 9–11).
- [7] P.M. Tedrow and R. Meservey. “Spin polarization of electrons tunneling from films of Fe, Co, Ni, and Gd”. In: *Physical Review B* 7 (1973), pp. 318–326. DOI: 10.1103/PhysRevB.7.318 (cit. on pp. 2, 11–13).
- [8] D.P. DiVincenzo. “Quantum computing and single-qubit measurements using the spin-filter effect”. In: *Journal of Applied Physics* 85.8 (1999), pp. 4785–4787. DOI: 10.1063/1.370481 (cit. on p. 2).
- [9] P. Recher et al. “Quantum Dot as Spin Filter and Spin Memory”. In: *Physical Review Letters* 85 (2000), pp. 1962–1965. DOI: 10.1103/PhysRevLett.85.1962 (cit. on p. 2).
- [10] J.S. Moodera et al. “The phenomena of spin-filter tunnelling”. In: *Journal of Physics: Condensed Matter* 19.16 (2007), p. 165202. DOI: 10.1088/0953-8984/19/16/165202 (cit. on pp. 2, 11).
- [11] A.H. Castro Neto et al. “The electronic properties of graphene”. In: *Reviews of Modern Physics* 81 (2009), pp. 109–162. DOI: 10.1103/RevModPhys.81.109 (cit. on pp. 4, 5).
- [12] H. Min et al. “Intrinsic and Rashba spin-orbit interactions in graphene sheets”. In: *Physical Review B* 74 (2006), p. 165310. DOI: 10.1103/PhysRevB.74/165310 (cit. on p. 8).
- [13] D. Huertas-Hernando et al. “Spin-orbit coupling in curved graphene, fullerenes, nanotubes, and nanotube caps”. In: *Physical Review B* 74 (2006), p. 155426. DOI: 10.1103/PhysRevB.74.155426 (cit. on p. 8).
- [14] C. Tannous and J. Gieraltowski. *Magnetic Properties of Electric Materials*. Ed. by S. Kasap and P. Capper. Springer US, 2007, p. 96. DOI: 10.1007/978-0-387-29185-7_4 (cit. on p. 8).

- [15] N. F. Mott. “The Electrical Conductivity of Transition Metals”. English. In: *Proceedings of the Royal Society of London. Series A, Mathematical and Physical Sciences* 153 (1936), pp. 699–717 (cit. on p. 9).
- [16] R. Meservey and P. M. Tedrow. “Properties of Very Thin Aluminum Films”. In: *Journal of Applied Physics* 42 (1971), pp. 51–53. DOI: 10.1063/1.1659648 (cit. on pp. 11, 59, 60).
- [17] P.M. Tedrow and R. Meservey. “Direct observation of spin-state mixing in superconductors”. In: *Physical Review Letters* 27 (1971), pp. 919–921. DOI: 10.1103/PhysRevLett.27.919 (cit. on p. 12).
- [18] R. Meservey and P.M. Tedrow. “Spin-polarized electron tunneling”. In: *Physics Reports* 238 (1994), pp. 173–243. DOI: 10.1016/0370-1573(94)90105-8 (cit. on p. 13).
- [19] R. Meservey et al. “Electron spin polarized tunneling study of ferromagnetic thin films”. In: *Journal of Magnetism and Magnetic Materials* 35 (1983), pp. 1–6. DOI: 10.1016/0304-8853(83)90439-0 (cit. on p. 13).
- [20] M. Ohring. *Material Science of Thin Films*. Ed. by M. Ohring. 2nd. ISBN-13: 9780125249751. Academic Press, 2001 (cit. on p. 15).
- [21] T.A. Nguyen et al. “Excitation energy dependent raman signatures of ABA- and ABC-stacked few-layer graphene”. In: *Scientific Reports* 4 (2014), p. 04630. DOI: 10.1038/srep04630 (cit. on pp. 20–23).
- [22] A.C. Ferrari et al. “Raman Spectrum of Graphene and Graphene Layers”. In: *Physical Review Letters* 97 (2006), p. 187401. DOI: 10.1103/PhysRevLett.97.187401 (cit. on pp. 20–22).
- [23] D.M. Basko. “Theory of resonant multiphonon Raman scattering in graphene”. In: *Physical Review B* 78 (2008), p. 125418. DOI: 10.1103/PhysRevB.78.125418 (cit. on pp. 21, 22).
- [24] R.J. Nemanich and S.A. Solin. “First- and second-order Raman scattering from finite-size crystals of graphite”. In: *Physical Review B* 20 (1979), pp. 392–401. DOI: 10.1103/PhysRevB.20.392 (cit. on p. 21).
- [25] Graphene Supermarket. *Graphene Film on Nickel*. URL: <https://graphene-supermarket.com/One-wafer-100mm-Graphene-Film-on-Nickel.html> (cit. on pp. 22, 32, 65).
- [26] A. Gupta et al. “Raman Scattering from High-Frequency Phonons in Supported n-Graphene Layer Films”. In: *Nano Letters* 6 (2006), pp. 2667–2673. DOI: 10.1021/nl1061420a (cit. on p. 22).
- [27] S. Latil and L. Henrard. “Charge Carriers in Few-Layer Graphene Films”. In: *Physical Review Letters* 97 (2006), p. 036803 (cit. on p. 22).
- [28] A. Dahal and M. Batzill. “Graphene-nickel interfaces: a review”. In: *Nanoscale* 6 (2014), pp. 2548–2562. DOI: 10.1039/c3nr05279f (cit. on p. 22).
- [29] A.L. Patterson. “The Scherrer Formula for X-Ray Particle Size Determination”. In: *Physical Review* 56 (1939), pp. 978–982. DOI: 10.1103/PhysRev.56.978 (cit. on p. 25).
- [30] J.R. Creighton and P. Ho. *Surface Engineering Series*. Ed. by J.-H. Park and T.S. Sudarshan. Vol. Volume 2: Chemical Vapor Deposition. ASM International, 2001, pp. 1–22. DOI: 10.1361/chvd2001p001 (cit. on p. 32).
- [31] D. Hoffman and D. Leibowitz. “ Al_2O_3 Films Prepared by Electron-Beam Evaporation of Hot-Pressed Al_2O_3 in Oxygen Ambient”. In: *Journal of Vacuum Science & Technology* 8 (1971), pp. 107–111. DOI: 10.1116/1.1316256 (cit. on p. 34).

- [32] X.H. Song et al. “Low-temperature scaling of the susceptibility of Ni films”. In: *Physical Review B* 77 (2008), p. 092408. DOI: 10.1103/PhysRevB.77.092408 (cit. on p. 35).
- [33] M. S. Miller et al. “Influence of rf magnetron sputtering conditions on the magnetic, crystalline, and electrical properties of thin nickel films”. In: *Journal of Applied Physics* 75 (1994), pp. 5779–5781. DOI: 10.1063/1.355560 (cit. on p. 37).
- [34] J. Crangle and G.M. Goodman. “The Magnetization of Pure Iron and Nickel”. In: *Proceedings of the Royal Society of London. Series A, Mathematical and Physical Sciences* 321 (1971), pp. 477–491. DOI: 10.1098/rspa.1971.0044 (cit. on p. 37).
- [35] Y. Wang et al. “Fabrication and magnetic properties of hierarchical porous hollow nickel microspheres”. In: *Journal of Materials Chemistry* 16 (2006), pp. 1212–1214. DOI: 10.1039/b517176h (cit. on p. 38).
- [36] R. Romijn et al. “Critical pair-breaking current in superconducting aluminum films far below T_c ”. In: *Physical Review B* 26 (1982), pp. 3648–3655. DOI: 10.1103/PhysRevB.26.3648 (cit. on pp. 53, 57).
- [37] P. Townsend et al. “Superconducting Behavior of Thin Films and Small Particles of Aluminum”. In: *Physical Review B* 5 (1972), pp. 54–66. DOI: 10.1103/PhysRevB.5.54 (cit. on p. 60).
- [38] B. Li et al. “Observation of tunnel magnetoresistance in a superconducting junction with Zeeman-split energy bands”. In: *Physical Review B* 88 (2013), 161105(R) (cit. on p. 60).
- [39] S. Ben Amor et al. “Transverse magnetic field dependence of the current-voltage characteristics of double-barrier quantum well tunneling structures”. In: *Applied Physics Letters* 53 (1988), pp. 2540–2542. DOI: 10.1063/1.100202 (cit. on p. 61).
- [40] Z.Z. Alisultanov and R.P. Meilanov. “On the theory of electronic states of the "epitaxial graphene-quantum-well film" system”. In: *Physics of the Solid State* 54 (2012), pp. 1486–1493. DOI: 10.1134/S1063783412070037 (cit. on p. 61).
- [41] L. Pratley and U. Zuelicke. “Magnetotunneling spectroscopy of chiral two-dimensional electron systems”. In: *Physical Review B* 88 (2013), p. 245412. DOI: 10.1103/PhysRevB.88.245412 (cit. on p. 61).
- [42] M.-B. Martin et al. “Sub-nanometer Atomic Layer Deposition for Spintronics in Magnetic Tunnel Junctions Based on Graphene Spin-Filtering Membranes”. In: *ACS Nano* 8 (2014), pp. 7890–7895. DOI: 10.1021/nn5017549 (cit. on p. 64).

Appendix A

Theory

A.1 Tedrow-Meservey measurements

As explained in section 2.5 the conductance corresponding to a tunnelling current flowing through a superconductor can be used to calculate the spin polarisation of this current. This section serves as an intuitive explanation of this method.

The tunnelling current is proportional to the number of available states on both sides of the tunnel barrier within the bias window. An increase of the bias voltage causes more states to be in the bias window. The number of extra states available is simply given by the DOS integrated over the difference in bias voltage. Therefore the conductance σ , which is the derivative of the current with respect to the bias voltage ($\sigma = \frac{dI}{dV}$), is proportional to the DOS of the materials on both sides of the tunnel barrier.

In Figure A.1 on the next page the combination of a superconductor and a ferromagnetic material separated by an insulating material in the presence of a magnetic field is schematically depicted for different bias voltages. The dotted lines in the images on the left correspond to spin-down electrons. This is reflected in an up-shift of the DOS relative to the Fermi level in the superconductor. These electrons are minority electrons in the ferromagnetic material as is reflected by the relatively small value for the DOS on the right side of the tunnel barrier. In the right images the dashed lines correspond to spin-up electrons, which thus are the majority electrons in the ferromagnetic material. Consequently, in the superconductor the DOS shifted down and the DOS on the right side of the tunnel barrier has a relatively high value.

At zero bias the Fermi level of the ferromagnetic material is in the superconducting gap (Figure A.1(a)) and there will be no current. Applying a small positive bias to the ferromagnetic material results in alignment of the Fermi level in this material with a peak in the DOS of the superconductor for majority electrons, while the Fermi level of the ferromagnetic material is still in the superconducting gap for minority electrons as depicted in Figure A.1(b). This gives rise to a large peak in the conductance curve for this voltage, because a large number of extra states becomes available for tunnelling. A larger positive bias (Figure A.1(c)) leads to the alignment of the Fermi level with a peak for minority electrons. This also gives rise to a peak in the conductance, but this peak is lower, because less states in the ferromagnetic material are involved. A small negative bias (Figure A.1(d)) aligns the Fermi level with a peak in the superconducting DOS for minority electrons. As a consequence, at this bias voltage a peak appears in the conductance, which is quite low, because not so much minority states in the ferromagnetic material are involved. Increasing the negative bias to a larger value (Figure A.1(e)) eventually results in alignment of the Fermi level with a peak corresponding to majority electrons in the DOS of the superconductor, which thus gives rise to a large peak in the conductance due to the large amount of majority state available in the ferromagnetic material.

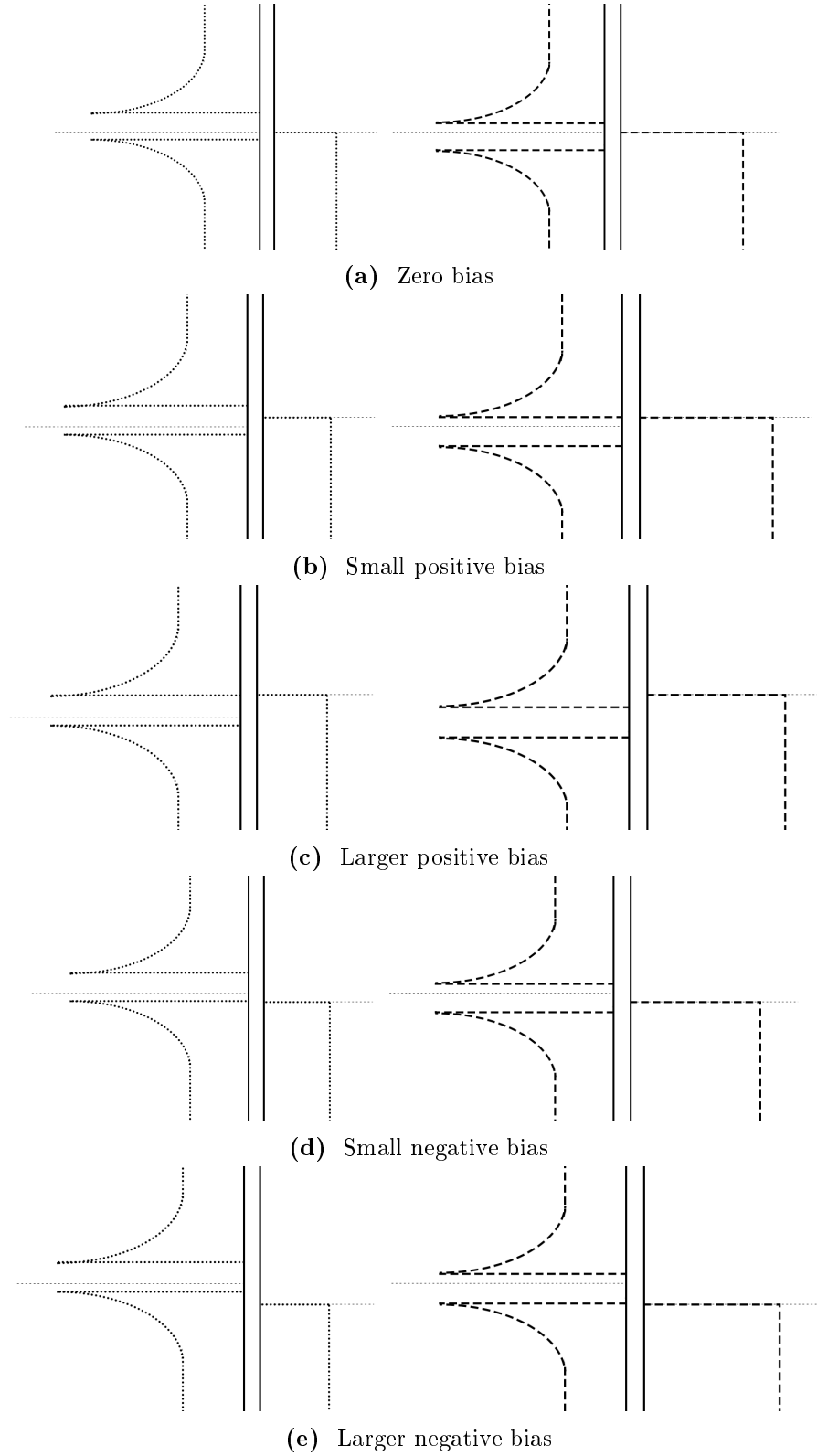


Figure A.1 – Schematic images of the DOS for a superconductor and a ferromagnetic material separated by a tunnel barrier. Dotted lines correspond to minority charge carriers and spin-down, while dashed lines correspond to majority charge carriers and spin-up. The DOS in the superconductor is spin-split by a magnetic field.

A.2 Lever arm effect

The lever arm effect is schematically depicted in Figure A.2.

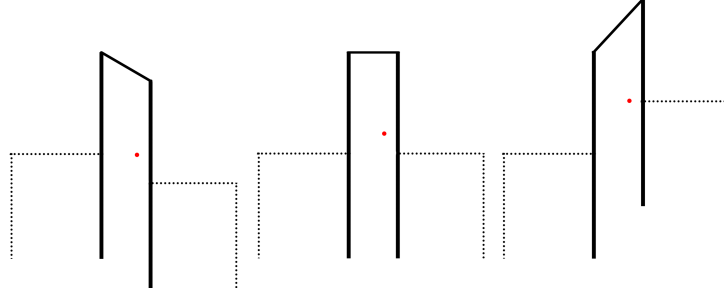


Figure A.2 – Lever arm effect for a geometrically asymmetric defect in a tunnel barrier. For zero bias (middle) the defect state obviously is not in the bias window. A bias is applied to the right electrode and its effect is assumed to only be a tilting of the barrier, which results in a triangular barrier. For positive bias (right image) a larger bias voltage than for negative bias (left image) is needed for the defect state to shift into the bias window.

Assume a defect with energy E_D above the Fermi level and take x as the ratio of the distance between the defect and the biased electrode, and the distance between the two electrodes. For the defect to be in the bias window at least the voltage corresponding to E_D should fall across the part of the barrier between the defect and the electrode with higher potential. For positive bias the defect shifts into the bias window for V_+ , while for negative bias this occurs for V_- . The Zeeman effect in combination with a spin polarised current effectively changes the weighted mean of the energy of the defect: $E_D \rightarrow E_D + \Delta E_D$, where ΔE_D is the weighted Zeeman shift and depends on the magnetic field and the spin polarisation of the current. The bias voltages at which the defect shifts into the bias window then become V'_+ and V'_- . The expressions for the absolute values of these bias voltages and the corresponding peak shifts are⁸:

$$V_+ = \frac{E_D}{x} \quad (\text{A.1a})$$

$$V_- = \frac{E_D}{1-x} \quad (\text{A.1b})$$

$$V'_+ = \frac{E_D + \Delta E_D}{x} \quad (\text{A.1c})$$

$$V'_- = \frac{E_D + \Delta E_D}{1-x} \quad (\text{A.1d})$$

$$\Delta V_+ = \frac{\Delta E_D}{x} \quad (\text{A.1e})$$

$$\Delta V_- = \frac{\Delta E_D}{1-x} \quad (\text{A.1f})$$

From these expression relevant ratios can be calculated:

$$\frac{V_+}{V_-} = \frac{1-x}{x} = \frac{\Delta V_+}{\Delta V_-} \quad (\text{A.2a})$$

$$\frac{\Delta V_+}{V_+} = \frac{\Delta E_D}{E_D} = \frac{\Delta V_-}{V_-} \quad (\text{A.2b})$$

⁸ Actually these expression should be divided by the elementary charge e , but for simplicity this is omitted here.

This shows the ratio of the peak shifts to be the same as the ratio of the peak positions and also the relative peak shifts are equal. This allows to calculate x . E_D can then be determined from the expressions in Equation A.1, which can be used to calculate ΔE_D if peak shifts can be determined accurately.

If ΔE_D is known or can be estimated this can be used to obtain an estimate for the spin polarisation of the tunnel current. Let E_Z be the absolute value for the Zeeman shift in the given circumstances. The weighted Zeeman shift can then be approximated as:

$$\Delta E_D = a \cdot E_Z + (1 - a) \cdot (-E_Z) = (2a - 1) \cdot E_Z = P \cdot E_Z \quad (\text{A.3})$$

where a is the fraction of either spin-up or spin-down electrons, because it is not possible to determine which of them is more abundant in the tunnel current from this analysis. Similar to the situation considered by Tedrow and Meservey the spin polarisation P is given by $P = 2a - 1$.

Although the value for ΔE_D is not easy to obtain accurately, because either the spin polarisation of the current or an accurate value for the peak shifts is required, it is equal for different defects in a single barrier, which can be used to obtain ratios between the peak shifts:

$$\frac{\Delta V_{+,1}}{\Delta V_{+,2}} = \frac{x_2}{x_1} \quad (\text{A.4a})$$

$$\frac{\Delta V_{-,1}}{\Delta V_{-,2}} = \frac{1 - x_2}{1 - x_1} \quad (\text{A.4b})$$

Appendix B

Design and fabrication

B.1 Recipe

Below the detailed recipe for the final fabrication process is given. It consists of four main steps (preparation, bottom electrode, contact holes and top electrodes), which contain several substeps.

0. Preparation (this step only has to be done once for a new wafer)
 - (a) Pick the 4 inch Si/SiO₂ wafer with a nickel layer covered with a few monolayers of graphene (1-7, 4 on average). These wafers can be bought at www.graphene-supermarket.com.
 - (b) Spin coat the wafer with a protective layer of photoresist and dice the wafer in smaller samples of 11 mm by 11 mm.
1. Define bottom electrodes
 - (a) Clean the samples in wetbench 11. Place them in a teflon sample holder and leave it in acetone until the protective layer is removed (usually a few minutes), rinse with isopropanol (IPA) and dry the samples with the nitrogen gun.
 - (b) Spin coat OiR 907/17 photoresist in wetbench 21. Use the 4000DYN recipe.
 - (c) Bake the samples on the 95°C hotplate for one minute.
 - (d) Pre-align the metal 4 inch sample holder with 20 sample positions (Figure B.1) in the EVG620 Bond Aligner.
 - (e) Place a sample at the correct position for the desired width of the bottom electrodes in the sample holder, align the sample and expose it for 4.5 seconds. Use the Topside recipe in hard contact mode and the 'Bottom contacts' mask as shown in Figure 4.2. Repeat this step for all samples.
 - (f) Bake the samples on the 120°C hotplate for one minute.
 - (g) Develop in OPD-4262 for 30 seconds, rinse thoroughly with water and dry with the nitrogen gun.
 - (h) Place the samples in the 4 inch sample holder for ion beam etching (Figure B.1). Use the one marked RIBE and be sure to not use the holders marked TCOater or BAK.

- (i) Load the sample holder into the Oxford Ionfab300Plus for etching with standard settings.⁹ Let the platen rotate at 5.0 rpm at an angle of 0°, add 5 sccm¹⁰ of argon gas to both neutralizer and beam and set the cool gas at 5.0 Torr. Etch away the complete nickel layer.¹¹
- (j) Unload the sample holder and remove the samples for the sample holder.

2. Define contact holes

- (a) Place the samples in the TePla 300E for a short treatment (~ 30 seconds) in oxygen plasma to strip the top of the resist layer. The oxygen flow should be 50% (200 sccm) and the power should be 500 W.
- (b) Clean the samples in wetbench 11. Place them in a teflon sample holder and leave it in acetone until the remaining photoresist is removed, rinse with IPA and dry the samples with the nitrogen gun. If necessary, repeat treatment in oxygen plasma and cleaning until all photoresist is removed. Do not expose the samples to oxygen plasma too long, because it can damage the graphene.
- (c) The next steps depend on whether the contact holes are defined by photolithography or EBL.
 - For contact holes defined by photolithography perform the following steps.
 - i. Spin coat diluted OiR 906/12 photoresist¹² in wetbench 21. Use a 0.45 μm filter on the bottle and use the 6000DYN recipe.
 - ii. Bake the samples on the 95°C hotplate for one minute.
 - iii. Pre-align the metal 4 inch sample holder with 20 sample positions in the EVG620 Bond Aligner.
 - iv. Place a sample at the correct position for the desired size of the contact holes in the sample holder, align the sample and expose it for 5 seconds. Use the Topside recipe in hard contact mode and the 'Contact holes' mask as shown in Figure 4.2. Repeat this step for all samples.
 - v. Bake the samples on the 120°C hotplate for one minute.
 - vi. Develop in OPD-4262 for 20 seconds, rinse thoroughly with water and dry with the nitrogen gun.
 - For contact holes defined by EBL perform the following steps.
 - i. Make images of the bottom electrodes with an optical microscope in which suitable graphene flakes (both large and thick enough) are visible.
 - ii. Define an EBL pattern with square contact holes of 150 nm by 150 nm by using these images in the EBL software.
 - iii. Spin coat PMMA A4 in wetbench 23 using the 2000 recipe.
 - iv. Write the EBL pattern in the RAITH150-TWO with an aperture of 10 μm, an acceleration voltage of 20 kV and a dose of 450 μC/cm².
 - v. Develop in 1:3 MIBK/IPA developer for 30 seconds, rinse in IPA and dry with the nitrogen gun.

⁹ Neutralizer current 100 mA, RF Generator power 300 W, Beam current 50 mA, Beam voltage and Accelerator voltage both 300V

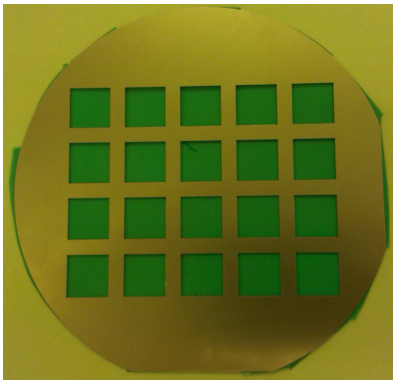
¹⁰ Standard Cubic Centimeters per Minute

¹¹ For wafer one and two this took approximately 40 and 55 minutes respectively.

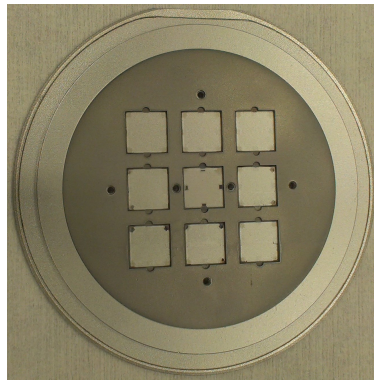
¹² 70 vol.% OiR 906/12, 18 vol.% methyl-3-methoxypropionate (MPP) and 12 vol.% ethyl-3-ethoxypropionate (EEP)

3. Deposit top electrodes

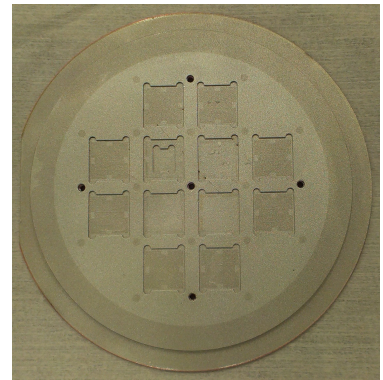
- (a) Start the cooling of the DCA by opening the liquid nitrogen valve and placing the turning knob in the 'Fill' position.
- (b) Stop the turbo pump to aerate the load lock of the DCA.
- (c) Place the samples in the 4 inch sample holder (Figure B.1) and place the shadow mask as shown in Figure 4.2 on top. Use the holder marked TCOater or BAK and be sure to not use the holder marker RIBE.
- (d) Place the sample holder on the wafer holder and together place them in the load lock.
- (e) Start the turbo pump to evacuate the load lock.
- (f) When the pressure in the load lock is sufficiently low, transfer the wafer holder to the deposition chamber and place it in the correct position for deposition (57 cm and 41°).
- (g) Place the crucible in the correct position for the material to be deposited.
- (h) Start the e-gun and gradually increase the emission current to the correct value.
- (i) Check the deposition rate with the rate monitor and, if it is sufficient and stable, open the shutter to start the deposition. At the same time, set the rate monitor to zero.
- (j) Close the shutter as soon as the desired thickness is obtained on the rate monitor. Keep in mind the tooling factor.
- (k) Gradually decrease the emission current and switch off the e-gun.
- (l) If aluminium oxide is deposited, perform the following steps:
 - i. Place the wafer holder in the load position (44 cm and 0°) and transfer it to the load lock.
 - ii. Aerate the load lock and close the nitrogen inlet at the turbo pump.
 - iii. Leave the wafer holder in the open load lock for at least one hour for natural oxidation of aluminium oxide.
 - iv. Evacuate the load lock and open the nitrogen inlet.
 - v. When the pressure in the load lock is sufficiently low, transfer the wafer holder to the deposition chamber and place it in the correct position for deposition
- (m) Repeat steps g-k for all layers.
- (n) After deposition of the final layer, place the wafer holder in the load position and transfer it to the load lock.
- (o) Aerate the load lock, unload the wafer holder and evacuate the load lock.
- (p) Remove the samples from the sample holder.
- (q) Stop the cooling by placing the turning knob in the 'Off' position and closing the liquid nitrogen valve.



(a) Photolithography with 20 sample position.



(b) Ion beam etching with 9 sample positions.



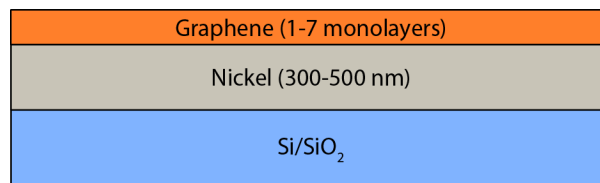
(c) Electron beam evaporation with 12 sample positions.

Figure B.1 – 4 inch sample holders. For etching and deposition it is important to use the correct sample holder to prevent contamination.

B.2 Workflow

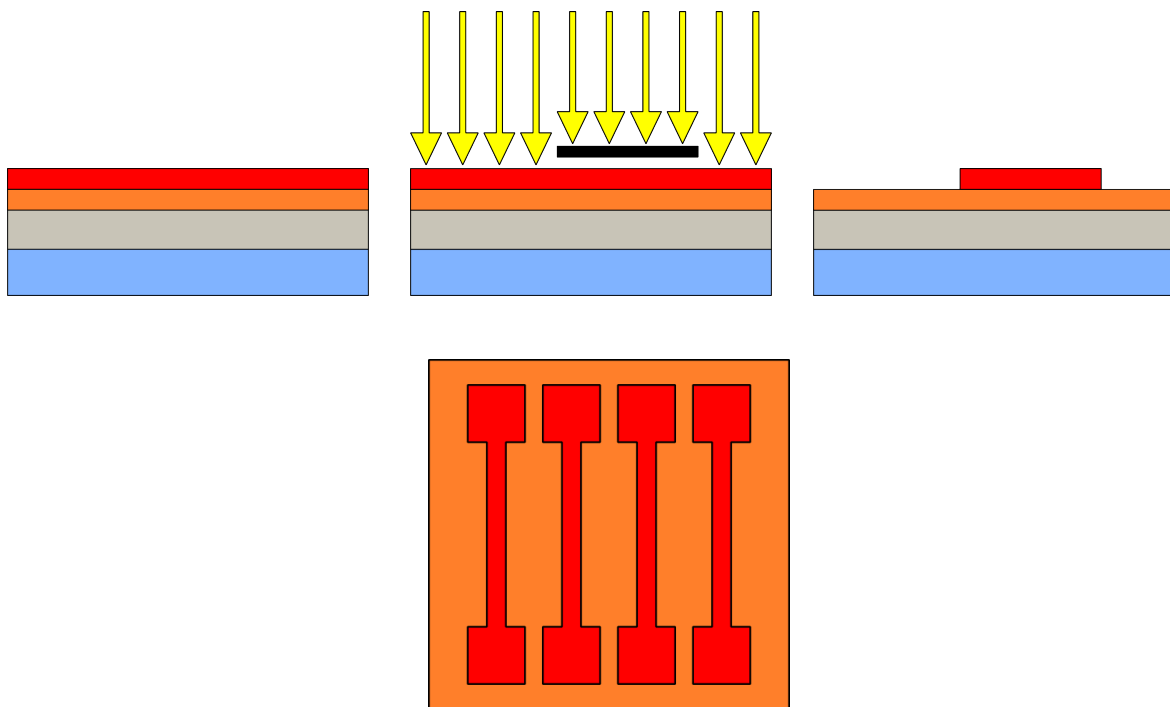
Below the workflow for the fabrication recipe described in the previous section is schematically depicted. The images are made by Elmer van Geijn. Order is from top to bottom and from left to right. Note: the numbers of bottom electrodes, contact holes and top electrodes are not equal to the actual number used.

0. Preparation

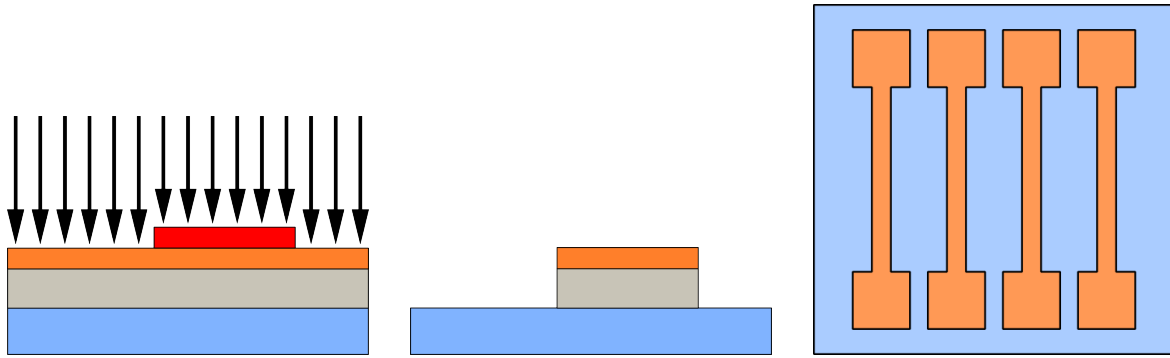


Sideview of untreated sample

1. Define bottom electrodes

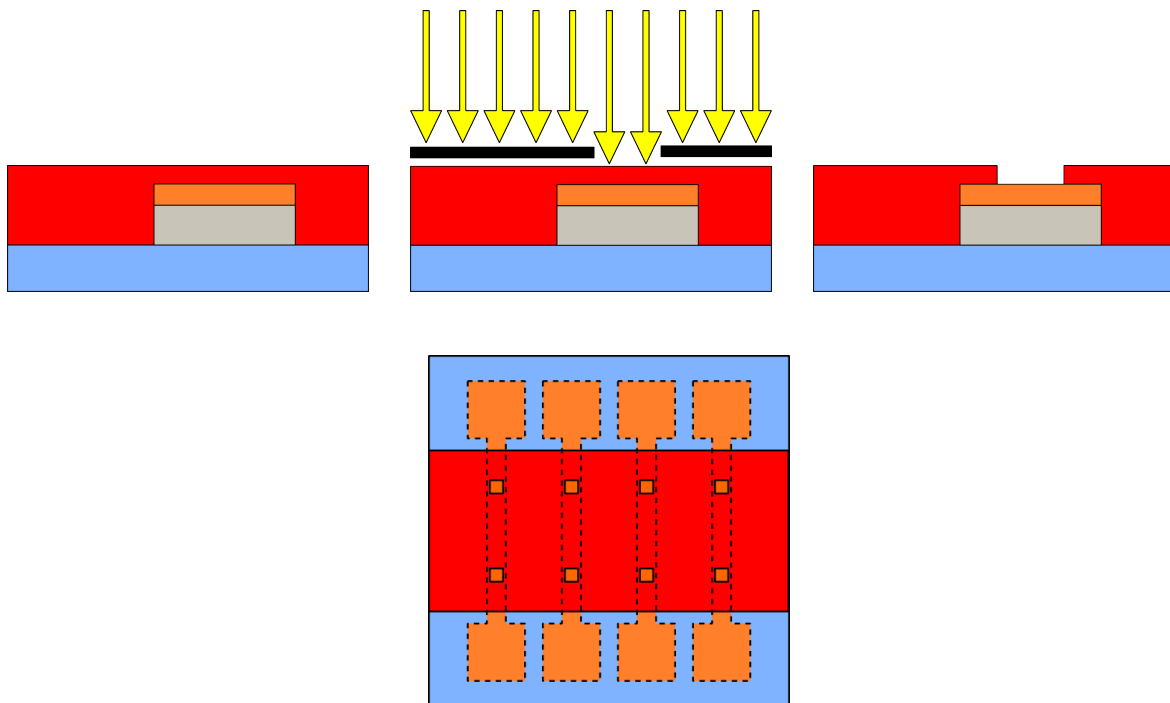


Top left: spin coat positive photoresist. Top middle: expose through 'Bottom contacts' mask. Top right: develop photoresist. Bottom: top view after developing photoresist.



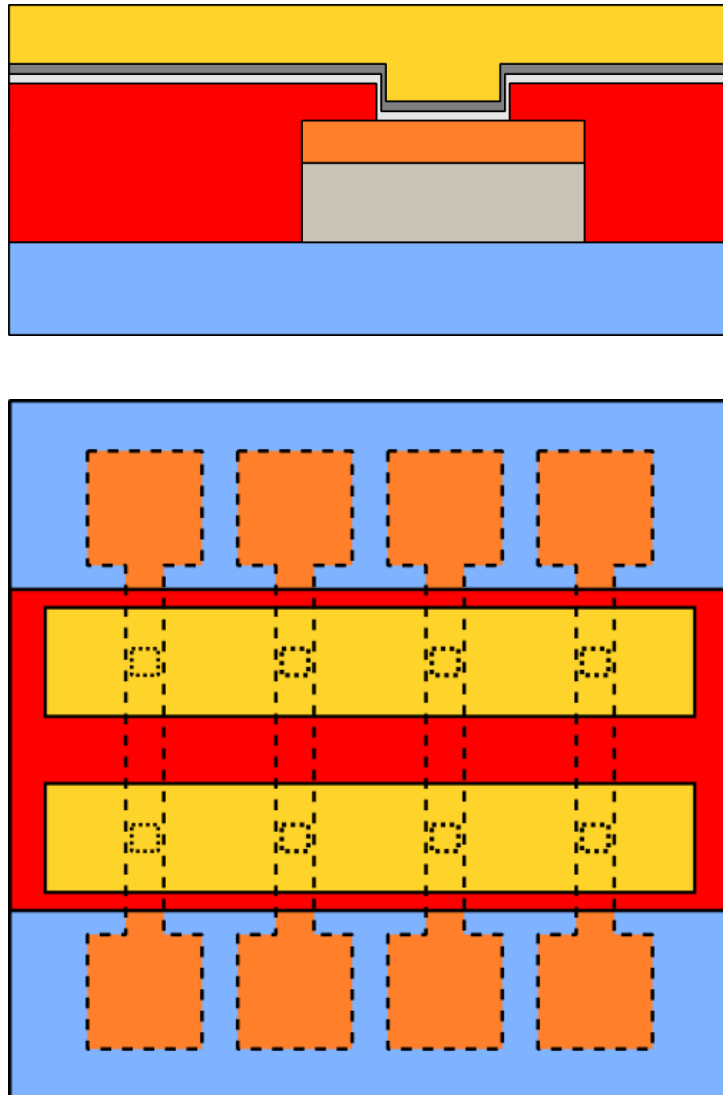
Left: etch away full graphene and nickel layer. Middle: remove resist. Right: top view after removing photoresist.

2. Define contact holes



Top left: spin coat positive photoresist or EBL resist. Top middle: expose through 'Contact holes' mask or write EBL pattern. Top right: develop photoresist or EBL resist. Bottom: top view after developing photoresist or EBL resist.

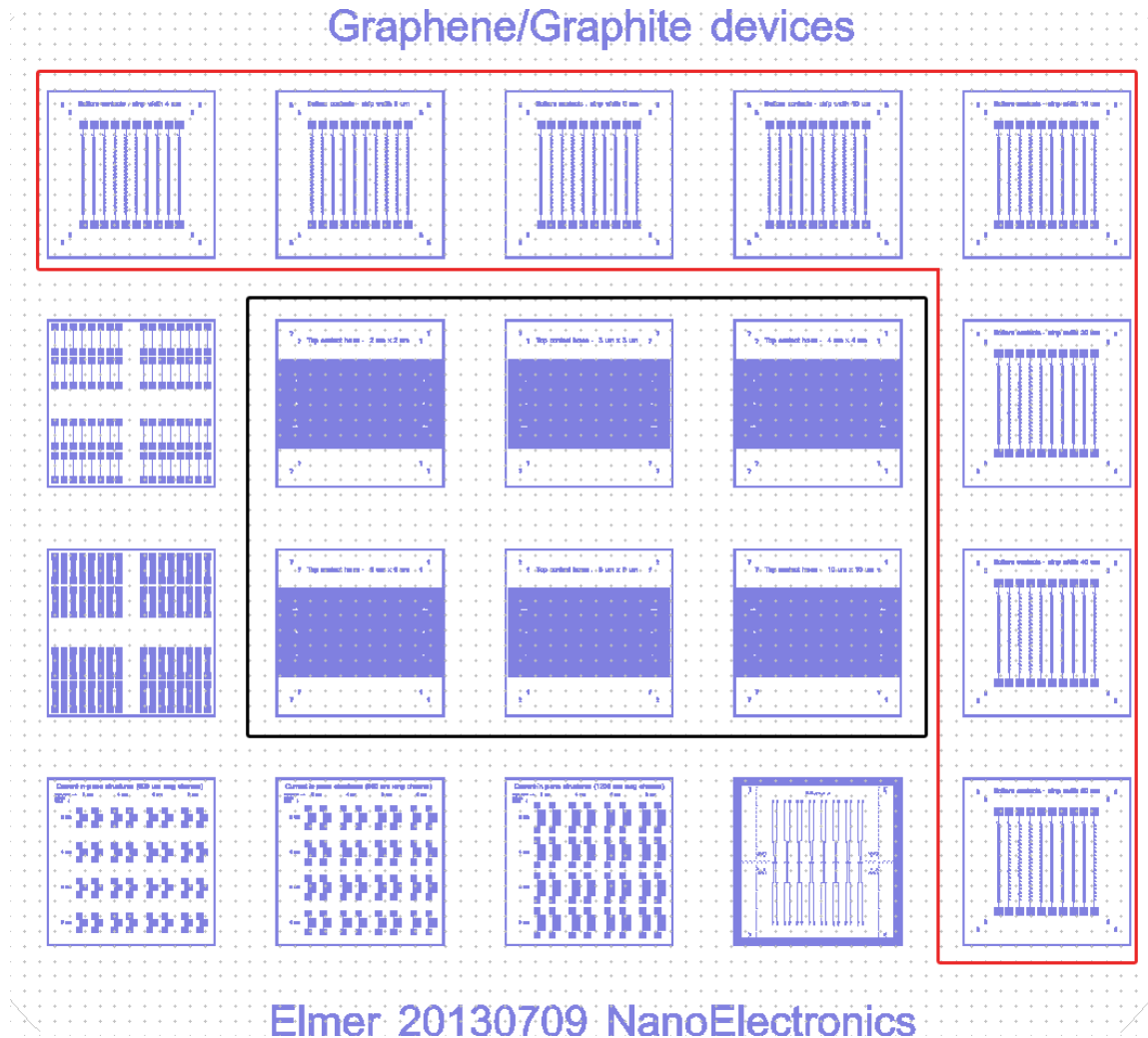
3. Deposit top electrode(s)



Top: deposit top electrode consisting of (in this case) three layers through shadow mask.
Bottom: top view after deposition of top electrode.

B.3 Mask

Below the design of the mask used for the two photolithography steps is shown. Each pattern is 11 mm by 11 mm. The patterns used for the bottom electrodes are in the red frame. Different widths for the electrodes are available, namely 4 μm , 6 μm , 8 μm , 10 μm , 15 μm , 20 μm , 40 μm and 60 μm . These patterns are used to define the bottom electrodes in the first exposure step. The patterns in the black frame are used for the contact holes. The size of the holes can be 2 μm , 3 μm , 4 μm , 6 μm , 8 μm and 10 μm . These patterns are used to define the contact holes if photolithography is used. The remaining patterns on this mask are not used in this project.



Appendix C

Results

C.1 Graphene thickness

The thickness of graphene flakes is estimated based on optical images, Raman spectroscopy and the corresponding cluster analyses. The estimated thickness for the different observed shades already is presented in Figure 5.14 and more details are given below.

What are major differences and what are just small variations in shades can be subject of discussion, but approximately five different shades can be distinguished in optical images of the used substrates. Three different Raman scans are used for the thickness estimation. For each scan the optical image, in which the used graphene flakes are indicated by circles, is shown on the left. The numbers indicate the corresponding clusters of which a zoom of the 2D peak of the corresponding Raman spectra are plotted in the graphs on the right.

The thickness estimates as presented earlier are related to the images presented here as summarised in the table below.

Thickness	Measurement	Cluster
1 layer	BM03	Cluster 7
2 layer	BM07	Cluster 2
3 layer	BM03	Cluster 18
4 layer	BM01	Cluster 13
5 layer	BM03	Cluster 12

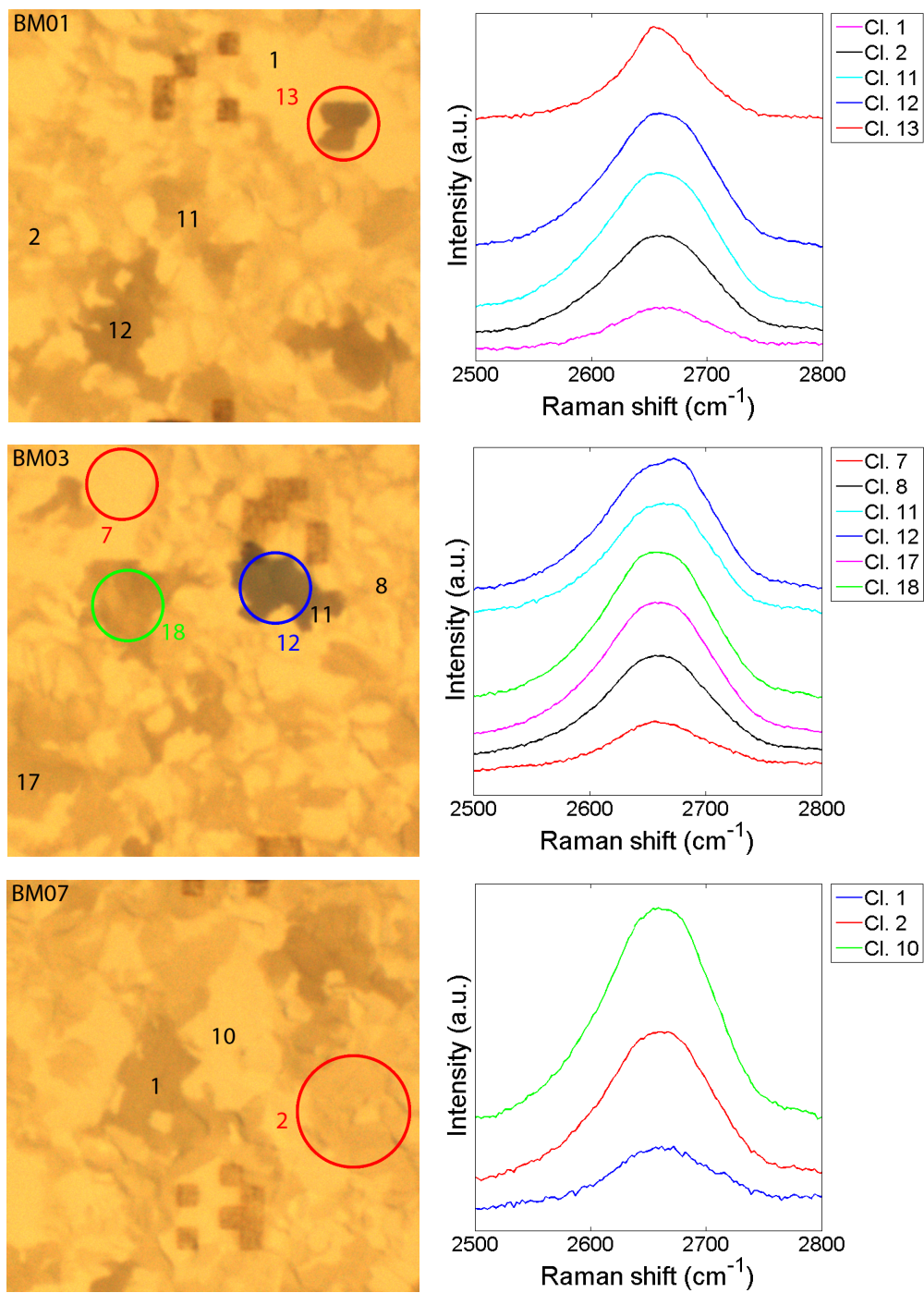


Figure C.1 – Optical images and Raman spectra used to estimate the graphene thickness. The circles in the optical images indicate the used flakes and the numbers in matching colour indicate the corresponding clusters of which the spectra are plotted in the images on the right. The black numbers indicate the other clusters, but these are not listed in the thickness estimation. From top to bottom the images correspond to measurements referred to as BM01, BM03 and BM07.